

AFIT/EN/ENG/97D-01

ANALYTIC TRANSFER FUNCTION OF THE  
FORWARD PROPAGATION OF DIFFUSE PHOTON  
DENSITY WAVES IN TURBID MEDIA WITH  
AN EMBEDDED SPHERICAL INHOMOGENEITY

THESIS

Deborah L. Lasocki  
Captain, USAF

AFIT/EN/ENG/97D-01

19980128 111

Approved for public release; distribution unlimited

**DTIC QUALITY INSPECTED 3**

The views expressed in this thesis are those of the author and do not reflect the official policy or position of the Department of Defense or the United States Government.

AFIT/EN/ENG/97D-01

ANALYTIC TRANSFER FUNCTION OF THE  
FORWARD PROPAGATION OF DIFFUSE PHOTON  
DENSITY WAVES IN TURBID MEDIA WITH  
AN EMBEDDED SPHERICAL INHOMOGENEITY

THESIS

Presented to the Faculty of the School of Engineering  
of the Air Force Institute of Technology  
Air University  
In Partial Fulfillment of the  
Requirements for the Degree of  
Master of Science in Electrical Engineering

Deborah L. Lasocki, B.S.E.E.  
Captain, USAF

December 1997

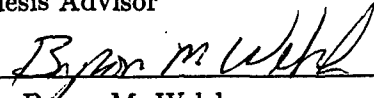
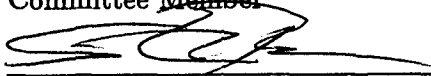
Approved for public release; distribution unlimited

ANALYTIC TRANSFER FUNCTION OF THE  
FORWARD PROPAGATION OF DIFFUSE PHOTON  
DENSITY WAVES IN TURBID MEDIA WITH  
AN EMBEDDED SPHERICAL INHOMOGENEITY

Deborah L. Lasocki, B.S.E.E.

Captain, USAF

Approved:

 _____ Capt. Peter J. Collins (Ph.D.) Thesis Advisor	<u>10/30/97</u> Date
 _____ Dr. Byron M. Welsh Committee Member	<u>10-30-97</u> Date
 _____ Dr. Michael C. Roggemann Committee Member	<u>10/30/97</u> Date
 _____ Dr. Steven K. Rogers Committee Member	<u>10/30/97</u> Date

### *Acknowledgements*

First and foremost, I would like to thank God for the wonderfully complex world He has given us to study. May we always see the beauty He has created around us.

I would like to thank everyone who supported my decision to take on such a difficult topic, in particular, my committee members Dr. Byron Welsh, Dr. Mike Roggemann, and Dr. Steve "Captain Amerika" Rogers. You all took the time to help when I needed it. Many words of thanks need to be bestowed upon Major Pete Collins, my thesis advisor, for always believing in me, even when the research looked quite bleak. It was your allowing me the freedom to work at my own pace and style that I appreciated most. Thank you.

I would also like to thank my sponsor, Dr. Chuck Matson of the Advanced Imaging Directorate at Phillips Labs. Your excitement and brilliant dabbling in this field made this thesis not only possible, but enjoyable. Thank you for your advice, guidance, and hard-to-answer questions that made me think. But most of all, thank you for inspiring the budding theoretician in me to continue challenging the world around me.

Also my parents must be recognized for instilling in me the need for higher education. Your support helped me to pursue and complete this thesis. I am only now beginning to realize how much your guidance throughout my life has contributed to my current success.

A special word of thanks to Christine Kerschus for your unfailing optimism, prayers, and much needed laughter and study breaks.

Finally, I want to thank my future husband, Troy Van Caster. You gave me endless encouragement and patience during these last 16 months, without which I could not have kept the peace of mind to complete this work. I only hope I was able to give you the same. I continue to thank God for bringing us together here at AFIT; you are my soul mate and my best friend. I am looking forward to many future years of exploring the world together.

"It is more important to have beauty in one's equations than to have them fit experiment...because the discrepancy may be due to minor features which are not properly taken into account and which will be cleared up with further developments of the theory....It seems that if one is working from the point of view of getting beauty into one's equations, and if one has a really sound instinct, one is on a sure line of success [25]"

Deborah L. Lasocki

## *Table of Contents*

	Page
Acknowledgements . . . . .	iii
List of Figures . . . . .	viii
List of Tables . . . . .	x
List of Symbols . . . . .	xi
Abstract . . . . .	xiii
I. Introduction . . . . .	1-1
II. Diffuse Photon Density Wave Propagation in Turbid Media . . . . .	2-1
2.1 Introduction . . . . .	2-1
2.2 Diffusion Approximation to the Transport Equation . . . . .	2-2
2.3 Diffuse Photon Density Waves . . . . .	2-3
2.4 Physics Model of Scattered DPDWs . . . . .	2-5
2.4.1 An Analytic Solution . . . . .	2-6
2.4.2 Semi-Infinite Media . . . . .	2-8
2.4.3 Resolution Limitations of the Analytic Solution . . . . .	2-9
2.5 Fourier Optics Model of Scattered DPDWs . . . . .	2-9
2.5.1 Wave Propagation in Source-Free Homogeneous Media . . . . .	2-10
2.5.2 Wave Propagation in Heterogeneous Media . . . . .	2-12
2.5.3 Reconstruction Algorithm . . . . .	2-13
2.5.4 Simulated Results . . . . .	2-14
2.5.5 Experimental Results . . . . .	2-15

	Page
III. An Analytic Transfer Function . . . . .	3-1
3.1 Introduction . . . . .	3-1
3.2 Transfer Function Formulation . . . . .	3-1
3.3 Decomposition of a Spherical Wave Into Plane Waves . . . . .	3-4
3.3.1 Incident Field Representation . . . . .	3-4
3.3.2 Scattered Field Reformulation . . . . .	3-6
3.4 Fourier Transform of the Analytic Solution . . . . .	3-9
3.4.1 Incident Wave . . . . .	3-9
3.4.2 Scattered Wave . . . . .	3-10
3.4.3 Transfer Function . . . . .	3-10
3.5 Summary . . . . .	3-11
IV. Implementation of Transfer Function Models and Test Plan . . . . .	4-1
4.1 Introduction . . . . .	4-1
4.2 System Geometry . . . . .	4-1
4.3 Approximations in Simulations . . . . .	4-2
4.3.1 Series Truncation . . . . .	4-2
4.3.2 Sampling Around Singularities . . . . .	4-3
4.4 Correlation Methodology . . . . .	4-4
4.5 Implementation of Analytic Solution Method . . . . .	4-4
4.6 Analytic Solution Simulation Code Development . . . . .	4-5
4.6.1 Code Structure . . . . .	4-5
4.6.2 Input Parameters . . . . .	4-5
4.6.3 Output Quantities . . . . .	4-6
4.6.4 Validation of Simulation . . . . .	4-6
4.7 Implementation of Analytic Transfer Function Method . . . . .	4-8
4.8 Analytic Transfer Function Simulation Code Development . . . . .	4-8
4.8.1 Code Structure . . . . .	4-9

	Page
4.8.2	Discretization Effects . . . . . 4-9
4.8.3	Input Parameters . . . . . 4-9
4.8.4	Output Quantities . . . . . 4-9
4.8.5	Validation of Simulation . . . . . 4-10
4.9	Implementation of the Fourier Optics Model . . . . . 4-11
4.9.1	Code Structure . . . . . 4-12
4.9.2	Discretization Effects . . . . . 4-13
4.9.3	Input Parameters . . . . . 4-13
4.9.4	Output Quantities . . . . . 4-14
4.10	Test Plan . . . . . 4-14
4.10.1	Perturbation Cases . . . . . 4-14
4.10.2	Analysis Plan . . . . . 4-15
4.11	Summary . . . . . 4-16
V.	Simulation Results and Analysis . . . . . 5-1
5.1	Introduction . . . . . 5-1
5.2	Sensitivity to Contrasts in Optical Parameters . . . . . 5-1
5.2.1	System Configuration . . . . . 5-2
5.2.2	Absorption Contrast With a Pure Absorber . . . . . 5-3
5.2.3	Scattering Contrast With a Pure Scatterer . . . . . 5-5
5.2.4	Low Contrast in Absorption and Varied Contrast in Scattering Coefficients . . . . . 5-5
5.2.5	High Contrast in Absorption and Varied Contrast in Scattering Coefficients . . . . . 5-9
5.2.6	Low Contrast in Scattering and Varied Contrast in Absorption Coefficients . . . . . 5-11
5.2.7	High Contrast in Scattering and Varied Contrast in Absorption Coefficients . . . . . 5-14
5.2.8	Summary of Sensitivity Analysis . . . . . 5-14

	Page
5.3 Sensitivity to Inhomogeneity Size . . . . .	5-19
5.4 Scattering Moment Contributions . . . . .	5-19
5.4.1 Pure Absorption . . . . .	5-21
5.4.2 Pure Scatterer . . . . .	5-22
5.4.3 High Absorption Contrast . . . . .	5-22
5.4.4 Low Absorptive Contrast . . . . .	5-24
5.4.5 High Scattering Contrast . . . . .	5-24
5.4.6 Low Scattering Contrast . . . . .	5-25
5.4.7 Summary of Moment Analysis . . . . .	5-26
5.5 Fourier Optics Model Validity . . . . .	5-35
5.6 Summary . . . . .	5-46
VI. Summary . . . . .	6-1
6.1 Conclusions . . . . .	6-1
6.2 Recommendations for Future Research . . . . .	6-2
6.3 Closing . . . . .	6-3
Appendix A. Input Parameter Code Listing to the Analytic Solution . . .	A-1
Appendix B. Analytic Solution Code Listing . . . . .	B-1
Appendix C. Transfer Function Code Listing to the Analytic Solution . .	C-1
Appendix D. Fourier Optics Wave Propagation Code Listing . . . . .	D-1
Bibliography . . . . .	BIB-1
Vita . . . . .	VITA-1

*List of Figures*

Figure		Page
2.1.	Coordinates for Inhomogeneity Geometry . . . . .	2-4
2.2.	Diffuse Photon Density Wave Propagation Representation . . . . .	2-5
2.3.	Extrapolated Surface for Semi-Infinite Medium . . . . .	2-9
2.4.	Fourier Optics Reconstruction Schematic . . . . .	2-13
3.1.	Linear System Representation . . . . .	3-1
3.2.	Analytic and Fourier Optics Solution Systems . . . . .	3-3
3.3.	Path of Integration in Transform Space . . . . .	3-7
3.4.	Region of Validity of the Multipole Expansion . . . . .	3-9
4.1.	System Geometry for Simulations . . . . .	4-2
4.2.	Series Truncation Effects on Precision . . . . .	4-3
4.3.	Percent Error of Analytic Incident Wave . . . . .	4-8
4.4.	Percent Error of Analytic Scattered Wave . . . . .	4-9
4.5.	Percent Error of Analytic Total Wave . . . . .	4-10
4.6.	Flow Chart for Analytic Transfer Function Method . . . . .	4-11
4.7.	Percent Error of Analytic Transfer Total Wave . . . . .	4-12
4.8.	Flow Chart for the Fourier Optics Model . . . . .	4-13
5.1.	Location of Maximum Perturbation in Lateral Direction . . . . .	5-2
5.2.	Homogeneous, Scattered, and Total Wave Slices of a Pure Absorber	5-4
5.3.	Analytic Transfer Function for Pure Absorbers . . . . .	5-6
5.4.	Homogeneous, Scattered, and Total Wave Slices of a Pure Scatterer	5-7
5.5.	Analytic Transfer Function for Pure Scatterers . . . . .	5-8
5.6.	Analytic Transfer Function for Low Contrast in $\mu_a$ . . . . .	5-10
5.7.	Analytic Transfer Function for High Contrast in $\mu_a$ . . . . .	5-12

Figure		Page
5.8.	Analytic Transfer Function for Very High Contrast in $\mu_a$ . . . . .	5-13
5.9.	Analytic Transfer Function for Low Contrast in $\mu'_s$ . . . . .	5-15
5.10.	Analytic Transfer Function for High Contrast in $\mu'_s$ . . . . .	5-16
5.11.	Analytic Transfer Function for Very High Contrast in $\mu'_s$ . . . . .	5-17
5.12.	Sensitivity to Change in Inhomogeneity Size . . . . .	5-20
5.13.	Moments of a Pure Absorber, High Contrast . . . . .	5-27
5.14.	Moments of a Pure Absorber, Low Contrast . . . . .	5-28
5.15.	Moments of a Pure Scatterer, High Contrast . . . . .	5-29
5.16.	Moments of a Pure Scatterer, Low Contrast . . . . .	5-30
5.17.	Moments for High Contrast in $\mu_a$ and $\mu'_s$ . . . . .	5-31
5.18.	Moments for High Contrast in $\mu_a$ and Low Contrast in $\mu'_s$ . . . . .	5-32
5.19.	Moments for Low Contrast in $\mu_a$ and $\mu'_s$ . . . . .	5-33
5.20.	Moments for Low Contrast in $\mu_a$ and High Contrast in $\mu'_s$ . . . . .	5-34
5.21.	Mean Square Error for Pure Absorbers . . . . .	5-38
5.22.	Mean Square Error for Pure Scatterers . . . . .	5-39
5.23.	Mean Square Error for Low Contrast in $\mu_a$ . . . . .	5-40
5.24.	Mean Square Error for High Contrast in $\mu_a$ . . . . .	5-41
5.25.	Mean Square Error for Very High Contrast in $\mu_a$ . . . . .	5-42
5.26.	Mean Square Error for Low Contrast in $\mu'_s$ . . . . .	5-43
5.27.	Mean Square Error for High Contrast in $\mu'_s$ . . . . .	5-44
5.28.	Mean Square Error for Very High Contrast in $\mu'_s$ . . . . .	5-45

*List of Tables*

Table		Page
4.1.	Mean-Square Error Verification of Simulation Codes . . . . .	4-12
4.2.	Typical Optical Parameters of Tissue . . . . .	4-14
4.3.	Optical Parameter Test Matrix . . . . .	4-15

*List of Symbols*

Symbol	Page
$L$ spectral radiance . . . . .	2-2
$\hat{\Omega}$ direction . . . . .	2-2
$t$ time . . . . .	2-2
$v$ speed of light in medium . . . . .	2-2
$\mu_t$ transport coefficient . . . . .	2-2
$\mu_a$ absorption coefficient . . . . .	2-2
$\mu_s$ scattering coefficient . . . . .	2-2
$\mu'_s$ reduced scattering coefficient . . . . .	2-2
$g_1$ scattering angle . . . . .	2-2
$f(\hat{\Omega}, \hat{\Omega}')$ normalized phase function . . . . .	2-2
$S(\bar{r}, \hat{\Omega}, t)$ angular distribution of the source . . . . .	2-2
$D$ diffusion coefficient . . . . .	2-3
$S_0(\bar{r}, t)$ isotropic moment of the source . . . . .	2-3
$\omega$ angular frequency . . . . .	2-4
$k$ complex wavenumber . . . . .	2-4
$S_{AC}$ source modulation amplitude . . . . .	2-4
$\Phi_{AC}$ homogeneous wave solution . . . . .	2-4
$\Phi$ total wave solution . . . . .	2-6
$\Phi_{SC}$ scattered wave solution . . . . .	2-6
$j_l$ spherical Bessel function of the first kind, order $l$ . . . . .	2-6
$n_l$ spherical Neumann function of the first kind, order $l$ . . . . .	2-6
$Y_l^m$ spherical harmonics of degree $l$ , order $m$ . . . . .	2-6
$A_{l,m}$ scattered wave amplitude . . . . .	2-7
$z_s$ source distance . . . . .	2-7
$a$ inhomogeneity radius . . . . .	2-7

Symbol	Page
$D_{out}$ photon diffusion coefficient of background medium . . . . .	2-7
$D_{in}$ diffusion coefficient inside the inhomogeneity . . . . .	2-7
$k_{out}$ wavenumber of background medium . . . . .	2-7
$k_{in}$ wavenumber inside the inhomogeneity . . . . .	2-7
$h_l^{(1)}$ spherical Hankel function of the first kind, type $l$ . . . . .	2-7
$h_l^{(1)'}$ first derivative of the spherical Hankel function of the first kind, type $l$	2-7
$j_l'$ first derivative of the spherical Bessel function of the first kind . . . . .	2-7
$z_d$ measurement (detector) plane distance . . . . .	2-9
$\mathcal{F}$ Fourier transform operator . . . . .	2-11
$\mathcal{F}^{-1}$ Inverse Fourier transform operator . . . . .	2-11
$f_x$ spatial frequency variable . . . . .	2-11
$f_y$ spatial frequency variable . . . . .	2-11
$t_A$ transmittance function . . . . .	2-12
$\Delta z$ $z$ -plane interval . . . . .	2-13
$\xi$ complex frequency variable . . . . .	3-4
$\eta$ complex frequency variable . . . . .	3-4
$\zeta$ complex frequency variable . . . . .	3-4
$P_l$ Legendre polynomial . . . . .	3-6
$\alpha$ complex spherical angle . . . . .	3-6
$\beta$ real spherical angle . . . . .	3-6
$U_{AC}$ homogeneous wave solution in Fourier space . . . . .	3-10
$U_{SC}$ scattered wave solution in Fourier space . . . . .	3-10
$\sigma^2$ mean-square error . . . . .	4-4

*Abstract*

Diffusing photons can be used to detect and localize optical inhomogeneities embedded in turbid media such as clouds, fog, paint and human tissue. This thesis shows that a transfer function derived from an analytic solution of the Helmholtz equation can completely characterize in three dimensions the perturbations in the forward propagation phenomena caused by a spherical defect object in a multiple-scattering medium.

Two models of the forward propagation behavior of diffuse photon density waves (DPDW) in homogeneous, infinite, turbid media that contains a spherical inhomogeneity are examined. DPDWs are generated from sinusoidally, intensity-modulated sources of light and are highly damped waves with a complex wavenumber. These waves can be described by expressions derived from the diffusion approximation to the linear transport equation. The first model is an exact analytic solution based on a modal expansion in spherical harmonics. The second model uses Fourier optics theory for wave propagation in a plane through homogeneous turbid media containing a spherical lens. The Fourier optics model is found to be a good approximation to the exact analytic solution when the optical absorptive contrast of the inhomogeneity and the surrounding media is weakly perturbative, and the detector is not near the inhomogeneity.

Using linear systems theory, a transfer function from the analytic model is derived. This function improves the Fourier optics model by replacing the spherical lens approximation with an exact representation of the system perturbation behavior. The transfer function is shown through simulation to completely characterize the sensitivity of the system to detect and localize in three dimensions inhomogeneities of varying optical contrasts with the surrounding media.

ANALYTIC TRANSFER FUNCTION OF THE  
FORWARD PROPAGATION OF DIFFUSE PHOTON  
DENSITY WAVES IN TURBID MEDIA WITH  
AN EMBEDDED SPHERICAL INHOMOGENEITY

*I. Introduction*

Concern over the limitation, cost-effectiveness, and risks associated with ionizing radiation in the imaging and diagnosis of human breast cancer is motivating researchers to seek other, safer methods of detecting breast lesions [6]. Light radiation as an imaging tool was apparent as early as 1929 in the pioneering mammography studies of Cutler [20, 21]. Light provides a non-invasive probe to image benign and malignant structures within human tissue. In spite of initial support for the new transillumination technique, the procedure fell into disrepute, probably due to inadequacy of the available equipment [36]. Later improvements to Cutler's work reported that transmission of light through human skin is decreased in the shorter wavelength spectrum and is increased in the near infrared [2, 15, 43]. This particular approach of illuminating, or diffusing, near infrared photons (NIR) in turbid media, such as human tissue, is continuing to emerge as a potentially important imaging modality [47, 54, 58].

There are many methods in which light is applied to image breast lesions. One of these methods is based on the concept of light traveling unscattered, or ballistically, through turbid media. The unscattered light is then distinguished from the scattered light using time or spatial gating techniques [8, 28, 37, 47, 50, 55]. For many biological tissues, the absorption length for NIR light is much longer than the scattering length and is much smaller than the dimensions of the sample. So in thick tissue, this ballistic method is unsuitable since unscattered light is highly attenuated and becomes indistinguishable from the scattered light. When the turbid medium is thick, other methods for non-invasive imaging can be applied. The traveling photons through the turbid medium are scattered

multiple times before they are absorbed or transmitted through the medium. This process of traveling through turbid media can be accurately described by a diffusional process [12, 40, 45].

The general behavior of photons propagating in an absorptive and scattering medium is described by the linear transport equation [9, 16, 22, 31]. Analytic solutions to this equation are typically difficult to handle and computationally intensive. Under certain conditions, the transport equation can best be approximated by the photon diffusion equation. When the intensity of the source of light is sinusoidally modulated, the photon diffusion equation can be rewritten as the Helmholtz equation. The modulated light source, referred to as a diffuse photon density wave (DPDW), produces a light energy density which propagates outwards from the source through the turbid medium [12, 28, 44]. On the microscopic level, photons walk in random paths, but macroscopically, the photons combine to produce a scalar wave of light energy density that maintains a well-defined wavelength, amplitude, and phase [58] and can thus be treated within the framework of wave phenomena. The wave behavior of DPDWs have been well researched, particularly the perturbations caused by optical inhomogeneities [11, 17, 28, 44, 51, 54].

Carcinomas compared to healthy tissue absorb light differently in narrow spectra, particularly in the NIR spectrum [36]. Lesions are then typically modeled as spherical inhomogeneities which have different optical (absorptive and scattering) properties than the breast tissue medium surrounding it. When a DPDW is incident on the tissue, the contrast in the optical properties of the inhomogeneity and the background tissue causes distortions in the DPDW. Measurements of these distortions can be used to characterize and localize these inhomogeneities [12]. The slab geometry is extensively used as a model of a physically compressed breast as it occurs during mammography. However, the geometry can be modified as an infinite medium if the tumor is small, since the boundaries of the medium do not significantly affect the DPDW.

Analytic solutions have been determined to exactly model this forward propagation of the DPDW in a turbid medium that contains an embedded spherical inhomogeneity [11, 17, 28, 44, 51, 54]. Another solution approach of this phenomena uses Fourier optics theory [40]. When the optical properties are weakly perturbative, meaning that the difference between

the optical properties inside and outside the inhomogeneity is small, the spherical tumor can be approximated as a thin lens. The Fourier optics approach models the source wave as a superposition of plane waves traveling through a piece-wise homogeneous medium. However, as the contrast in optical properties increases, the model of the inhomogeneity becomes invalid.

In this research, an exact transfer function is desired to model an infinite, homogeneous, turbid medium with an embedded spherical inhomogeneity. This transfer function completely characterizes the system and can be used to exactly model the forward propagation of the DPDW using Fourier optics theory. This model can be used to improve the Fourier optics approach by modeling perturbations caused by the inhomogeneity exactly rather than by approximating the object as a thin lens. In addition, the transfer function can be analyzed directly to determine the sensitivity of the system to detect and localize different inhomogeneities, particularly those which weakly perturb the system.

This thesis is structured into six chapters covering the history of optical imaging, the development and the simulation of the transfer function, and a comparative analysis of several forward propagation models used in research today. Specifically, Chapter II reviews the photon transport equation, the diffusion model, and the optics associated with the scalar wave (DPDW) solution that arise from the model. In addition, aspects of Fourier optics theory are presented which relate to its application to the forward propagation of a spherical wave through a heterogeneous medium. Chapter III develops an exact transfer function to completely characterize a spherical wave traveling through an infinite homogeneous medium containing an embedded spherical inhomogeneity. Chapter IV discusses the structure of the simulations, demonstrates the validity and accuracy of the transfer function method as well as the Fourier optics model, and outlines the specific inhomogeneity optical characteristics that are of interest in this thesis. Simulation codes for the transfer function and the Fourier optics methods are presented in Appendices C and D, respectively. Chapter V presents and discusses the results of the simulations conducted. Chapter VI reviews conclusions made throughout the thesis and recommends areas for further study.

## *II. Diffuse Photon Density Wave Propagation in Turbid Media*

### *2.1 Introduction*

Visually opaque media are unusual in that some are considered opaque because they strongly absorb visible light. Others such as paint, foam, milk, and human tissue are optically opaque because the light traveling within them is highly scattered. In fact, a very small number of photons travel in straight lines through such materials. Instead, the photons incident within a thick material multiply scatter and trace out random paths until they are either absorbed, or they escape through the boundaries of the media. Media that cause photons to propagate, or "diffuse", through the material in that manner are also referred to as optically "turbid" media. Human tissue acts as a turbid medium in a narrow spectral window of about 700-900 nm where the light is mostly scattered, and the absorption effects are small.

The high degree of scattering, a result of a very short scattering length characteristic of photon transport in turbid media, has been shown to be very well approximated as a diffusive process. This diffusion transport behavior of photons is commonly known as photon migration. When the intensity of the incident light wave is sinusoidally modulated, it has a small but measurable traveling wave disturbance of the light energy density propagating outwards from the source. This is hence referred to as a diffuse photon density wave (DPDW) [12, 28, 44].

In this chapter, photon migration properties are investigated through the radiative transport equation and its approximation leading to the photon diffusion equation. DPDWs are known to adhere to standard scattering models. A particular analytic model for localizing a spherical heterogeneity in an otherwise homogeneous medium as well as its resolution limitations are presented. Finally, a Fourier optics model to the same perturbation problem and its resolution performance are discussed. These solution developments form a basis for the comparison of two approaches to deep tissue imaging with near infrared light.

## 2.2 Diffusion Approximation to the Transport Equation

The propagation of waves in scattering media can be rigorously described with the linear transport equation [9, 16, 22, 31]

$$\frac{1}{v} \frac{\partial L(\bar{r}, \hat{\Omega}, t)}{\partial t} + \nabla \cdot L(\bar{r}, \hat{\Omega}, t) \hat{\Omega} + \mu_t L(\bar{r}, \hat{\Omega}, t) = \mu_s \int L(\bar{r}, \hat{\Omega}', t) f(\hat{\Omega}, \hat{\Omega}') d\hat{\Omega}' + S(\bar{r}, \hat{\Omega}, t). \quad (2.1)$$

The gradient symbol  $\nabla = \frac{\partial}{\partial x} \hat{i} + \frac{\partial}{\partial y} \hat{j} + \frac{\partial}{\partial z} \hat{k}$ , where  $\hat{i}$ ,  $\hat{j}$  and  $\hat{k}$  are unit vectors in the  $x$ ,  $y$ , and  $z$  directions, respectively.  $L(\bar{r}, \hat{\Omega}, t)$  is the spectral radiance, or the number of photons per unit volume, per unit wavelength, per unit solid angle (sr = steradian = unit solid angle) at  $\bar{r}$ , traveling in direction  $\hat{\Omega}$ , at time  $t$ , with units of  $\text{Wm}^{-2}\text{sr}^{-1}$ .  $v$  is the speed of light in the transporting (turbid) medium which is characterized by the transport coefficient  $\mu_t$  where  $\mu_t = \mu_s + \mu_a$ . The absorption coefficient is  $\mu_a$  in units of  $\text{m}^{-1}$ , and the scattering coefficient,  $\mu_s$ , in the same units, is the reciprocal of the scattering length. The reduced scattering coefficient  $\mu'_s$  is the reciprocal of the random walk step, meaning it is the reciprocal of the average path length before the photon's direction becomes random. The two scattering parameters are related by the measure of the amount of incident light scattered in the forward direction, i.e. the average cosine of the scattering angle,  $g_1$  [28, 35].

$$\mu'_s = \mu_s(1 - g_1) = \mu_s(1 - \langle \cos \theta \rangle) \quad (2.2)$$

The normalized phase function  $f(\hat{\Omega}, \hat{\Omega}')$  represents the probability of scattering from direction  $\hat{\Omega}$  into direction  $\hat{\Omega}'$ . The last term,  $S(\bar{r}, \hat{\Omega}, t)$  is the spatial and angular distribution of the source with units of  $\text{Wm}^{-3}\text{sr}^{-1}$ .

The transport equation is usually interpreted as a conservation equation for the radiance,  $L(\bar{r}, \hat{\Omega}, t)$ . Many of the difficulties of the solutions to the transport equation include numerical analysis and heavy computational efforts. The  $P_N$  approximation method reduces those difficulties and still results in a valid solution when applied to the transport equation [10, 16, 22, 31]. The  $P_N$  approximation expands the radiance  $L$ , the phase function  $f$ , and the source  $S$  into a truncated sum of spherical harmonics  $Y_{l,m}$  [10]. The  $P_1$  approx-

imation is valid if it is assumed that the source-detector separation is large as compared to  $(1/\mu_s)$ , and that the scattering frequency is much larger than the source modulation frequency [28]. The condition  $\mu_s/(\mu_s + \mu_a) \approx 1$  must also be met for the  $P_1$  approximation to be valid [30]. When the scattering dominates the absorption in the medium, e.g.  $\mu'_s \gg \mu_a$ , then the radiance can be expressed as an isotropic source [10, 29]. In cases where photon absorption is large as in the liver, hematomas, and regions with large blood concentrations, higher order solutions to the transport equation would be a more accurate approximation. The optical properties of the human brain or breast demonstrate that the  $P_1$  approximation is valid [27]. The photons are treated as particles in this work, thus the interference terms from superposition effects as well as polarization are neglected in this simplification of the transport equation [26]. If the source is sinusoidally modulated, then applying these assumptions reduces the transport equation (2.1) to the photon diffusion equation [10, 16]

$$-D\nabla^2\Phi(\bar{r}, t) + v\mu_a\Phi(\bar{r}, t) + \frac{\partial\Phi(\bar{r}, t)}{\partial t} = vS_0(\bar{r}, t). \quad (2.3)$$

Here, the photon fluence (or energy density) is represented as

$$\Phi(\bar{r}, t) = \int d\hat{\Omega}L(\bar{r}, \hat{\Omega}, t), \quad (2.4)$$

and has units of  $\text{Wm}^{-2}$ . The diffusion coefficient is given by  $D = v/[3(\mu_a + \mu'_s)]$  is in units of  $\text{m}^{-1}$ , and  $S_0(\bar{r}, t)$  is the monopole (isotropic) moment of the source.

It has been demonstrated that at a sharp boundary for a small random walk step  $(1/\mu'_s)$ , the transport equation better approximates the photon migration across the boundary [12]. Otherwise, the light transport in the medium is well approximated by the diffusion equation.

### 2.3 Diffuse Photon Density Waves

Many analytic solutions to the diffusion equation have been derived to model plane wave sources in semi-infinite media [33], as well as on slab [16], spherical [12, 45, 52] and other media surfaces [4]. However, if the intensity of the photon source is sinusoidally

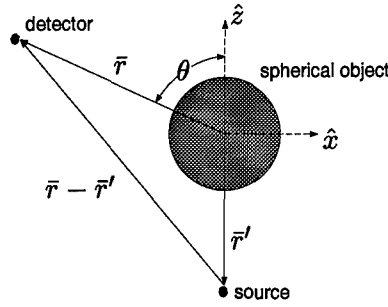


Figure 2.1 To solve the frequency dependent Helmholtz equation for a spherical inhomogeneity, it is natural to use spherical coordinates with the origin at the center of the object. The source is situated along the  $\hat{z}$  axis ( $\theta_s = \pi$ ), allowing azimuthal symmetry to be exploited. The radial distances for the source, detector and inhomogeneity are indicated in the diagram [10].

modulated at angular frequency  $\omega$ , e.g.  $S(\bar{r}) = S_{DC}(\bar{r}) + S_{AC}(\bar{r})\exp(-j\omega t)$ , then the light energy density within the turbid medium can be written as a combination of the time-dependent and time-independent parts, i.e.,  $\Phi(\bar{r}) = \Phi_{DC}(\bar{r}) + \Phi_{AC}(\bar{r})\exp(-j\omega t)$  [58].

With an oscillating point source, Equation (2.3) can be rewritten as the Helmholtz equation [28] at the field point  $\bar{r}$  with spherical polar coordinates  $(r, \theta, \phi)$  in the frequency domain (denoted with subscripts  $AC$ ) as

$$\nabla^2 \Phi_{AC}(\bar{r}) + k^2 \Phi_{AC}(\bar{r}) = \frac{-v}{D} S_{AC}, \quad (2.5)$$

where  $k$  is the complex photon density wavenumber (with  $j = \sqrt{-1}$ ),

$$k^2 = \frac{-v\mu_a + j\omega}{D}, \quad (2.6)$$

and  $S_{AC}$  is the source modulation amplitude. A time-dependent solution to Equation (2.5) may be expressed in the form [23] of the real portion of  $\Phi_{AC}(\bar{r}, t) = \Re[\Phi_{AC}(\bar{r})\exp(-j\omega t)]$ . From this expression, the oscillatory part of the solution for a homogeneous, infinite dense random medium with a modulated point source was determined to be [28]

$$\Phi_{AC}(\bar{r}) = \frac{vS_{AC}}{4\pi D|\bar{r} - \bar{r}'|} e^{jk|\bar{r} - \bar{r}'|}, \quad (2.7)$$

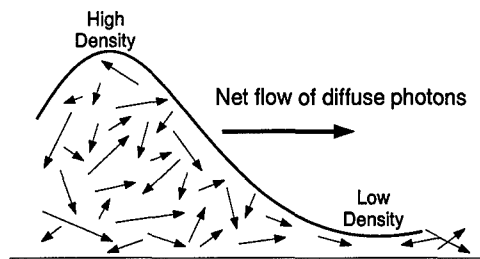


Figure 2.2 The DPDW propagates from regions with a high photon fluence rate (or energy density) to those with lower rates (energy density). The density of the photon wave is indicated on the amplitude of the solid curve. The directions of the individual photons are depicted by the arrows [53].

where this solution is referenced to the center of the spherical inhomogeneity which also coincides with the origin of the system. The unprimed variable ( $\bar{r}$ ) correlates to the location of the detector and the primed variable ( $\bar{r}'$ ) refers to the location of the source as seen in Figure 2.1. It is customary to drop the time-dependent term for this development. This solution is a highly damped wave which propagates with a single phase velocity and is referred to as a DPDW. This propagation is illustrated in Figure 2.2 where the density of the photons is denoted by the height of the solid curve, and the individual photon directions are depicted by the arrows [53].

Though the complex wavenumber indicates that the wave attenuates very rapidly within the medium, the wave possesses a well defined wavelength, amplitude and phase at all points [58]. The validity of the DPDW shows that the diffusional process of sinusoidally intensity-modulated light incident on a turbid medium can be treated within the framework of wave phenomena [10,28].

#### 2.4 Physics Model of Scattered DPDWs

In the presence of an inhomogeneity, the DPDW is distorted to a certain extent, depending on both the physical characteristics as well as the optical properties of the object. DPDWs have been extensively researched and shown to adhere to the standard models of wave behavior such as refraction [44], diffraction [11,28], scattering from localized heterogeneities [10], interference [17,51], and dispersion [54]. These properties of DPDWs have been verified in both biological models [28] and human breast studies [17]. Many of

the noted solutions above are only valid if the inhomogeneity is located between the source and detector. In addition, the object must have specific optical properties relative to its surrounding background. That is, the object must be highly absorptive relative to the background medium.

In this section, a physics model of the forward propagation of DPDWs is investigated. In particular, an analytic solution to the Helmholtz equation (Equation (2.5)) is discussed for the same piecewise homogeneous medium only now with a spherical object embedded in it. Unlike other solutions [11, 17, 28, 44, 51, 54] this solution is for a highly scattering inhomogeneity within another strongly scattering infinite medium, and later extended to a semi-infinite medium [12].

*2.4.1 An Analytic Solution.* The total field,  $\Phi$ , in a homogeneous medium outside an embedded spherical inhomogeneity is the summation of the incident field ( $\Phi_{AC}$ ) and the scattered field ( $\Phi_{SC}$ ) [35], meaning

$$\Phi = \Phi_{AC} + \Phi_{SC}, \quad (2.8)$$

where  $\Phi_{AC}$  results from the homogeneous background medium, and  $\Phi_{SC}$  results from the inhomogeneity. The Helmholtz equation (Equation (2.5)) was shown in Section 2.3 to describe DPDW propagation in piecewise homogeneous medium. With that basis and application of appropriate boundary conditions, the scattered field outside the inhomogeneity has the final form of a modal solution to Equation (2.5) involving spherical Bessel ( $j_l$ ) and Neumann functions ( $n_l$ ) of the first kind, and spherical harmonics of degree  $l$  and order  $m$  ( $Y_l^m$ ) [12], i.e.

$$\Phi_{SC}(\bar{r}) = \sum_{l=0}^{\infty} \sum_{m=-l}^l [A_{l,m} j_l(k_{out} r) + j A_{l,m} n_l(k_{out} r)] Y_l^m(\theta, \phi), \quad r \geq a. \quad (2.9)$$

Here the  $A_{l,m}$  coefficients are

$$A_{l,m} = -j \frac{v S_{AC} k_{out}}{D} h_l^{(1)}(k_{out} z_s) Y_{l,m}^*(\pi, 0) \times \left[ \frac{D_{out} k_{out} a j_l'(k_{out} a) j_l(k_{in} a) - D_{in} k_{in} a j_l(k_{out} a) j_l'(k_{in} a)}{D_{out} k_{out} a h_l^{(1)'}(k_{out} a) j_l(k_{in} a) - D_{in} k_{in} a h_l^{(1)}(k_{out} a) j_l'(k_{in} a)} \right], \quad (2.10)$$

where  $z_s$  is equivalent to the source distance along the  $z$ -axis,  $a$  is the radius of the spherical inhomogeneity, and  $D_{out}$  ( $D_{in}$ ) is the photon diffusion coefficient outside (inside) the sphere, and similarly  $k_{out}$  ( $k_{in}$ ) is the wavenumber outside (inside) the sphere.  $h_l^{(1)}$  is the spherical Hankel function of the first kind, type  $l$ , and  $h_l^{(1)'}$  and  $j_l'$  are the first derivatives of the spherical hankel and bessel functions respectively. Applying azimuthal symmetry about  $z = 0$  since the spherical object is at the origin leads to  $A_{l,m} = 0$  for  $m \neq 0$ . The scattered field simplifies to [12]

$$\begin{aligned} \Phi_{SC}(\bar{r}) &= \sum_{l=0}^{\infty} A_l [j_l(k_{out} r) + j_n l(k_{out} r)] Y_l^{(0)}(\theta, \phi) \\ &= \sum_{l=0}^{\infty} A_l h_l^{(1)}(k_{out} r) Y_l^{(0)}(\theta, \phi), \quad r \geq a. \end{aligned} \quad (2.11)$$

This solution is simpler but similar to the scalar version of Mie Theory for the scattering of electromagnetic waves from dielectric spheres [34].

In the numerical calculation of the scattered wave (Equation (2.11)), the number of moments to include of the infinite summation is important to consider. To better understand the dependent parameters in the scattered wave, consider the first three moments of Equation (2.11), namely the monopole ( $l = 0$ ), the dipole ( $l = 1$ ), and the quadrupole ( $l = 2$ ) moments which are, respectively,

$$\Phi_{SC}^{(l=0)}(\bar{r}) = -j A_0 \frac{e^{j k_{out} r}}{k_{out} r}, \quad (2.12)$$

$$\Phi_{SC}^{(l=1)}(\bar{r}) = A_1 \frac{e^{j k_{out} r}}{k_{out} r} \left( -1 - \frac{j}{k_{out} r} \right) \cos \theta, \quad (2.13)$$

$$\Phi_{SC}^{(l=2)}(\bar{r}) = A_2 \frac{e^{j k_{out} r}}{k_{out} r} \left( j - \frac{3}{k_{out} r} - \frac{3j}{(k_{out} r)^2} \right) \left[ \frac{1}{2} (3 \cos^2 \theta - 1) \right]. \quad (2.14)$$

To leading order in  $k_{out}a$  and  $k_{in}a$ , assuming  $|k_{out}a| \ll 1$  and  $|k_{in}a| \ll 1$ , these moments of the scattered wave evaluate to [13]:

$$\Phi_{SC}^{(l=0)}(\bar{r}) = \frac{vS_{AC}}{8\pi^2 D_{out}} \frac{e^{jkr}}{r} \frac{e^{jkr'}}{r'} \left[ \frac{4\pi a^3}{3} \right] \left[ \frac{-v\Delta\mu_a}{D_{out}} \right], \quad (2.15)$$

$$\begin{aligned} \Phi_{SC}^{(l=1)}(\bar{r}) &= \frac{vS_{AC}}{8\pi^2 D_{out}} \frac{e^{jkr}}{r} \frac{e^{jkr'}}{r'} \left[ jk - \frac{1}{r'} \right] \left[ jk - \frac{1}{r} \right] \left[ \frac{4\pi a^3}{3} \right] \\ &\quad \times \left[ \frac{-3 \cos \theta \Delta\mu'_s}{3\mu'_{s,out} + 2\Delta\mu'_s} \right], \end{aligned} \quad (2.16)$$

$$\begin{aligned} \Phi_{SC}^{(l=2)}(\bar{r}) &= \frac{vS_{AC}}{8\pi^2 D_{out}} \frac{e^{jkr}}{r} \frac{e^{jkr'}}{r'} \left[ k^2 + \frac{j3k}{r'} - \frac{3}{r'^2} \right] \left[ k^2 + \frac{j3k}{r} - \frac{3}{r^2} \right] \left[ \frac{4\pi a^5}{45} \right] \\ &\quad \times \left[ \frac{(3 \cos^2 \theta - 1) \Delta\mu'_s}{5\mu'_{s,out} + 3\Delta\mu'_s} \right]. \end{aligned} \quad (2.17)$$

The difference in the absorption coefficient of the inhomogeneity,  $\mu_{a,in}$ , and the absorption coefficient of the background,  $\mu_{a,out}$ , are expressed as  $\Delta\mu_a = \mu_{a,in} - \mu_{a,out}$ . Similarly,  $\Delta\mu'_s = \mu'_{s,in} - \mu'_{s,out}$ , where this is the difference between the reduced scattering coefficients of the inhomogeneity ( $\mu'_{s,in}$ ) and the background ( $\mu'_{s,out}$ ).

Note that the first moment, to leading order, depends only on the difference of the absorptive coefficients. The dipole and quadrupole moments, however, depend only on the difference of the reduced scattering coefficients. Generally, the detectable moments of the scattered DPDW depend on the optical contrasts of the object and the surrounding medium. These dependencies will be further explored in Chapters IV and V.

**2.4.2 Semi-Infinite Media.** In medical imaging, non-invasive methods are preferred and inherently involve boundaries between tissue and a non-scattering medium such as water or air. Treating this system as infinite as in Section 2.4.1 will certainly lead to a certain degree of inaccuracy since measurements are usually made by placing the source and detector against the tissue. This procedure creates the boundary between scattering and non-scattering media. Using the method of image sources, this system can be transformed into an equivalent infinite system which contains the real and image sources [46]. This transformation assumes a planar division and a boundary condition of  $\Phi = 0$  on an extrapolated zero boundary at a distance  $z_0 = 0.7104/\mu'_s$  from the actual boundary, away

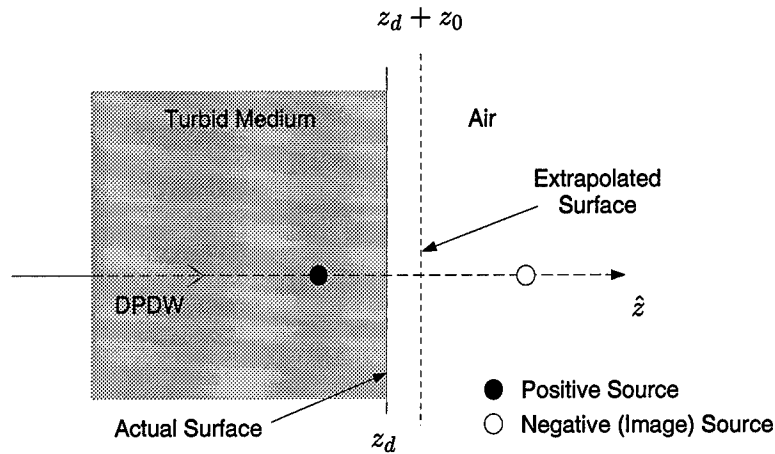


Figure 2.3 The source in the semi-infinite medium can be modeled with a negative source image centered about an extrapolated surface situated at a distance  $z_0$  from the actual boundary ( $z_d$ ) away from the turbid medium [19].

from the diffusive medium [12]. A distance of  $z_0 = 2/(3\mu'_s)$  has also been used [16,31,33,47]. A complete listing of appropriate diffusion-based values of  $z_0$  is presented by Aronson [3].

Figure 2.3 illustrates the geometry of the extrapolated surface. The  $z$ -plane boundary of the turbid medium is denoted by  $z_d$ , and the extrapolated boundary is at a distance  $z_d + z_0$ . An extrapolated zero boundary is a good approximation for the boundary conditions in the semi-infinite case. Experimental comparisons of the boundary model with the infinite model have demonstrated that the object sensitivity has not been affected [12].

**2.4.3 Resolution Limitations of the Analytic Solution.** An extensive analysis of the ability of DPDWs to detect and localize inhomogeneities was conducted by Boas *et al.* Their findings indicated that tumors as small as 0.3 cm in diameter can be unambiguously detected when  $\mu_a(\text{object}) > 3\mu_a(\text{background})$ , or 0.4 cm when  $\mu'_s(\text{object}) > 1.5\mu'_s(\text{background})$ . If the optical contrast of the tumor to the background medium is not known, then the detectable tumor diameter is on the order of 1.0 cm or larger [13].

## 2.5 Fourier Optics Model of Scattered DPDWs

An alternative approach to solving the forward propagation problem in the frequency domain is to apply the mathematical tool, Fourier analysis. This tool provides a means of

describing linear phenomena such as that occurring in the system of interest here. When applying Fourier theory on an imaging system where the information being mathematically represented is of a spatial nature (e.g. a light amplitude or intensity distribution over space), the theory is referred to as Fourier optics [32].

A new approach to localize an object in a turbid medium developed by Matson [40] uses Fourier optics theory. The approach localizes a spherical inhomogeneity in three dimensions using a single set of two-dimensional measurements. This solution method includes several new aspects that obviates the need for movement in the source-detector setup or the medium sample during measurements, unlike solutions mentioned in Section 2.4. Since only a single view is needed, position alignment inaccuracies are avoided, and ease-of-use for *in vivo* (internal) imaging in a clinical environment is maintained. Multiple detectors are phased in a manner such that the DPDW is scanned through the sample providing the lateral localization data of the inhomogeneity. Post-processing techniques are then used to determine the depth information.

In this section, the Fourier optics theoretical and algorithmic developments for the forward propagation of a DPDW in homogeneous media without and with an embedded scatterer are outlined. The reconstruction (or back-propagation) algorithm is also presented to show the application of the forward analysis. Resolution values as found through simulation are presented. In addition, current research being conducted to validate this novel approach is discussed.

*2.5.1 Wave Propagation in Source-Free Homogeneous Media.* An alternative solution to describing the light behavior in homogeneous turbid media can be found through Fourier optics due to the linear nature of the system. In Section 2.2, it was shown that light propagation in a given medium can be expressed through a solution to the diffusion equation (Equation (2.3)). For a point source, the result is a spherical damped outgoing wave. If the medium is a source-free vacuum, there is neither scattering nor absorption of the traveling light, and the solution to the diffusion equation is a non-damped wave. Light propagation in a source-free system can similarly be analyzed in a linear, space-invariant

(LSI) system [32]. Therefore, using the LSI framework, Fourier theory can be applied to determine the behavior of the traveling light.

In this Fourier optics approach, the Fourier transform for two independent variables  $x$  and  $y$  will be represented by  $\mathcal{F}\{g\}$  and is defined by

$$\mathcal{F}\{g\} = \int_{-\infty}^{\infty} \int_{-\infty}^{\infty} g(x, y) e^{-j2\pi(f_x x + f_y y)} dx dy. \quad (2.18)$$

Similarly, the inverse Fourier transform of a function  $G(f_x, f_y)$ , represented by  $\mathcal{F}^{-1}\{G\}$ , is defined as

$$\mathcal{F}^{-1}\{G\} = \int_{-\infty}^{\infty} \int_{-\infty}^{\infty} G(f_x, f_y) e^{j2\pi(f_x x + f_y y)} df_x df_y. \quad (2.19)$$

Since the Fourier transform is a linear operator, and the incident and scattered fields are linear systems, Fourier transform properties can be used.

Consider an incident DPDW in the  $(x, y)$  plane, created by an unspecified system of sources, and traveling in an infinite homogeneous turbid medium in the positive  $\hat{z}$  direction. Since the DPDW satisfies the Helmholtz equation (Equation (2.5)), let it be represented by  $U(x, y; z = 0)$  across the  $z = 0$  plane and its two-dimensional Fourier transform be given by

$$A_0(f_x, f_y; 0) = \int_{-\infty}^{\infty} \int_{-\infty}^{\infty} U(x, y; 0) e^{-j2\pi(f_x x + f_y y)} dx dy, \quad (2.20)$$

where  $f_x$  and  $f_y$  are spatial frequency variables. At a parallel plane of positive distance  $z$ , let  $A_z(f_x, f_y)$  be the two-dimensional Fourier transform of the scattered field  $U(x, y, z)$ . In other words, the spatial Fourier components are a collection of various plane waves propagating in different directions away from a specified  $z$  plane. The amplitude of those Fourier components across any other plane can be identified as the superposition of these plane waves with the appropriate phase shifts incurred during propagation. The relationship of the Fourier components in different parallel planes is shown to be [32]

$$A_z(f_x, f_y) = A_0(f_x, f_y; 0) e^{jz\sqrt{k^2 - (2\pi f_x)^2 - (2\pi f_y)^2}}. \quad (2.21)$$

Within this LSI system, the transfer function,  $H_z(f_x, f_y)$ , that characterizes the wave propagation is [40]

$$\begin{aligned} H_z(f_x, f_y; z) &\equiv \frac{A_z(f_x, f_y)}{A_0(f_x, f_y; 0)} \\ &= e^{jz\sqrt{k^2 - (2\pi f_x)^2 - (2\pi f_y)^2}}. \end{aligned} \quad (2.22)$$

In a medium without embedded inhomogeneities, the scattered photon density wave can be constructed through the following relationship [40]:

$$U(x, y; z) = \mathcal{F}^{-1} \left\{ \frac{A_z(f_x, f_y; z_d)}{H_z(f_x, f_y; z)} \right\} \quad (2.23)$$

where  $z_d$  corresponds to the measurement (or detector) plane, and  $z$  is the location of the plane of interest. Essentially, Equation (2.23) means that the incident wave can be mapped from one  $z$  plane to another, taking into account scattering and propagation effects.

*2.5.2 Wave Propagation in Heterogeneous Media.* Considering an embedded spherical inhomogeneity in an otherwise piece-wise homogeneous medium, Equation (2.23) is valid only up to the plane containing the object. To model the diffraction caused by the spherical object, an equivalent dispersive disk of the same diameter can replace the object in the plane containing the center of the object [40]. The ray optic model in conventional optics is of limited applicability since the measurements of the perturbed wave are in the near field. Typically the model only works well for inhomogeneities that are not highly absorptive or dense, and have a larger diffusion coefficient relative to the background medium [10]. If the inhomogeneity is replaced with this ray optic model, then Equation (2.23) is valid only up to the plane containing the center of the object. The diffraction from this disk is similar to a thin lens with a different wavenumber value ( $k_{in}$ ) than the surrounding medium ( $k_{out}$ ). The transmittance function associated with a thin lens,  $t_A$ , has been shown to be [32]

$$t_A = e^{j\Delta k R}, \quad (2.24)$$

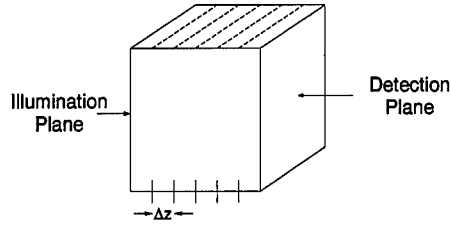


Figure 2.4 The photon density wave is reconstructed along planar slices (dashed lines) parallel to the measurement plane. Each slice is spaced a specified interval  $\Delta z$  [40].

where  $\Delta k$  is the difference between the wavenumber inside and outside the inhomogeneity (e.g.  $\Delta k = k_{in} - k_{out}$ ),  $R$  is the distance through the inhomogeneity at  $(x, y)$ , specifically

$$R = 2\sqrt{a^2 - (x - x')^2 - (y - y')^2}, \quad (2.25)$$

where the primed and unprimed coordinates are defined as in Figure 2.1. The homogeneous wave is transmitted through the plane containing the lens model. The remaining medium to the right of the inhomogeneity is homogeneous, so the now perturbed wave can be propagated as in Equation (2.21).

**2.5.3 Reconstruction Algorithm.** To determine the lateral location of the inhomogeneity, the photon density wave that is due to the background medium is subtracted from the detected photon density wave (Equation (2.8)). The lateral information in the detection plane (Figure 2.4) can be determined from either the resulting amplitude or phase of the scattered photon density wave.

For depth information, the photon density wave must be reconstructed by calculating planar slices of the medium parallel to the measurement plane via Equation (2.22) at specified intervals of  $\Delta z$ . Equation (2.23) is valid only up to the plane containing the center of the inhomogeneity. At that point, there is a singularity, and the reconstructed photon density wave peaks. By determining where the photon density wave peaks along the  $\hat{z}$  axis, the depth of the inhomogeneity can be found [40]. Figure 2.4 illustrates this reconstruction geometry [40].

Equation (2.23) is the basic algorithm, but it is modified to include a stabilizing factor for two reasons. First, the exponential fall-off of the transfer function causes the reconstructed Fourier spectra to become unstable. Secondly, when over 1.0 cm or more into the volume, computer-roundoff error and any noise introduced into the system become significant. A pillbox filter can be applied to pass the unattenuated reconstructed Fourier spectra within a limited radial distance around the origin to attain system stability. Another correction is made to the algorithm since exponential attenuation of the DPDW within the turbid media limits the dynamic range of the image intensities during reconstruction. To remain within the dynamic range of the reconstructed image the reconstructed wave intensity is normalized by the energy in the wave at the plane of interest [40].

*2.5.4 Simulated Results.* Using the algorithm described in the previous section, computer simulation results [40] demonstrated the validity of the methodology to localize a spherical object embedded in an infinite homogeneous medium. With mammography in mind, the medium was modeled after human breast tissue with a spherical tumor located at multiple positions. The surrounding background breast tissue was characterized at 700 nm light with a reduced scattering and absorption coefficients of 14.0 and 0.035  $\text{cm}^{-1}$ , respectively [58]. The tumor is modeled with carcinoma tissue parameters characterized at a wavelength of 780 nm and had reduced scattering and absorption coefficients of 12.0 and 0.5  $\text{cm}^{-1}$ , respectively. The radius of the tumor was set at 0.5 cm [48]. The source was modeled as a point source with an amplitude modulation of 1 GHz, giving a DPDW wavelength of 2.67 cm. The source's closest point in the detection plane was 5 cm. Zero-mean complex Gaussian noise with 1% amplitude and 1° phase standard deviations was added to computer-simulated data generated with a previously developed code [12, 40, 49].

Under these simulated conditions, the lateral localization of the 1.0 cm diameter tumor was accurate but dependent on the amount of noise in the system. Using the algorithm outlined in Section 2.5.3 with an interval distance  $\Delta z = 0.125$  cm, the depth of the tumor was identifiable up to 3.0 cm into the tissue from the detection plane. Resolution decreased as depth increased, but within a few millimeters, the center of the tumor was still determined.

*2.5.5 Experimental Results.* Physical measurements were conducted to validate the algorithm outlined in Section 2.5.3. The setup consisted of a single amplitude-modulated light source, a multiple detector array, and a series of tissue phantoms (plastic resin with  $\text{TiO}_2$  powder and NIR dye) containing various “tumors” in the forms of different colored beads. The colors provided various absorption properties that contrasted with the surrounding medium. The modulation has been lowered from 1 GHz in the simulated experiments down to 20-40 MHz where preliminary measurements showed more conclusive results. The experimental results demonstrated the ability of the algorithm to detect and localize various heterogeneities with different optical properties relative to the surrounding medium [38].

### III. An Analytic Transfer Function

#### 3.1 Introduction

There are several methods of determining the behavior of light propagation in turbid media as was shown in Chapter II. Two particular methods yielded solutions that were investigated in some detail.

The analytic solution solved the Helmholtz equation for both an incident wave in a homogeneous turbid medium and a scattered wave off an inhomogeneity. This solution is in the form of a multipole expansion of spherical harmonics.

An alternate method applied the theory of Fourier analysis to represent the wave in different regions of the turbid medium. In one of the regions, a transfer function can be applied to propagate the perturbed wave through the media.

In this chapter, the objective is to determine a single transfer function that can be applied to the entire system by using the analytic solution results.

#### 3.2 Transfer Function Formulation

In linear systems, for a given input and output pair, there is a transform that can be applied to the input to yield the given output. Figure 3.1 illustrates this process. For this transfer function development, the system that is under consideration has been shown that it can be modeled as a linear system [32]. The input to the system is a point source of intensity modulated light, and the output can be modeled in two ways. The first being in the form of an analytic solution as discussed in Section 2.4. The other is the Fourier optics representation as presented in Section 2.5.

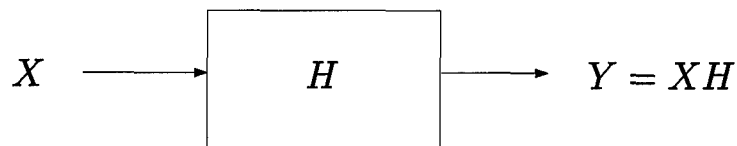


Figure 3.1 In a linear system, for a given input  $X$ , a transfer function  $H$  can be applied to yield the output  $Y$ .

The performance of both solutions have been demonstrated to detect and localize inhomogeneities within a turbid medium within a few millimeters [12,40]. Since the model of the inhomogeneity is different in the analytic solution and the Fourier optics solution, the systems are not the same. The Fourier optics solution is applied piece-wise to three regions: the homogeneous medium to the left of the inhomogeneity, the heterogeneous medium which contains the inhomogeneity, and the homogeneous medium to the right of the inhomogeneity. The transfer function in the Fourier optics solution can only be applied to the homogeneous regions. The analytic solution system encompasses the entire heterogeneous medium comprised of both the background and inhomogeneity. Thus the analytic solution can be used to determine a transfer function for the entire system.

Since the total field outside the inhomogeneity is a superposition of the incident and scattered waves (Equation (2.8)), then via the linearity property of Fourier transforms, the Fourier transform of the total wave, represented by  $\mathcal{F}\{\Phi\}$ , is simply a superposition of the individual Fourier transforms of the incident ( $\Phi_{AC}$ ) and scattered ( $\Phi_{SC}$ ) waves. Meaning,

$$\mathcal{F}\{\Phi\} = \mathcal{F}\{\Phi_{AC}\} + \mathcal{F}\{\Phi_{SC}\}. \quad (3.1)$$

Rearranging terms, Equation (3.1) can be rewritten as

$$\mathcal{F}\{\Phi\} = \mathcal{F}\{\Phi_{AC}\} \left\{ 1 + \frac{\mathcal{F}\{\Phi_{SC}\}}{\mathcal{F}\{\Phi_{AC}\}} \right\}, \quad (3.2)$$

provided  $1/\mathcal{F}\{\Phi_{AC}\}$  exists. The right bracketed term in Equation (3.2) is the transfer function. The analytic form of the transfer function is the ultimate objective of this chapter. The Fourier transforms for the incident and the scattered waves will be developed and the transfer function then determined.

Throughout these developments, the Fourier transform for two independent variables  $x$  and  $y$  will be represented by  $\mathcal{F}\{g\}$  and is defined by

$$\mathcal{F}\{g\} = \int_{-\infty}^{\infty} \int_{-\infty}^{\infty} g(x, y) e^{-j(\xi x + \eta y)} dx dy. \quad (3.3)$$

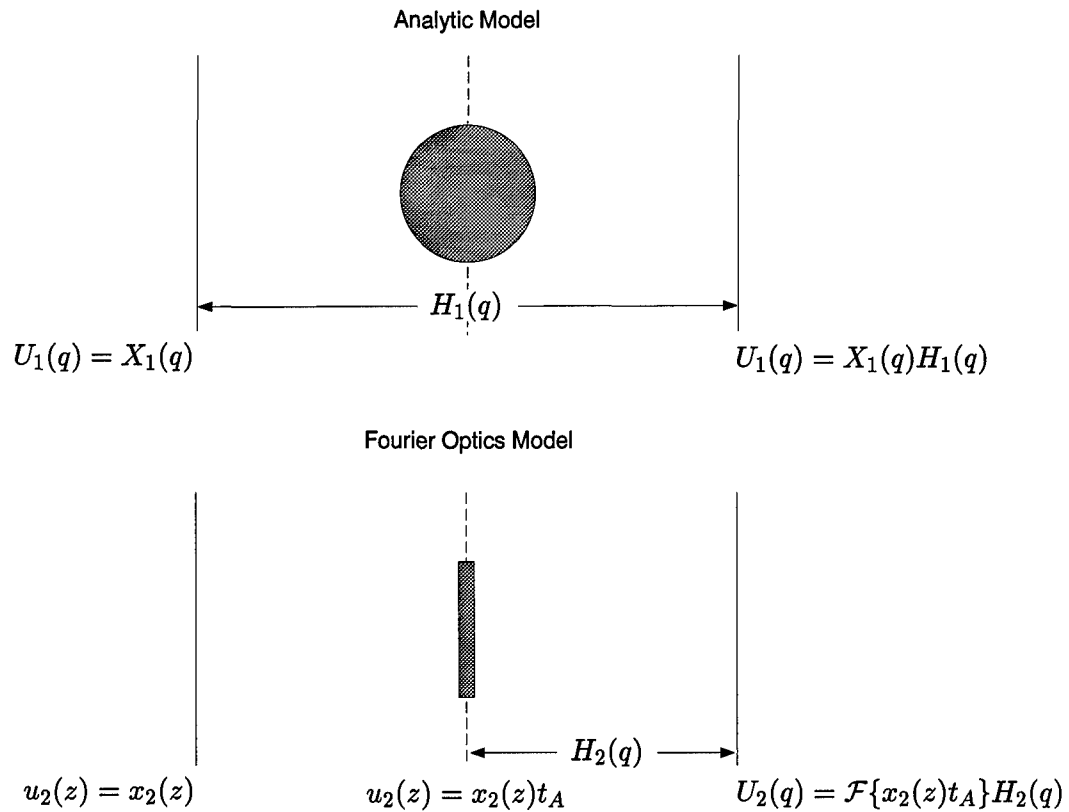


Figure 3.2 The top system depicts the analytic solution model as a linear system represented by an input,  $X_1(q)$ , propagated through the medium containing a spherical inhomogeneity by a transform function,  $H_1(q)$ , to become the output,  $U_1(q)$ . The Fourier optics model in the bottom system shows an incident wave through homogeneous medium and a thin lens approximation of a spherical inhomogeneity ( $t_A$ ), and propagated out of the medium by  $H_2(q)$ . The two systems are not equivalent due to the different models of the spherical inhomogeneity.

Similarly, the inverse Fourier transform of a function  $G(\xi, \eta)$ , represented by  $\mathcal{F}^{-1}\{G\}$ , is defined as<sup>1</sup>

$$\mathcal{F}^{-1}\{G\} = \frac{1}{(2\pi)^2} \int_{-\infty}^{\infty} \int_{-\infty}^{\infty} G(\xi, \eta) e^{j(\xi x + \eta y)} d\xi d\eta. \quad (3.4)$$

<sup>1</sup>This transform definition differs slightly from that defined in Chapter II. The difference is in a scale factor which does not change the properties of the transform.

### 3.3 Decomposition of a Spherical Wave Into Plane Waves

The difficulty of the problem of a spherical wave on a plane interface is due to the difference between the symmetries of the wave and the form of the boundary. While the incident wave caused by a point source has spherical symmetry, the boundary (detector) is a plane. It is natural to express the spherical wave in terms of plane waves in the desired Cartesian coordinate system in order to evaluate the wave on the planar boundary.

Consider an optically dense homogeneous medium with a spherical inhomogeneity composed of a highly scattering medium and whose center is located at the origin of a Cartesian coordinate system  $(x, y, z)$ . A diffuse photon density wave (DPDW) is assumed incident in the direction of the  $+\hat{z}$  axis and is observed at a detector position in the region bounded by  $z \geq a$ , where  $a$  is the radius of the inhomogeneity.

In this section, the plane wave formulation of the incident wave and the scattered wave from the spherical object are investigated.

**3.3.1 Incident Field Representation.** To obtain the incident wave in Equation (2.7), the scalar Green's function was used to solve the Helmholtz equation (Equation (2.5)). The Green's function has been shown to have an equivalent triple integral representation [5, 56], e.g.

$$\frac{e^{jk|\bar{r}-\bar{r}'|}}{|\bar{r}-\bar{r}'|} = \frac{1}{2\pi^2} \int_{-\infty}^{\infty} \int_{-\infty}^{\infty} \int_{-\infty}^{\infty} \frac{e^{j[\xi(x-x')+\eta(y-y')+\zeta(z-z')]} d\xi d\eta d\zeta. \quad (3.5)$$

The unprimed variable ( $\bar{r}$ ) indicates the distance to the detector and the primed variable ( $\bar{r}'$ ) is the distance to the source as seen in Figure 2.1. The complex wave number of the medium is denoted by  $k$ . The path of integration for each of the three complex variables  $\xi$ ,  $\eta$ , and  $\zeta$  is the corresponding real axis. To keep the frequency variables  $\xi$  and  $\eta$  vigorously real, the third variable  $\zeta$  needs to be bounded by a strip region  $-\Im(k) < \Im(\zeta) < \Im(k)$  in order to keep the function analytic, where  $\Im(\cdot)$  is the imaginary part of the complex number. This boundary assumes that there is some dissipation in the medium, however small, i.e. that  $k$  has a positive imaginary part.

Let  $\gamma$  be defined as

$$\begin{aligned}\gamma &= \sqrt{\xi^2 + \eta^2 - k^2}, & \text{if } \xi^2 + \eta^2 > k^2, \\ \gamma &= -j\sqrt{k^2 - \xi^2 - \eta^2}, & \text{if } \xi^2 + \eta^2 \leq k^2.\end{aligned}\quad (3.6)$$

This definition requires the real part of the square root to be greater than zero. The constraints on  $\gamma$  are valid in that the right side of Equation (3.5) satisfies the Helmholtz wave equation and gives the correct value of the field at  $z = z'$  [14]. However, in a turbid medium the real part of  $k^2$  is always negative, and the imaginary part is always positive [12]. This means that the second constraint in Equation (3.6) will never occur. As a result, the expression for  $\gamma$  can be simplified to

$$\gamma = \Re\left(\sqrt{\xi^2 + \eta^2 - k^2}\right) + j\Im\left(\sqrt{\xi^2 + \eta^2 - k^2}\right), \quad (3.7)$$

where  $\Re(\cdot)$  denotes the real part of a complex number [39]. Integrating Equation (3.5) with respect to  $\zeta$ , the double integral representation results as [5]

$$\frac{e^{jk|\bar{r}-\bar{r}'|}}{|\bar{r}-\bar{r}'|} = \frac{1}{2\pi} \int_{-\infty}^{\infty} \int_{-\infty}^{\infty} \frac{1}{\gamma} e^{-\gamma|z-z'|+j[\xi(x-x')+\eta(y-y')]} d\xi d\eta. \quad (3.8)$$

The elegant result of Equation (3.8) is a decomposition of a spherical wave into a superposition of elementary plane waves in the  $\hat{x}$  and  $\hat{y}$  directions as indicated by the exponent. The waves exponentially attenuate in the two directions away from the plane  $z = z'$  which contains the source.

In keeping the transform coordinates arbitrary in Equation (3.8), the incident field in Equation (2.7) can be rewritten as

$$\Phi_{AC}(\bar{r}, \bar{r}') = \frac{vS_{AC}}{8\pi^2 D} \int_{-\infty}^{\infty} \int_{-\infty}^{\infty} \frac{1}{\gamma} e^{-\gamma(z-z')+j[\xi(x-x')+\eta(y-y')]} d\xi d\eta, \quad z - z' > 0, \quad (3.9)$$

where  $v$  is the speed of light in the medium,  $S_{AC}$  is the source modulation amplitude, and  $D$  is the diffusion coefficient. The system geometry in this research dictates that the source and detector will be on opposite sides of the inhomogeneity, and the incident wave travels

in the positive  $\hat{z}$  direction. Thus  $z > z'$  in all cases, and so the absolute value operator in the exponent of Equation (3.8) is replaced with its argument.

**3.3.2 Scattered Field Reformulation.** The scattered wave off of a spherical inhomogeneity was determined to be a multipole expansion involving spherical functions. To simplify the notation, the scattered wave result in Equation (2.11) is rewritten as

$$\Phi_{SC}(\bar{r}) = \sum_{l=0}^{\infty} A_l \Pi_l^{(0)}(\bar{r}), \quad r \geq a, \quad (3.10)$$

where the abbreviation  $\Pi_l^{(0)}$ , in spherical coordinates  $\bar{r}(r, \theta, \phi)$ , is defined as

$$\Pi_l^{(0)}(\bar{r}) = \sqrt{\frac{2l+1}{4\pi}} h_l^{(1)}(kr) P_l(\cos \theta), \quad r \geq a. \quad (3.11)$$

Here,  $h_l^{(1)}$  is the spherical hankel function of the first kind, type  $l$ , and the zonal (or sectoral) spherical harmonics (order  $m = 0$ ) have been replaced with the equivalent Legendre polynomials,  $P_l$ , and normalization factor [1, 7]. The coefficients  $A_l$  are defined in Equation (2.10). As before,  $k$  is the wavenumber of the surrounding medium. The superscript (0) will be assumed to carry throughout the rest of the derivation. The objective is to rewrite Equation (3.11) into a plane wave expansion in Cartesian coordinates. To that end, Equation (3.11) can be expressed in an integral format as [42]

$$\Pi_l = \frac{1}{2\pi j^l} \sqrt{\frac{2l+1}{4\pi}} \int_0^{2\pi} d\beta \int_B e^{j\bar{k}\cdot\bar{r}} P_l(\cos \alpha) \sin \alpha d\alpha. \quad (3.12)$$

The contour  $B$  is chosen to be from  $\epsilon \rightarrow -j\infty + \epsilon$ ,  $0 < \epsilon < \frac{\pi}{2}$ , as illustrated in Figure 3.3. The vector  $\bar{k}$  is of length  $k$  and has the complex spherical angle  $\alpha$  and real spherical angle  $\beta$ . It should be noted that  $j^l$  is the imaginary number  $\sqrt{-1}$  to the power of  $l$  and is not to be confused with  $j_l$  which is the spherical bessel function of order  $l$ . Using the spherical

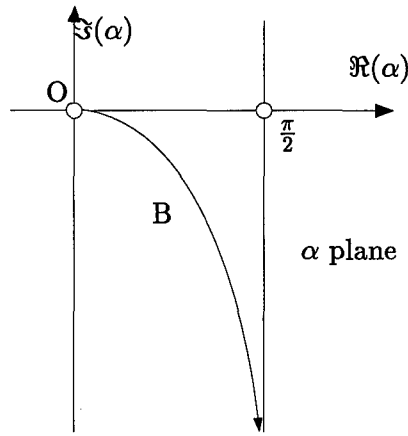


Figure 3.3 The path of integration denoted by  $B$  in the  $\alpha$  plane corresponds to the positive half of the real axis in the  $\lambda$  plane. [23,42].

coordinate to rectilinear transform variables, namely

$$\begin{aligned}
 r &= \sqrt{x^2 + y^2 + z^2}, & x &= r \sin \theta \cos \phi, \\
 \theta &= \cos^{-1}\left(\frac{z}{r}\right), & y &= r \sin \theta \sin \phi, \\
 \phi &= \tan^{-1}\left(\frac{y}{x}\right), & z &= r \cos \theta,
 \end{aligned} \tag{3.13}$$

the dot product in the exponent in Equation (3.12) is given by

$$\begin{aligned}
 \bar{k} \cdot \bar{r} &= kr [\cos \theta \cos \alpha + \sin \alpha \cos \beta \sin \theta \cos \phi + \sin \alpha \sin \beta \sin \theta \sin \phi], \\
 &= k [z \cos \alpha + x \sin \alpha \cos \beta + y \sin \alpha \sin \beta].
 \end{aligned} \tag{3.14}$$

Substituting Equation (3.14) into Equation (3.12), the result is

$$\Pi_l = \frac{1}{2\pi j^l} \sqrt{\frac{2l+1}{4\pi}} \int_0^{2\pi} d\beta \int_B e^{jk(z \cos \alpha + x \sin \alpha \cos \beta + y \sin \alpha \sin \beta)} P_l(\cos \alpha) \sin \alpha d\alpha. \tag{3.15}$$

From this spherical representation in transform space, a conformal transformation into

polar coordinates is defined as

$$\begin{aligned}\lambda &= k \sin \alpha, & d\lambda &= k \cos \alpha d\alpha; \\ \gamma &= -\sqrt{\lambda^2 - k^2} = -jk \cos \alpha,\end{aligned}\quad (3.16)$$

where the path of integration in the  $\lambda$  plane is restricted along the positive half of the real axis, e.g.  $0 \leq \lambda < \infty$ . This path corresponds to mapping onto the curve in Figure 3.3 which depicts the  $\alpha$  plane [23]. Under the assumption that there is some absorption in the medium ( $\Im(k) > 0$ ), the integral will converge along the path of integration illustrated in Figure 3.3. Making the conformal transformation in Equation (3.16), the expression in Equation (3.15) becomes

$$\Pi_l = \frac{1}{2\pi j^l} \frac{1}{jk} \sqrt{\frac{2l+1}{4\pi}} \int_0^{2\pi} d\beta \int_0^\infty \frac{1}{\gamma} e^{-\gamma z} e^{j(x\lambda \cos \beta + y\lambda \sin \beta)} P_l \left( \frac{j\gamma}{k} \right) \lambda d\lambda. \quad (3.17)$$

The result in Equation (3.17) is in the same form as the double integral of Equation (3.8). Let the frequency variables  $\xi = \lambda \cos \beta$  and  $\eta = \lambda \sin \beta$ , where  $\lambda = \sqrt{\xi^2 + \eta^2}$  and  $\lambda d\lambda d\beta = d\xi d\eta$ . Note that  $\xi$  and  $\eta$  are real transform variables, so the limits of integration are now over the entire real axis. Using these transform variables, Equation (3.17) can be rewritten as

$$\Pi_l = \frac{1}{2\pi j^l} \frac{1}{jk} \sqrt{\frac{2l+1}{4\pi}} \int_{-\infty}^\infty \int_{-\infty}^\infty \frac{1}{\gamma} e^{-\gamma z} e^{j(\xi x + \eta y)} P_l \left( \frac{j\gamma}{k} \right) d\xi d\eta. \quad (3.18)$$

Using the results in Equation (3.18), the scattered wave (Equation (2.11)) can now be expanded into a superposition of ordinary plane waves in Cartesian coordinates, namely,

$$\Phi_{SC}(\vec{r}) = \sum_{l=0}^{\infty} \sqrt{\frac{2l+1}{4\pi}} \frac{A_l}{2\pi k j^{l+1}} \int_{-\infty}^\infty \int_{-\infty}^\infty \frac{1}{\gamma} e^{-\gamma z} e^{j(\xi x + \eta y)} P_l \left( \frac{j\gamma}{k} \right) d\xi d\eta, \quad |z| \geq a \quad (3.19)$$

It must be noted here that the multipole expansion of Equation (2.11) and the plane wave expansion in Equation (3.19) have different regions of validity. The multipole expansion is

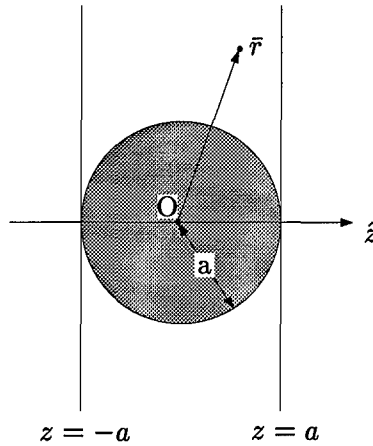


Figure 3.4 The multipole expansion is valid throughout the region  $r \geq a$ , but the plane wave expansion is valid on  $|z| \geq a$  [23].

valid outside the inhomogeneity on  $r \geq a$ . The integral expression represents the scattered DPDW outside the strip  $|z| < a$  [23]. Figure 3.4 illustrates these two regions.

### 3.4 Fourier Transform of the Analytic Solution

Since the Fourier transform is a linear operator, and the incident and scattered fields are linear systems, Fourier transform properties can be used. In this section, the two-dimensional Fourier transform in Section 3.2 is found using the incident and scattered wave expressions developed in the previous section.

**3.4.1 Incident Wave.** For the two dimensional Fourier transform development of the incident DPDW, let  $C_o(\xi, \eta; z, z')$  be defined as

$$C_o(\xi, \eta; z, z') = \frac{1}{\gamma} e^{-\gamma(z-z')}, \quad z - z' > 0, \quad (3.20)$$

so that Equation (3.9) becomes

$$\Phi_{AC}(\bar{r}, \bar{r}') = \frac{vS_{AC}}{8\pi^2 D} \int_{-\infty}^{\infty} \int_{-\infty}^{\infty} C_o(\xi, \eta; z, z') e^{j(\xi x + \eta y)} d\xi d\eta, \quad z - z' > 0. \quad (3.21)$$

Note that it is assumed that the incident wave source location is at (0,0) in the  $\hat{x}'$ - $\hat{y}'$  plane. In Equation (3.21) the form for a two-dimensional Fourier transform of the incident wave,

$U_{AC}$ , is readily apparent via Equation (3.4), e.g.

$$U_{AC}(\xi, \eta; z') = \frac{vS_{AC}}{2D} C_o(\xi, \eta; z, z'), \quad z - z' > 0. \quad (3.22)$$

It is interesting to note that even though the incident wave is singular at the source location, the non-zero imaginary component of  $k$  and the real frequencies,  $\xi$  and  $\eta$ , keep  $\gamma$  from becoming zero.

**3.4.2 Scattered Wave.** Similarly for the two-dimensional Fourier transform development of the scattered wave, let  $C_z(\xi, \eta; z)$  be defined as follows:

$$C_z(\xi, \eta; z) = \frac{1}{\gamma} e^{-\gamma z} P_l \left( \frac{j\gamma}{k} \right). \quad (3.23)$$

Using the definition in Equation (3.23) and the results in Equation (3.19), the scattered wave can be expressed as

$$\Phi_{SC}(\bar{r}) = \sum_{l=0}^{\infty} \sqrt{\frac{2l+1}{4\pi}} \frac{A_l}{2\pi k j^{l+1}} \int_{-\infty}^{\infty} \int_{-\infty}^{\infty} C_z(\xi, \eta; z) e^{j(\xi x + \eta y)} d\xi d\eta, \quad |z| \geq a. \quad (3.24)$$

From Equation (3.4), the two-dimensional Fourier transform of the scattered wave in Equation (3.24),  $U_{SC}$ , is

$$U_{SC}(\xi, \eta; z) = \sum_{l=0}^{\infty} \frac{2\pi}{k j^{l+1}} \sqrt{\frac{2l+1}{4\pi}} A_l C_z(\xi, \eta; z), \quad |z| \geq a, \quad (3.25)$$

where the constant terms have been brought inside the Fourier integral.

**3.4.3 Transfer Function.** Using the results in Equations (3.22) and (3.25), the transfer function can be determined from Equation (3.2). Thus, the analytic form of the transfer function is

$$H(\xi, \eta; z, z') = 1 + \sum_{l=0}^{\infty} \frac{4\pi D}{v k S_{AC} j^{l+1}} \sqrt{\frac{2l+1}{4\pi}} A_l P_l \left( \frac{j\gamma}{k} \right) e^{-\gamma z'}, \quad |z| \geq a, \quad z > z'. \quad (3.26)$$

This transfer function indicates that the piece-wise homogeneous medium with an embedded spherical inhomogeneity is characterized by the location of the source along the  $\hat{z}$  axis as well as by the Legendre polynomials in the  $(\xi, \eta)$  plane. The phase is further affected by the  $1/k$ ,  $A_l$  and  $P_l$  factors since these are complex values.

### 3.5 Summary

In this chapter, an analytic transfer function was determined for a system of infinite homogeneous turbid medium with a spherical inhomogeneity situated at the origin. The transfer function completely characterizes this system so that an input DPDW can be applied to produce a corresponding perturbed output wave at a detector plane. The transfer function shows that some of the three-dimensional Fourier components of the system may be determined directly from knowing the two-dimensional Fourier components in the detector plane. It is then possible to determine the three-dimensional structure of the inhomogeneity with only the measurements in the detector plane.

## *IV. Implementation of Transfer Function Models and Test Plan*

### *4.1 Introduction*

Two, among the many, exact methods of determining the total output wave in a homogeneous turbid media containing a spherical inhomogeneity are simulated in this chapter. These methods include direct calculation using Boas's results in Equation (2.11), and by using Fourier methods in Equation (3.2). The two codes developed to perform both methods of wave generation are referred to as the "analytic solution" for Boas's results and the "analytic transfer function" for the Fourier optics approach. The total wave outputs of each code are correlated to determine the validity of the simulation methods. In addition to these exact models, Goodman's propagation method is also modeled [32]. The plane wave propagation approach can be accurately applied to the movement of a wave through homogeneous media. The wave is represented as a superposition of plane waves, and its propagation through homogeneous media can be characterized by a transfer function. However, in the presence of an embedded spherical inhomogeneity, this approach becomes an approximation since the system is no longer homogeneous. By comparing the exact analytic transfer function model to the transfer function characterization by Goodman for inhomogeneous media, the relative error can be determined for the plane wave approximation.

In this chapter, the system geometry is described and the method of wave comparison is introduced. The implementation of each model of wave propagation is simulated and validated. In addition to the simulation code descriptions, this chapter outlines in a test plan the various optical parameters that will be used to analyze the behavior of the analytic transfer function from the Fourier optics method. Following the test plan, the validity of the wave propagation model developed by Goodman is determined.

### *4.2 System Geometry*

The system geometry is consistently structured throughout all of the simulations and analysis of the models of wave propagation. The sample size is 5 cm  $\times$  5 cm  $\times$  5 cm and is modeled as an infinite homogeneous, turbid medium with a point source located along

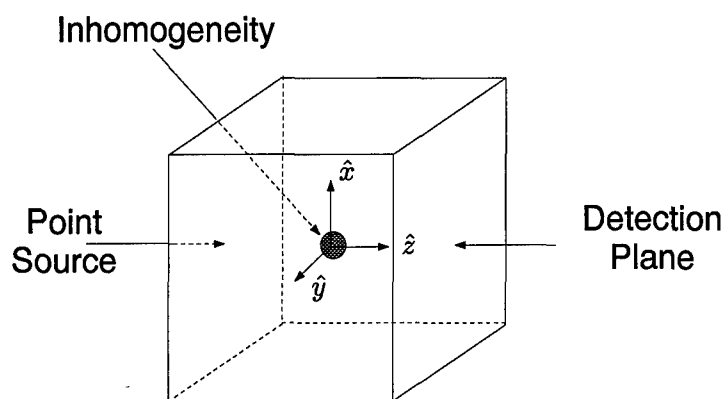


Figure 4.1 A spherical inhomogeneity is located at the origin of the system. A point source is incident at 2 cm to the left ( $-\hat{z}$  direction) and the detector plane is 3 cm to the right ( $+\hat{z}$  direction) of the inhomogeneity. The source location nor the origin are included in the system analysis due to the associated singularities. Increment division along all axes is 0.125 cm.

the  $-\hat{z}$ -axis. A spherical inhomogeneity is located at the origin of the system, 2 cm from the source and 3 cm from the detector plane along the  $\hat{z}$ -axis. The sampling interval along both the  $\hat{x}$  and  $\hat{y}$ -axes is 0.125 cm. Along the  $\hat{z}$ -axis, the sampling interval is also 0.125 cm, but neither the origin of the inhomogeneity or the source location is included in order to avoid singularities in the calculation of the scattered and incident waves respectively. This geometry is illustrated in Figure 4.1.

### 4.3 Approximations in Simulations

**4.3.1 Series Truncation.** To implement the exact analytic solution numerically, the infinite series in Equation (2.11) is truncated at a user-defined limit. If the conditions  $|k_{out}a| \ll 1$  and  $|k_{in}a| \ll 1$  are valid, where  $k_{out}$  ( $k_{in}$ ) is the wavenumber outside (inside) the inhomogeneity with radius  $a$ , only the first three moments of the series are detectable in experiments due to signal-to-noise limitations [13]. These three moments are dependent on the absorptive and scattering properties of the inhomogeneity. To leading order, the first moment (monopole) depends on the difference of the absorption coefficients inside and outside the inhomogeneity. The second moment (dipole) and the third moment (quadrupole) depend on the difference of the reduced scattering coefficients inside and outside the inhomogeneity (see Section 2.5.2 for development).

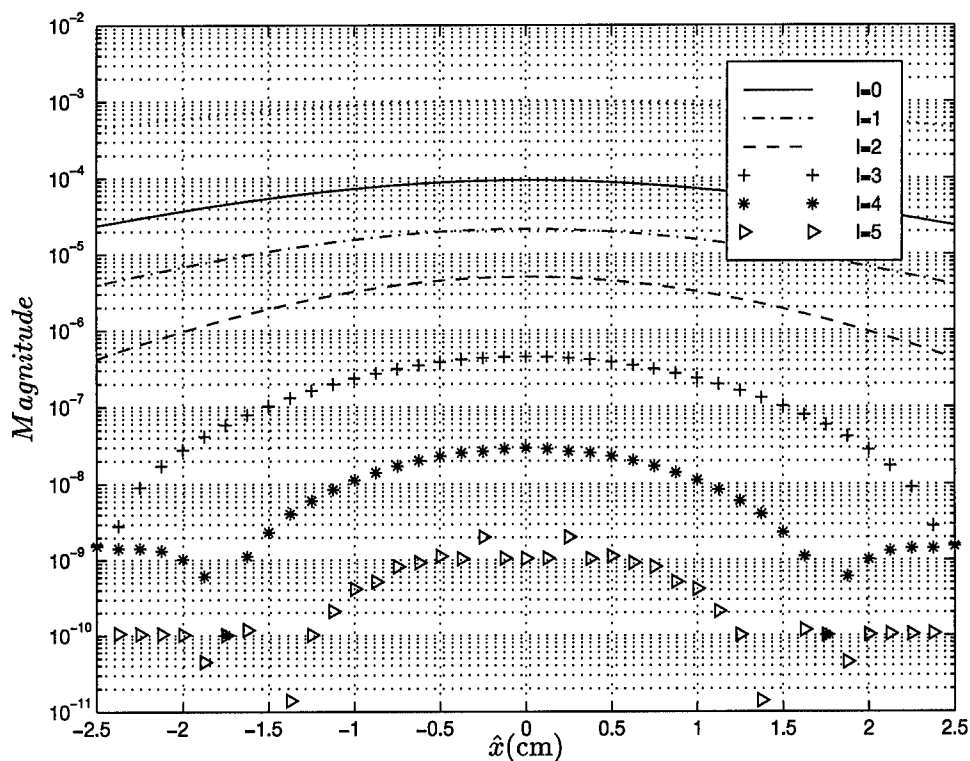


Figure 4.2 The magnitude of the incident wave due to a point source is plotted at the top of the graph. The magnitude of the first six moments ( $l$ ) in the scattered wave are plotted below the incident wave which gives better than  $10^{-6}$  value of precision in the total wave. The optical parameters used here are  $\mu_{a,out} = 0.05 \text{ cm}^{-1}$ ,  $\mu'_{s,out} = 10 \text{ cm}^{-1}$ ,  $\mu_{a,in} = 0.15 \text{ cm}^{-1}$ ,  $\mu'_{s,in} = 15 \text{ cm}^{-1}$ .

To determine the number of terms, or moments, needed, the first six terms of the scattered wave are plotted for a 1 cm diameter spherical inhomogeneity with an absorption coefficient,  $\mu_a$ , of  $0.15 \text{ cm}^{-1}$ , and a reduced scattering coefficient,  $\mu'_s$ , of  $15 \text{ cm}^{-1}$  surrounded by a background tissue with  $\mu_a = 0.10 \text{ cm}^{-1}$  and  $\mu'_s = 10 \text{ cm}^{-1}$ . For this example,  $|k_{in}a| = 1.2995$  and  $|k_{out}a| = 0.6413$ . These values indicate that more than three moments are needed in the series for acceptable accuracy. Figure 4.2 shows that to gain a precision of  $10^{-6}$ , at least the first six terms in the infinite series in Equation (2.11) must be included.

**4.3.2 Sampling Around Singularities.** Since the homogeneous wave is undefined at the location of the point source, the sampling in the spatial domain does not contain the point source location. The scattered wave described by Equation (2.11) is only valid outside

or on the boundary of the inhomogeneity, so the coordinates inside the inhomogeneity are not included in the sampling set. Sampling arbitrarily close to those locations is valid and is useful in determining the behaviors of the waves without causing numerical errors dealing with the singularities. Note that Boas's exact code is valid for both inside and outside the inhomogeneity, but it has the singularity at the point source location [49].

#### 4.4 Correlation Methodology

The mean-square error methodology is used to correlate waves calculated by different codes. The error is calculated by first finding the difference in the magnitude (or phase) of each respective sampled pixel in the wave calculated by the theoretical code and the corresponding pixel in the wave calculated by the approximated code. The difference is squared and divided by the total number of pixels. The error,  $\sigma^2$ , is mathematically expressed as,

$$\sigma^2 = \sum_{i=1}^N \sum_{j=1}^M \frac{(U_{i,j}^t - U_{i,j}^e)^2}{NM}, \quad (4.1)$$

where  $U^t$  is theoretical value and  $U^e$  is the estimated value at the  $i^{th}$  and  $j^{th}$  pixel, and  $N \times M$  is the number of pixels in the wave matrix. For the analysis in this thesis, this correlation equation is used in the  $\hat{x}$ - $\hat{y}$  plane (i.e., the detection plane) which is square. So the total number of pixels is  $N^2$ .

The theoretical value will be the output of Boas's exact code [49]. Since only the first six moments were used in the MATLAB<sup>©</sup> simulations, the values are accurate on the order of  $10^{-9}$  for the magnitude and  $10^{-6}$  for the phase. Mean square errors are expected to be at best on the order of  $10^{-18}$  and  $10^{-12}$  for magnitude and phase, respectively.

#### 4.5 Implementation of Analytic Solution Method

Photon Migration Imaging (PMI) code for this exact solution has already been developed by Boas and extensively analyzed for accuracy [49]. This exact code only yields the incident and total wave as outputs. The scattered wave can be calculated by subtracting

the incident wave from the total wave as per Equation (2.8). However, at the time the analysis in this thesis was conducted, the moments that comprise the scattered wave could not be recovered. The code developed in this thesis, referred to as the analytic solution code, can decompose the scattered wave into its moments. These moments can then be analyzed individually. The total perturbed wave is calculated in this code and is correlated to Boas' code results to validate the implementation of the algorithm.

#### *4.6 Analytic Solution Simulation Code Development*

The analytic solution in Equation (2.11) is implemented in MATLAB 5.0<sup>©</sup> to take advantage of the multi-dimensional matrix capabilities of the language. The source code for the algorithm is listed in Appendix B. This algorithm implementation is verified against the PMI code [49].

*4.6.1 Code Structure.* The code is structured as a function so that the input parameters can be passed into the algorithm and only the output quantities are returned. The incident and scattered waves are calculated from Equation (2.7) and the first six moments of Equation (2.11). The total perturbed wave is simply the superposition of those two waves via Equation (2.8).

*4.6.2 Input Parameters.* The user defines the following optical parameters of the system:

- **Muain** - Absorption coefficient inside the inhomogeneity ( $\text{cm}^{-1}$ ).
- **Musin** - Reduced scattering coefficient inside the inhomogeneity ( $\text{cm}^{-1}$ ).
- **Muaout** - Absorption coefficient of the background medium ( $\text{cm}^{-1}$ ).
- **Musout** - Reduced scattering coefficient of the background medium ( $\text{cm}^{-1}$ ).
- **f** - Modulation frequency (Hz).
- **idim** - Length of x- and y-axes (cm).
- **inc** - Increments (cm) along x- and y-axes.
- **zinc** - Increments (cm) along z-axis.

- **zdet** - Location of detector plane (cm).
- **Nin** - Index of refraction of the inhomogeneity.
- **Nout** - Index of refraction of the background medium.

The following parameter variables are passed into the analytic solution algorithm:

- **numdeg** - Truncate series after this number of terms.
- **Sac** - Source modulation amplitude.
- **a** - Radius of the inhomogeneity (cm).
- **rsx, rsy, rsz** - Location of the source along x-, y-, and z-axes (cm).
- **x, y, z** - Vectors containing sampling points along x-, y-, and z-axes (cm).
- **Dout** - Diffusion coefficient of the background medium.
- **Vout** - Speed of light in the background medium.
- **Kout** - Wavenumber in the background medium.
- **Din** - Diffusion coefficient of the inhomogeneity.
- **Kin** - Wavenumber of the inhomogeneity.

The variables in bold are defined by the user, while the plain-text ones are calculated from the user-defined values. An example of this listing is in Appendix A.

*4.6.3 Output Quantities.* The outputs of the program are the incident homogeneous wave and the scattered wave due to the inhomogeneity at each incremental point along all axes. The total wave is also an output quantity and is simply the superposition of the first two quantities. In the code, these are identified by the variables: **Uinc**, **Us**, and **Uout**, respectively.

*4.6.4 Validation of Simulation.* To verify the validity of the code developed here, each wave of this code at the detection plane is correlated to the corresponding wave in the exact solution code [49] by calculating the mean-square error between the two via Equation (4.1). The system is modeled as illustrated in Figure 4.1 at 20 MHz

with a spherical inhomogeneity with a 1 cm diameter. The background medium has  $\mu_a = 0.05 \text{ cm}^{-1}$ ,  $\mu'_s = 10 \text{ cm}^{-1}$ , while the inhomogeneity has the properties  $\mu_a = 0.15 \text{ cm}^{-1}$ ,  $\mu'_s = 15 \text{ cm}^{-1}$ .

The PMI code uses an approximated diffusion coefficient,  $D = v/(3\mu'_s)$  while the analytic solution code used the exact definition of the diffusion coefficient, e.g.  $D = v/[3(\mu_a + \mu'_s)]$ . In addition, the PMI code does not include the  $v/D_{out}$  factor in the  $A_{l,m}$  coefficients in Equation (2.10). To correlate the two codes, these corrections were made to the analytic solution code.

With the amendments to the analytic solution code to match the algorithm implemented in the PMI code, the magnitude and the phase of the incident waves have mean-square errors,  $\sigma^2 = 7.8695 \cdot 10^{-17}$  and  $\sigma^2 = 6.6781 \cdot 10^{-8}$ , respectively. The scattered and total waves are correlated in the same manner. The magnitude and the phase of the scattered waves have mean-square errors,  $\sigma^2 = 2.9876 \cdot 10^{-9}$  and  $\sigma^2 = 6.5293 \cdot 10^{-8}$ , respectively. A relative percentage error for each respective point of the incident and scattered waves in the detector plane are depicted in Figures 4.3 and 4.4 to show that the resulting error is evenly distributed over the plane indicating that differences are due to computer numerical round-off. However, the majority of the error in Figure 4.4(a) is due to the truncation of the infinite series after six terms. The PMI code truncates the series after more than 20 terms, so the correlation error is consistent with this reason.

The total output wave of the analytic solution code is only used to validate this algorithm against Boas's results. With the exceptions noted before, the algorithm is a good match. The magnitude and phase of the total output waves have mean-square errors of  $\sigma^2 = 2.6027 \cdot 10^{-9}$  and  $\sigma^2 = 1.0473 \cdot 10^{-6}$ . Similar to the incident and scattered waves, the error is caused by computer round-off and series truncation. The relative percentage error for each respective  $x$  and  $y$  coordinate in the detector plane is illustrated in Figure 4.5. The numerical round-off error is proportional to  $1/\bar{r}$ , so the error is greater nearer the center of plane and decreases as the  $(x, y)$  values in the plane increase. The mean-square errors are summarized in Table 4.1. These small mean-square error values give validity to the incident and scattered wave calculations, as well as the total wave, at the detection plane.

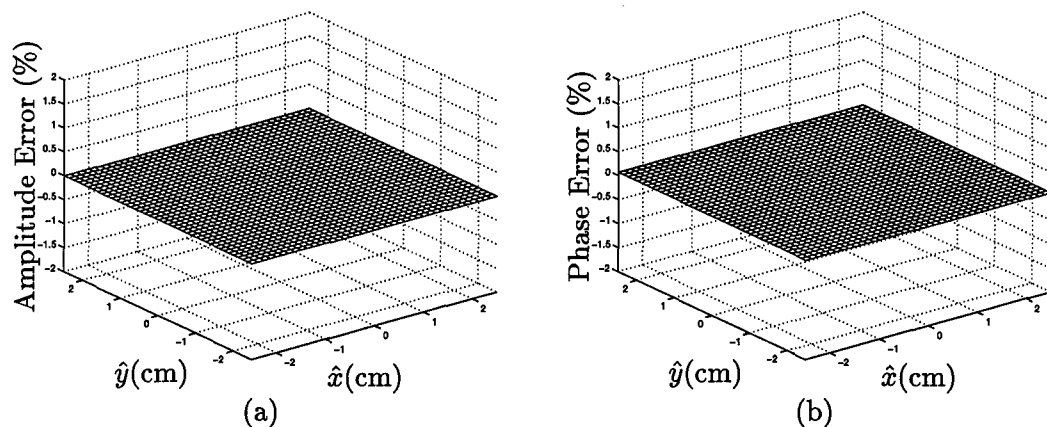


Figure 4.3 The percent error in the detector plane is plotted for the (a) magnitude and (b) phase of the incident waves caused by a point source incident wave. For both figures,  $\mu_{a,out} = 0.05 \text{ cm}^{-1}$ ,  $\mu'_{s,out} = 10 \text{ cm}^{-1}$ ,  $\mu_{a,in} = 0.15 \text{ cm}^{-1}$ ,  $\mu'_{s,in} = 15 \text{ cm}^{-1}$ .

#### 4.7 Implementation of Analytic Transfer Function Method

The total wave can also be calculated in the spatial frequency domain as determined in Section 3.2. This code calculates the incident homogeneous wave as well as the scattered wave due to the inhomogeneity exactly as executed in the analytic solution code. With these two wave quantities, the transfer function can be calculated and used to generate the total output wave. In essence, this code validates the existence of a transfer function through the correlation of the total wave generated in both the spatial and the spatial frequency domains. In Chapter V, the output wave in this analytic transfer function code is used to analyze the Fourier optics wave propagation model, and the behavior due to various optical parameters is investigated .

#### 4.8 Analytic Transfer Function Simulation Code Development

The analytic transfer function solution in Equation (3.2) is also implemented in MATLAB 5.0<sup>©</sup> for its multi-dimensional matrix capabilities. The source code for the algorithm is listed in Appendix C. This algorithm implementation is verified against PMI, a known working code [49].

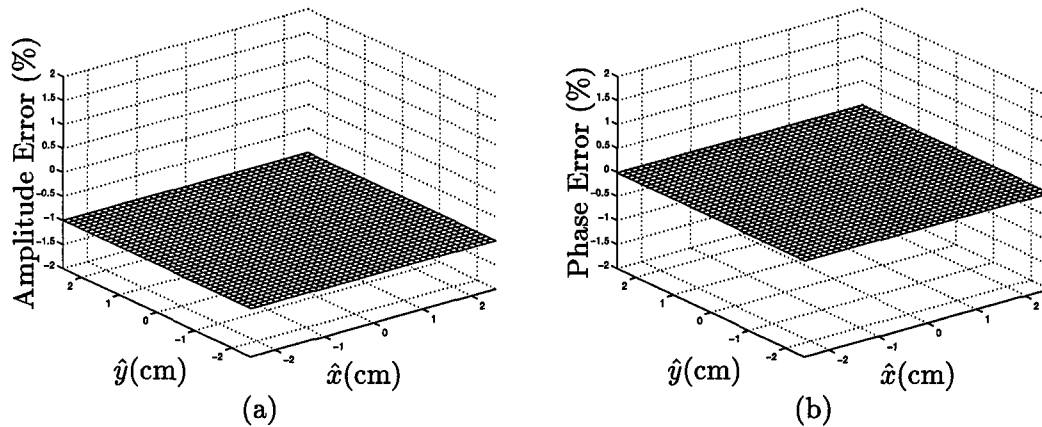


Figure 4.4 The percent error in the detector plane is plotted for the (a) magnitude and (b) phase of the scattered waves from a spherical inhomogeneity with a 1 cm diameter. For both figures,  $\mu_{a,out} = 0.05 \text{ cm}^{-1}$ ,  $\mu'_{s,out} = 10 \text{ cm}^{-1}$ ,  $\mu_{a,in} = 0.15 \text{ cm}^{-1}$ ,  $\mu'_{s,in} = 15 \text{ cm}^{-1}$ . The error is mainly due to the truncation of the infinite series.

**4.8.1 Code Structure.** This analytic transfer function code is structured so that input parameters can be passed into the algorithm and only the output quantities are returned. The algorithm determines the incident homogeneous and the scattered waves in the spatial domain and then converts the two quantities to the spatial frequency domain. The transfer function is determined via Equation (3.2) and is used to construct the total perturbed wave. The total wave is then transformed back into the spatial domain where it is then correlated with the total wave generated directly in the spatial domain from the PMI code [49]. The implementation of the analytic transfer function solution is illustrated in Figure 4.6.

**4.8.2 Discretization Effects.** Zero-padding of the wave matrices avoids wrap-around error in the Fourier transform calculations. The zero-pad matrix size is selected to be a square matrix of a power of 2 in order to take advantage of the FFT algorithms.

**4.8.3 Input Parameters.** The user-defined parameters and input variables are the same as listed in Section 4.6.2. An example of this listing is in Appendix A.

**4.8.4 Output Quantities.** The outputs of the program are the incident homogeneous wave and the scattered wave due to the inhomogeneity at each incremental point

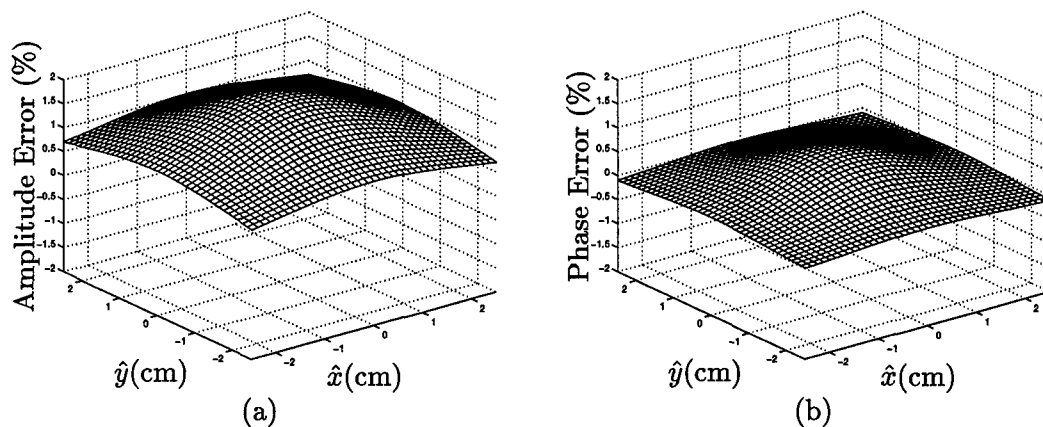


Figure 4.5 The percent error in the detector plane is plotted for the (a) magnitude and (b) phase of the total perturbed wave from a spherical inhomogeneity with a 1 cm diameter. For both figures,  $\mu_{a,out} = 0.05 \text{ cm}^{-1}$ ,  $\mu'_{s,out} = 10 \text{ cm}^{-1}$ ,  $\mu_{a,in} = 0.15 \text{ cm}^{-1}$ ,  $\mu'_{s,in} = 15 \text{ cm}^{-1}$ .

along all axes. The transfer function that is calculated from those two waves and the resulting total perturbed wave are also outputs to this code. All of these quantities are identified by the variables: Uinc, Uscatt, H, and UoutH, respectively.

**4.8.5 Validation of Simulation.** To verify the validity of the code developed, the total perturbed wave calculated in the detection plane must be transformed into the spatial domain, then correlated to the wave calculated in the exact solution code by Boas [49]. The correction factors discussed in Section 4.6.4 are applied in order to correlate to the same algorithm. Namely, the approximated diffusion coefficient,  $D = v/(3\mu'_s)$ , is used, and the  $v/D_{out}$  factor in the  $A_{l,m}$  coefficients is removed from the code to match the PMI algorithm. The analysis in Chapter V using the transfer function calculated here does not include the  $v/D_{out}$  factor, but does use the exact diffusion coefficient,  $D = v/(3[\mu_a + \mu'_s])$ .

The perturbed wave is calculated from a 1 cm diameter spherical inhomogeneity, situated in a homogeneous medium as in Figure 4.1 at 20 MHz. The background medium has  $\mu_a = 0.05 \text{ cm}^{-1}$ ,  $\mu'_s = 10 \text{ cm}^{-1}$ , while the inhomogeneity has the properties  $\mu_a = 0.15 \text{ cm}^{-1}$ ,  $\mu'_s = 15 \text{ cm}^{-1}$  (the same as the previous validation).

The magnitude and phase of the total output waves have mean-square errors of  $\sigma^2 = 2.6027 \cdot 10^{-9}$  and  $\sigma^2 = 1.0473 \cdot 10^{-6}$ . The mean-square errors match the direct

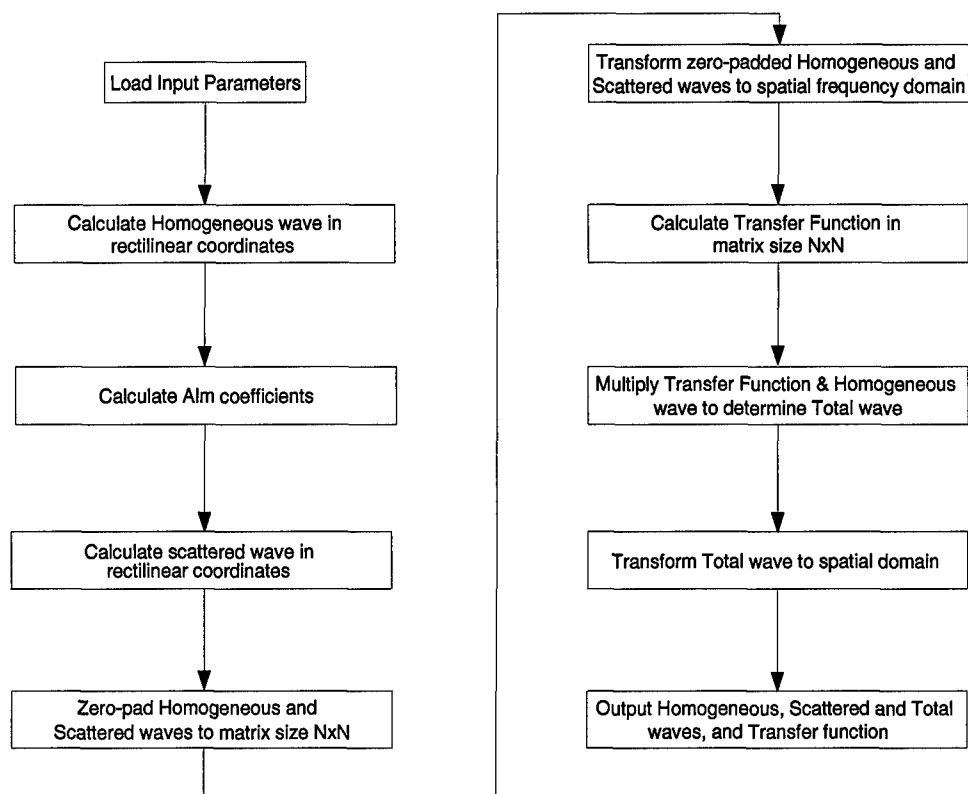


Figure 4.6 The flow chart above shows the code structure for simulating the analytic transfer function method in MATLAB 5.0<sup>©</sup>.

evaluation of the total wave in the analytic solution code (Section 4.6.4), indicating that the Fourier transform algorithm of MATLAB 5.0<sup>©</sup> does not introduce additional error into the program. The relative percentage error for each respective  $x$  and  $y$  coordinate in the detector plane is illustrated in Figure 4.7. The incident and scattered waves were correlated in Section 4.6.4. The mean-square errors are summarized in Table 4.1. These high correlation values give validity to the existence of the transfer function since there is a good match to the total perturbed wave.

#### 4.9 Implementation of the Fourier Optics Model

In Section 2.5, a solution was discussed for wave propagation in a source-free homogeneous medium using Fourier optics. Since the system under investigation contains a spherical inhomogeneity in a otherwise piece-wise homogeneous medium, the solution can only be applied in the regions that do not contain the inhomogeneity. This code calculates

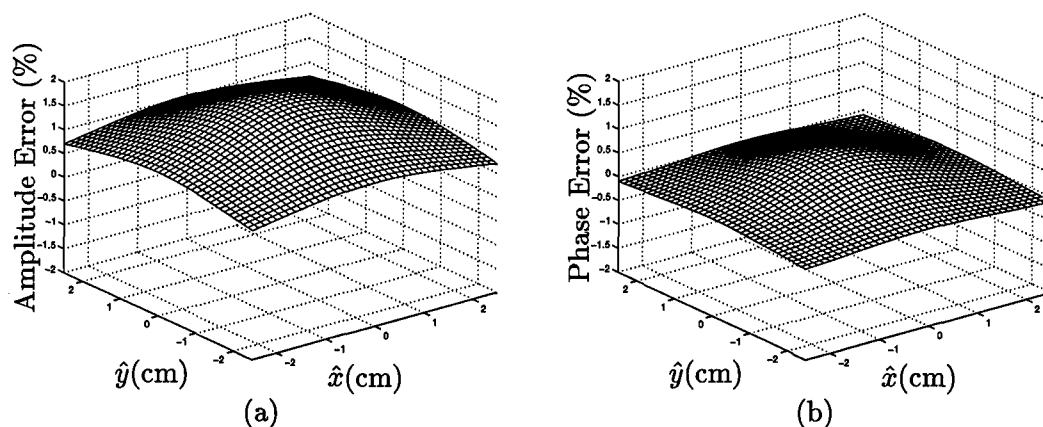


Figure 4.7 The percent error in the detector plane is plotted for the (a) magnitude and (b) phase of the total perturbed wave from the analytic transfer method, from a 1 cm diameter spherical inhomogeneity. For both figures,  $\mu_{a,out} = 0.05 \text{ cm}^{-1}$ ,  $\mu'_{s,out} = 10 \text{ cm}^{-1}$ ,  $\mu_{a,in} = 0.15 \text{ cm}^{-1}$ ,  $\mu'_{s,in} = 15 \text{ cm}^{-1}$ .

Wave	Analytic Magnitude	Analytic Phase	Analytic Transfer Magnitude	Analytic Transfer Phase
Homogeneous	$7.8695 \cdot 10^{-17}$	$6.6781 \cdot 10^{-8}$	$7.8695 \cdot 10^{-17}$	$6.6781 \cdot 10^{-8}$
Scattered	$2.9876 \cdot 10^{-9}$	$6.5293 \cdot 10^{-8}$	$2.9876 \cdot 10^{-9}$	$6.5293 \cdot 10^{-8}$
Total	$2.6027 \cdot 10^{-9}$	$1.0473 \cdot 10^{-6}$	$2.6027 \cdot 10^{-9}$	$1.0473 \cdot 10^{-6}$

Table 4.1 The mean-square error of the simulated waves calculated using both the analytic and the analytic transfer methods. Both methods are compared to the exact solution developed by Boas [49]. Note that the FFT algorithm used in the analytic transfer method does not introduce additional error into the calculation.

an incident wave and propagates it through the homogeneous medium up to the plane containing center of the inhomogeneity. At that point, the spherical object is modeled as a thin lens with a corresponding transmittance function in the plane containing its center (Section 2.5.2). The wave is then transmitted through that plane by multiplying the incident wave by the transmittance function in Equation (2.24). This distorted wave is then propagated to the detector plane using Goodman's method in Equation (2.22) [41]. The regions of validity for this model are investigated in Chapter V.

**4.9.1 Code Structure.** Similar to the previous two model implementations, this method is written in MATLAB 5.0<sup>©</sup>. The function structure enables the user to pass

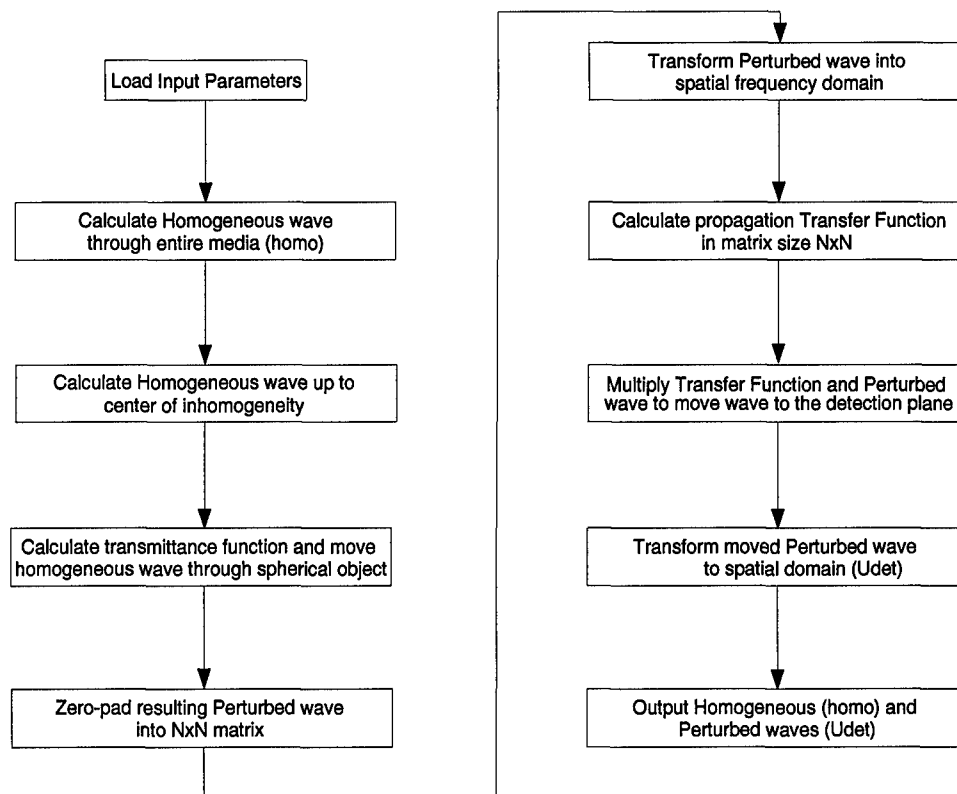


Figure 4.8 The flow chart above shows the code structure for simulating the Fourier optics model in MATLAB 5.0<sup>©</sup> [41].

parameters into the algorithm and returns only the desired output quantities. The source code for the algorithm is listed in Appendix D, and a flow chart illustrates the implementation of the Fourier optics method in Figure 4.8.

**4.9.2 Discretization Effects.** Zero-padding of the wave matrices avoids wrap-around error in the Fourier transform calculations. The zero-pad matrix size is selected to be a square matrix of a power of 2 in order to take advantage of the FFT algorithms.

**4.9.3 Input Parameters.** The user-defined parameters and input variables are the same as listed in Section 4.6.2. The variables *inc*, *idim*, and *zinc* are passed into the program in addition to those listed in Section 4.6.2. The diffusion coefficient for the inhomogeneity, *Din*, is not needed in the program. An example of this listing is in Appendix A.

*4.9.4 Output Quantities.* The output identified as the variable “homo” is the incident homogeneous wave through the homogeneous medium without any inhomogeneity present. The only other output quantity is the wave perturbed by the inhomogeneity and is specified by “Udet”.

#### 4.10 Test Plan

Only the first six moments will be included in these simulations for the reasons stated in Section 4.3. The pure absorption and pure scattering cases have been highly investigated [13]. The concentration of this thesis is for inhomogeneities that have small absorptive and highly scattering properties as well as low contrast as compared to the background medium properties. For completeness, high contrast cases (i.e. pure absorption and pure scattering) are investigated to determine trends.

Type	$\mu_a$ (cm <sup>-1</sup> )	$\mu'_s$ (cm <sup>-1</sup> )
Human Breast Tissue	0.05	10.0
Adipose Tumor	0.7	9.0
Fibroadenoma Tumor	0.5	7.0
Carcinoma Tumor	0.5	12.0

Table 4.2 These are typical optical parameters of human tissue characterized at an optical wavelength of 700 nm [12, 18].

*4.10.1 Perturbation Cases.* Typical  $\mu_a$  and  $\mu'_s$  parameters used to model human tissue and tumors are listed in Table 4.2. For this analysis, the background medium was consistently modeled as human tissue with  $\mu_a = 0.05$  cm<sup>-1</sup> and  $\mu'_s = 10$  cm<sup>-1</sup>. The frequency at which all of the simulations were conducted was 20 MHz [38]. The inhomogeneity parameters are varied according to Table 4.3. Each perturbation case includes an absorption coefficient of 100, 200, 300, or 400% of 0.05 cm<sup>-1</sup>, or rather a contrast of 0 (none), 100 (low), 200 (high), or 300% (very high) relative to the background absorption coefficient, respectively. It should be noted that these absorption contrasts are still less than actual cancerous tumor values given in Table 4.3. Similarly, the scattering parameter is 100, 110, 150, or 200% of 10 cm<sup>-1</sup>, meaning a contrast of 0 (none), 10 (low), 50 (high), or 100% (very high) relative to the background reduced scattering coefficient. A pure

absorber indicates an inhomogeneity with only an absorption contrast, while a pure scatterer is an inhomogeneity with only a scattering contrast. From the simulated results of each of the perturbation cases in the analytic transfer function code as well as the Fourier optics method code, the effects the different levels of contrast have on the magnitude and phase change in the resulting total wave are determined. All of the cases in Table 4.3 do not exceed the conditions for the  $P_1$  approximation of the linear transport equation, e.g.  $\mu_a \ll \mu'_s$  and  $\mu_s/[\mu_s + \mu_a] \approx 1$ .

Perturbation Case	Absorption Contrast	Scattering Contrast	$\mu_{a,in}$ (cm <sup>-1</sup> )	$\mu'_{s,in}$ (cm <sup>-1</sup> )
Base Line	none	none	0.05	10
Pure Absorption	high	none	0.10	10
Pure Absorption	high	none	0.15	10
Pure Absorption	very high	none	0.20	10
Pure Scatterer	none	high	0.05	11
Pure Scatterer	none	high	0.05	15
Pure Scatterer	none	very high	0.05	20
Mixed	low	low	0.10	11
Mixed	low	high	0.10	15
Mixed	low	very high	0.10	20
Mixed	high	low	0.15	11
Mixed	high	high	0.15	15
Mixed	high	very high	0.15	20
Mixed	very high	low	0.20	11
Mixed	very high	high	0.20	15
Mixed	very high	very high	0.20	20

Table 4.3 The wave behavior is analyzed for highly scattering optical parameters, as well as for levels of contrast between the background tissue (designated by the subscript "out") and the inhomogeneity (designated by the subscript "in"). All of these values are for a homogeneous background medium with  $\mu_{a,out} = 0.05 \text{ cm}^{-1}$  and  $\mu'_{s,out} = 10 \text{ cm}^{-1}$ .

**4.10.2 Analysis Plan.** The behavior of a weakly perturbative system is analyzed in several ways using the cases listed in Table 4.3. In addition, the extent of error in the Fourier optics approximation is also studied under this system.

**4.10.2.1 Sensitivity Analysis.** For the low, high, and mixed contrast cases, the total wave behavior relative to the contrast in the optical characteristics is investigated.

The moment analysis in Chapter III determined that an absorptive contrast results in an amplitude change, while a scattering contrast causes perturbation in the phase. The sensitivity analysis will show to what extent varying degrees of contrast perturb the output wave amplitude and phase. For a unit amplitude, zero phase incident wave, the transfer function in Equation (3.26) can be used to examine this sensitivity of the system.

*4.10.2.2 Size of Inhomogeneity.* A weakly perturbative case is used to determine the effects low contrast in absorption and scattering have on detecting various sizes of the inhomogeneity. Again, the transfer function calculated from the analytic transfer function model can be used in this analysis.

*4.10.2.3 Moment Contribution.* For each perturbative case, the moments of the scattered wave are investigated to determine the amount of contribution each moment has to the total wave relative to the amount of absorptive and/or scattering contrast present in the system.

*4.10.2.4 Validity of Fourier Optics Approximation.* The total output wave calculated from the analytic transfer function model is compared to Goodman's Fourier optics method. Since the Fourier optics approach is a straight ray approximation to distortion caused by a spherical inhomogeneity, the relative error in the two models, specifically in the model of the inhomogeneity, will determine the regions of validity of this approach.

#### *4.11 Summary*

Three different models of wave propagation through a homogeneous medium containing a spherical object were simulated in this chapter. The first is an implementation of the analytic solution (derived by Boas) to the problem. The second is a Fourier optics approach that applies an exact formulation of a transfer function to propagate the wave from the source to the detector. The last is a plane wave representation of the incident spherical wave developed by Goodman and uses a simpler transfer function to propagate the perturbed wave from the inhomogeneity to the detector.

The first two models were correlated against a known working code, PMI. With the exception of a complex scale factor and an approximated parameter, the models are in good agreement with PMI. Goodman's wave propagation model is examined in Chapter V for validity.

The plan for analysis of the analytic transfer function was outlined for a range of weak to strong perturbative cases in Table 4.3. The surrounding background medium is modeled as human breast tissue with a fixed set of optical parameters. By varying the optical properties of the inhomogeneity, contrasts between the properties in the object and the surrounding medium create the weak and strong perturbative conditions. In addition to varying the optical properties, changing the size of the inhomogeneity will be examined. By measuring the amount of perturbation caused by the contrast in the optical properties or by the size of the object, the ability to detect the inhomogeneity can be determined. The amount of contrast present in the system also affects which moments significantly contribute to the perturbation in the output wave. By determining which moments dominate in each perturbation case, an improved approximation can be made to the transfer function expression developed in Chapter III.

## *V. Simulation Results and Analysis*

### *5.1 Introduction*

Tumors are detectable because their optical scattering and absorption properties are different than that of the media in which they are embedded. This contrast in optical properties causes a perturbation in the diffuse photon density wave (DPDW). If the level of change in the DPDW is greater than a certain limit, the tumor is considered detectable. An understanding of the interaction and the levels of contrasts needed to detect and localize the object is important optical imaging, particularly in medical applications.

General behavior of the total wave for different absorptive and scattering properties of the inhomogeneity relative to a constant background medium are considered in this evaluation. The particular environment of interest in this thesis is a weak perturbation, meaning, the optical characteristics of the inhomogeneity slightly differ from the background medium. Since the transfer function developed in Chapter III completely characterizes the perturbations caused by the inhomogeneity, the perturbative behavior can be determined by examining the transfer function in the spatial domain. The contribution of the individual moments in the scattered wave are also studied to determine the necessary number of moments needed to best approximate the scattered wave. This chapter concludes with a comparison between the analytic transfer function and the Fourier optics model in Section 2.5 to determine the regions of validity as well as the relative accuracy of the transmittance function in Goodman's method.

### *5.2 Sensitivity to Contrasts in Optical Parameters*

Perturbations caused by the presence of an inhomogeneity are caused by a difference, or contrast, in the optical parameters inside and outside the object. The amount of distortion by the contrast defines the sensitivity of the system. By measuring the levels of distortion, inhomogeneities can be detected. The measurement precision necessary to detect optical inhomogeneities can be estimated using the analytic transform solution method. The required amplitude precision is determined by the ratio of the magnitudes of the total wave to the homogeneous wave. The difference in the phase between the total

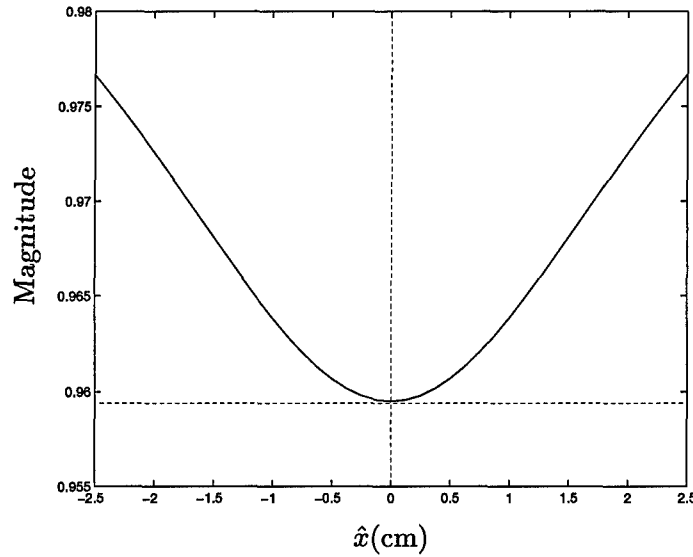


Figure 5.1 The transfer function in the spatial domain is plotted for an inhomogeneity with  $\mu'_s = 15 \text{ cm}^{-1}$  and  $\mu_a = 0.15 \text{ cm}^{-1}$  embedded in a medium with the  $\mu'_s = 10 \text{ cm}^{-1}$  and  $\mu_a = 0.05 \text{ cm}^{-1}$ . This shows that the best estimate for measurement precision can be determined here at the  $x = 0$  position for  $y = 0 \text{ cm}$  and the detector plane located at  $z = 3 \text{ cm}$ .

and the homogeneous wave is the necessary phase precision. If the homogeneous wave has unit amplitude and zero phase, the magnitude and phase precision required is simply the magnitude and phase of the transfer function from Equation (3.26) in the spatial domain.

*5.2.1 System Configuration.* To study the system sensitivity, the system is configured as in Section 4.2. Figure 5.1 illustrates that for an inhomogeneity with a reduced scattering coefficient,  $\mu'_s = 15 \text{ cm}^{-1}$ , and an absorption coefficient,  $\mu_a = 0.15 \text{ cm}^{-1}$ , embedded in a medium with  $\mu'_s = 10 \text{ cm}^{-1}$  and  $\mu_a = 0.05 \text{ cm}^{-1}$ , the maximum perturbation in the DPDW occurs at the  $x = 0$  position. Since the system is symmetric, the same view holds for the  $\hat{y}$  direction. The locations along the  $\hat{x}$  and  $\hat{y}$  axes indicate that the maximum perturbation occurs along the axis that contains the source, the inhomogeneity and the detector. Along that axis, then, the best estimate for measurement precision can be determined.

For the perturbation cases listed in Table 4.3, the precision in the magnitudes and phases are determined and compared to what most detectors can detect, which is at least

a 0.1% amplitude and  $0.1^\circ$  phase change [10]. If the perturbation caused by the inhomogeneity is greater than the detector level, the object is considered detectable. It should be noted that noise is not added to the signal and that detection ultimately depends on the level of noise in the system [13]. For this reason, the amplitude detection level considered in this analysis will be increased to 1.0%. For all the contrast cases, the system is configured as in Section 4.2 at a frequency of 20 MHz. The spherical inhomogeneity is embedded in a background medium with  $\mu'_s = 10 \text{ cm}^{-1}$  and  $\mu_a = 0.05 \text{ cm}^{-1}$ , and the optical parameters of the inhomogeneity are varied.

In addition to being able to detect the inhomogeneity, the minimum in either the magnitude or the phase of the transfer function in the spatial domain can be used to determine the depth of the object.

*5.2.2 Absorption Contrast With a Pure Absorber.* A pure absorber with  $\mu'_s = 10 \text{ cm}^{-1}$  is studied in this analysis. The absorption coefficient for the absorber is varied to show the perturbation effects on the DPDW.

In Figure 5.2, a slice along the  $(x, y) = (0, 0)$  is shown for the magnitude and phase of the homogeneous wave through the media, the scattered wave caused by the absorber, and the total wave in the system. It is along this central axis that the maximum perturbation will occur as discussed in Section 5.2.1.

The plot in Figure 5.3 indicates for a pure absorber at a detector plane 3 cm from the center of the inhomogeneity, as small as 4% amplitude precision is necessary to detect an inhomogeneity with 100% absorption contrast. There is no detectable phase difference at that distance. Note that the straight solid line indicates the detection level, but the discontinuous solid line is for an inhomogeneity with no contrast in either scattering or absorption, and consequently no noticeable change in phase or magnitude. As the value of the absorption coefficient increases for the inhomogeneity relative to the background medium, the precision required is less stringent. For example, at three times the amount of absorption contrast, only 8% amplitude precision is needed.

If the detector plane moves closer to the inhomogeneity, the relative amount increase in both magnitude and phase are evident. However, even at the boundary of the inhomogeneity,

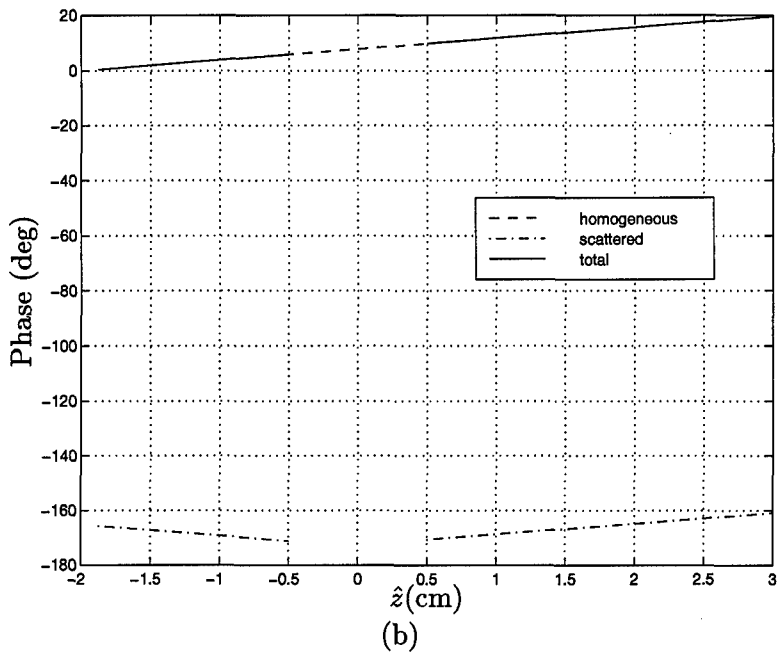
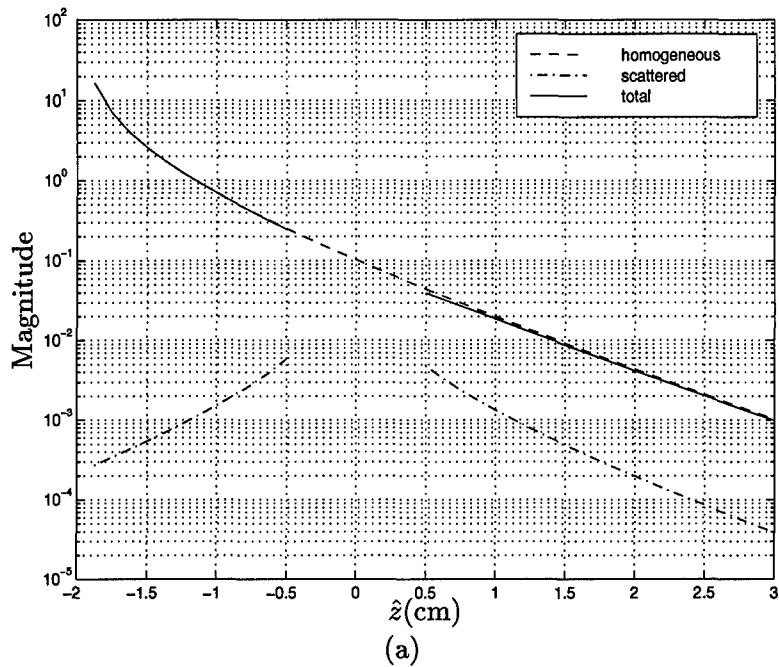


Figure 5.2 A view along the  $(x, y) = (0, 0)$  axis through the medium is shown for a pure absorber with an absorption coefficient,  $\mu_a = 0.15 \text{ cm}^{-1}$ . The (a) magnitude and (b) phase of the waves shown are the homogeneous (dashed line), the scattered wave due to the inhomogeneity (dashed-dotted line), and the total wave (solid line). It is along this axis that the maximum perturbation will occur.

geneity, the phase is only  $0.08^\circ$  and does not meet the minimum detection level for most detectors.

*5.2.3 Scattering Contrast With a Pure Scatterer.* In this case, a pure scatterer with  $\mu_a = 0.05 \text{ cm}^{-1}$  is investigated. To show the perturbation effects on the DPDW, the reduced scattering coefficient for the object is varied from no scattering contrast up to twice the value of the background medium.

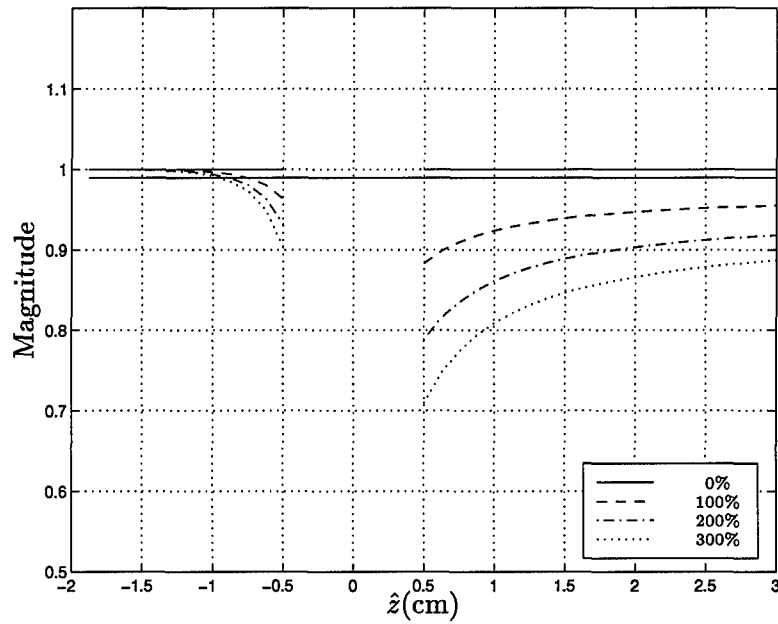
In Figure 5.4, a slice along the  $(x, y) = (0, 0)$  is shown for the magnitude and phase of the homogeneous wave through the medium, the scattered wave caused by the scatterer, and the total wave in the system. As discussed in Section 5.2.1, the maximum perturbation will occur along this axis.

The plot in Figure 5.5 shows that at the detector plane, 3% amplitude and  $0.03^\circ$  phase precision are necessary to detect the inhomogeneity at a 3 cm distance from the object center, with a 10% scattering contrast present. The phase amount is not sufficient to meet most detector minimum levels. If the detector plane is located close to the right boundary of the inhomogeneity, the phase perturbation increases to  $0.1^\circ$ . The maximum magnitude and phase in all variations of the absorption contrast occur at the right (positive  $\hat{z}$ ) boundary of the inhomogeneity.

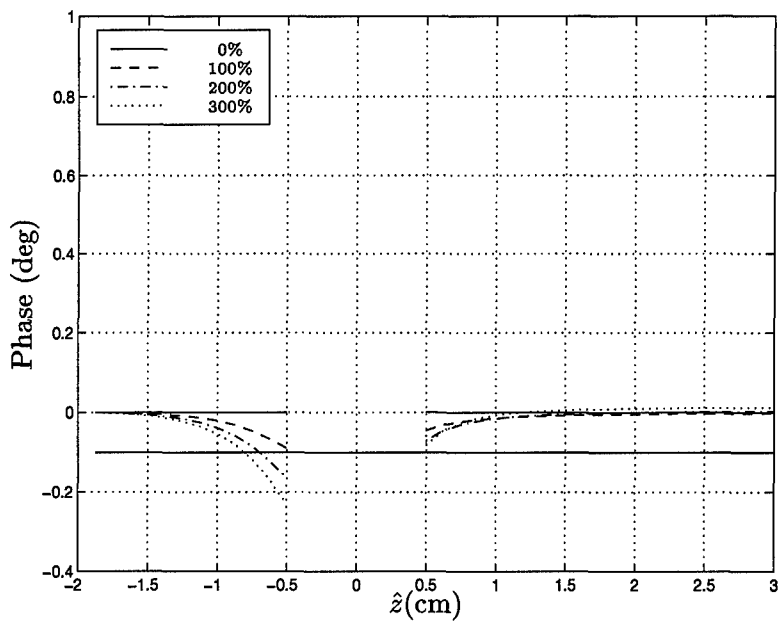
As the scattering contrast increases for the inhomogeneity relative to the background medium, the perturbation in both the magnitude and phase increases. At a scattering contrast of 1.5 times the background scattering value, the phase is  $0.15^\circ$  at the detector plane 3 cm from the center of the inhomogeneity and meets the lower detector limits. Note that the straight solid line indicates the detection level, but the discontinuous solid line in Figure 5.5 is for an inhomogeneity with no contrast in either scattering or absorption, and consequently no noticeable phase or magnitude.

The results from Sections 5.2.2 and 5.2.3 are consistent with results presented in the literature for purely absorptive and purely scattering inhomogeneities [12, 13].

*5.2.4 Low Contrast in Absorption and Varied Contrast in Scattering Coefficients.* In this case, an inhomogeneity with a 100% absorption contrast, or  $\mu_{a,in} = 0.10 \text{ cm}^{-1}$ , is

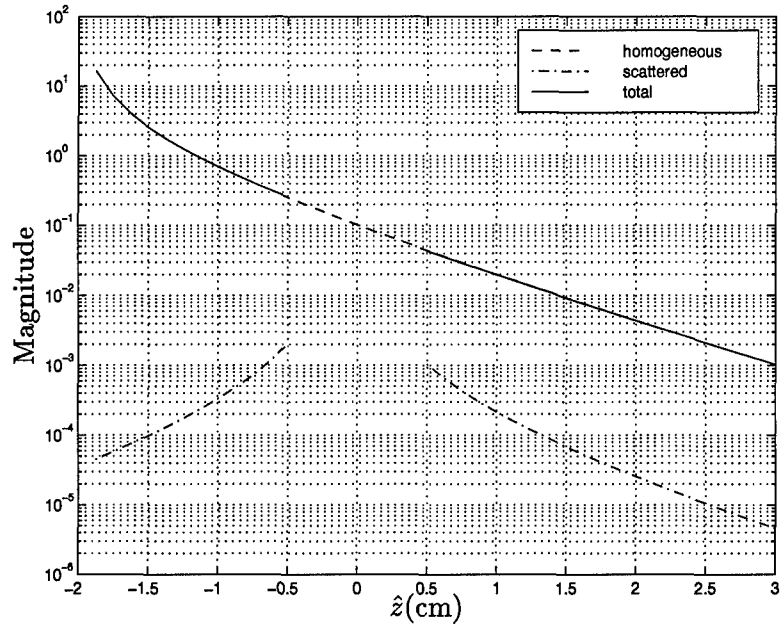


(a)

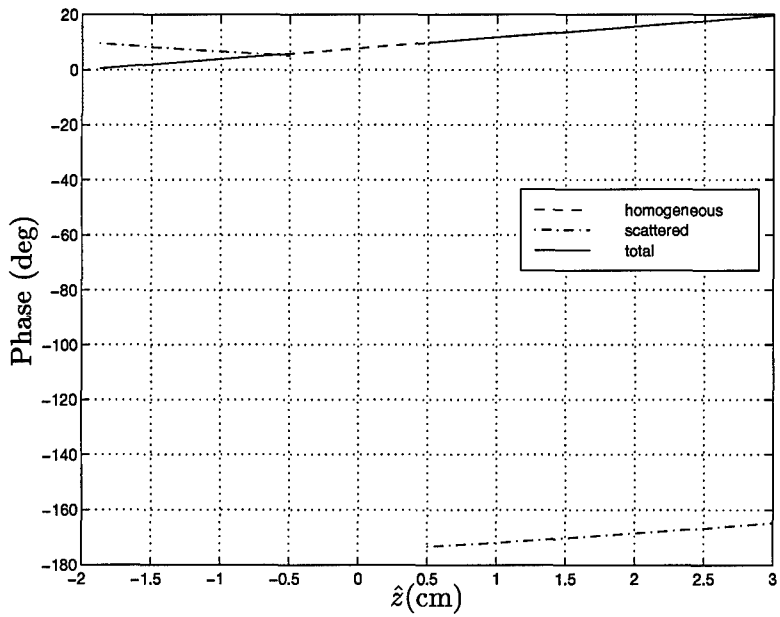


(b)

Figure 5.3 These plots show the (a) magnitude and (b) phase (degrees) of the analytic transfer function in the spatial domain for a pure absorber along the  $\hat{z}$ -axis. The object absorption coefficient is varied as:  $\mu_{a,in} = 0.05 \text{ cm}^{-1}$  (solid line),  $\mu_{a,in} = 0.10 \text{ cm}^{-1}$  (dashed line),  $\mu_{a,in} = 0.15 \text{ cm}^{-1}$  (dashed-dotted line), and  $\mu_{a,in} = 0.20 \text{ cm}^{-1}$  (dotted line). For both figures,  $\mu'_{s,in} = 10 \text{ cm}^{-1}$ ,  $\mu_{a,out} = 0.05 \text{ cm}^{-1}$ , and  $\mu'_{s,out} = 10 \text{ cm}^{-1}$ . The straight solid line in each graph indicates the minimum detection level.



(a)



(b)

Figure 5.4 A view along the  $(x, y) = (0, 0)$  axis through the medium is shown for a pure scatterer with reduced scattering coefficient,  $\mu'_s = 15 \text{ cm}^{-1}$ . The waves shown are the homogeneous (dashed line), the scattered wave due to the inhomogeneity (dashed-dotted line), and the total wave (solid line). It is along this axis that the maximum perturbation will occur.

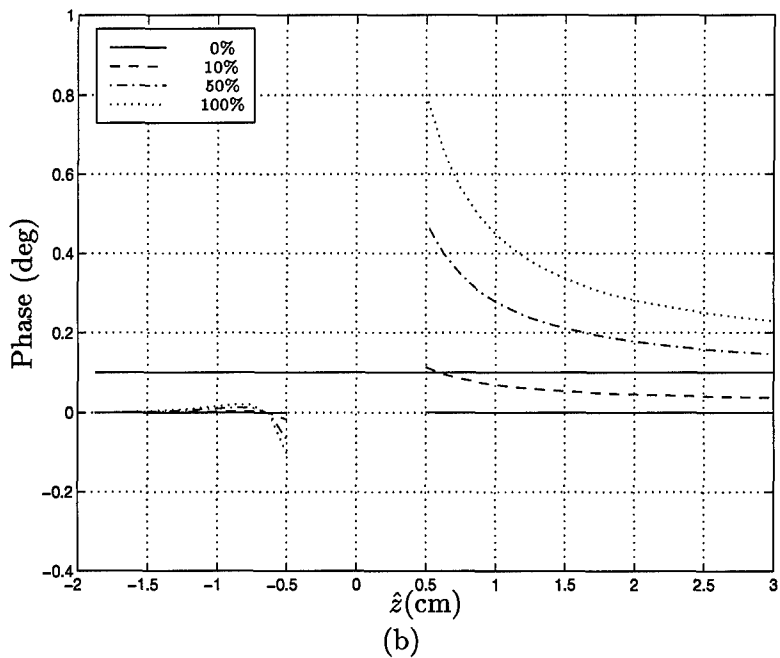
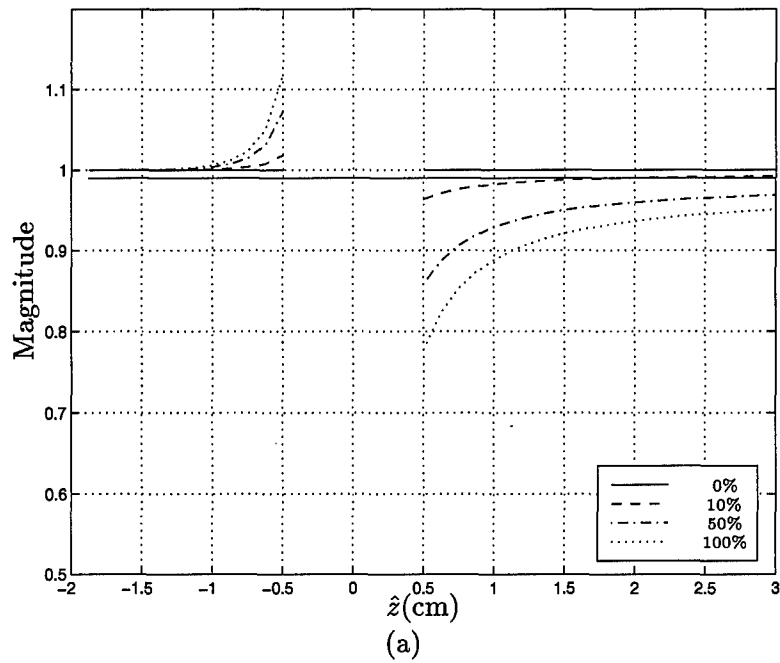


Figure 5.5 These plots show the (a) magnitude and (b) phase (degrees) of the analytic transfer function in the spatial domain for a pure scatterer along the  $\hat{z}$ -axis. The object scattering coefficient is varied as:  $\mu'_{s,in} = 10 \text{ cm}^{-1}$  (solid line),  $\mu'_{s,in} = 11 \text{ cm}^{-1}$  (dashed line),  $\mu'_{s,in} = 15 \text{ cm}^{-1}$  (dashed-dotted line), and  $\mu'_{s,in} = 20 \text{ cm}^{-1}$  (dotted line). For both figures,  $\mu_{a,in} = 0.05 \text{ cm}^{-1}$ ,  $\mu_{a,out} = 0.05 \text{ cm}^{-1}$ , and  $\mu'_{s,out} = 10 \text{ cm}^{-1}$ . The straight solid line in each graph indicates the minimum detection level.

studied. The reduced scattering coefficient for the object is varied to examine the resulting perturbations for this low absorption contrast. Figure 5.6 indicates that for a 10% difference in scattering coefficients, 4% amplitude and  $0.04^\circ$  phase precision are necessary to detect the inhomogeneity at the detector plane 3 cm from the center of the inhomogeneity. At this low level of scattering contrast, there is insufficient phase perturbation to be detected.

As in the pure scattering case, an increase in the scattering contrast decreases the amount of precision required to detect the object. Note that the straight solid line indicates the detection level, but the discontinuous solid line in the graph illustrates no scattering contrast. The absorption contrast causes a magnitude perturbation as seen before in the pure absorber case. When a scattering contrast is present, the resulting magnitude perturbation is in addition to the perturbation caused by the absorption contrast. A similar effect is seen in the phase. However, since the phase due to the absorption contrast is negative, but is positive due to the scattering contrast, the combination of the two is a lower phase amount than if there was no absorption contrast present. In other words, the phase perturbation due to an absorption contrast combines destructively with the perturbation due to a scattering contrast.

The maximum in both the magnitude and phase occurs at the inhomogeneity boundary at 0.5 cm. There is an additional  $0.2^\circ$  phase drop-off to the right of the object boundary due to the contrast in absorption.

#### 5.2.5 High Contrast in Absorption and Varied Contrast in Scattering Coefficients.

The inhomogeneity absorption coefficient is increased to three times the background medium value, meaning  $\mu_{a,in} = 0.15 \text{ cm}^{-1}$ . Again, the reduced scattering coefficient for the scatterer is varied to show the perturbations for high absorption contrast in the resulting wave. The plot in Figure 5.7 illustrates that at the detector plane at  $z = 3 \text{ cm}$ , as small as 8% amplitude and  $0.04^\circ$  phase precision is necessary to detect the inhomogeneity with 10% scattering contrast. Moving the detector plane does not increase the phase to a detectable level at this scattering contrast amount. If the scattering contrast is increased to 1.5 times that of the background, the phase precision increases to  $0.12^\circ$  and is sufficient to be detected. The corresponding magnitude precision increases only to 11%. As in

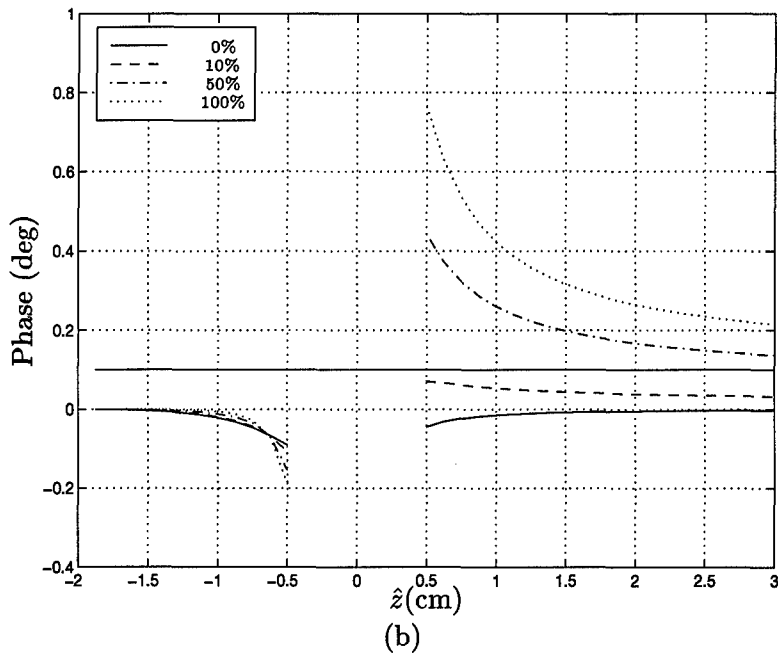
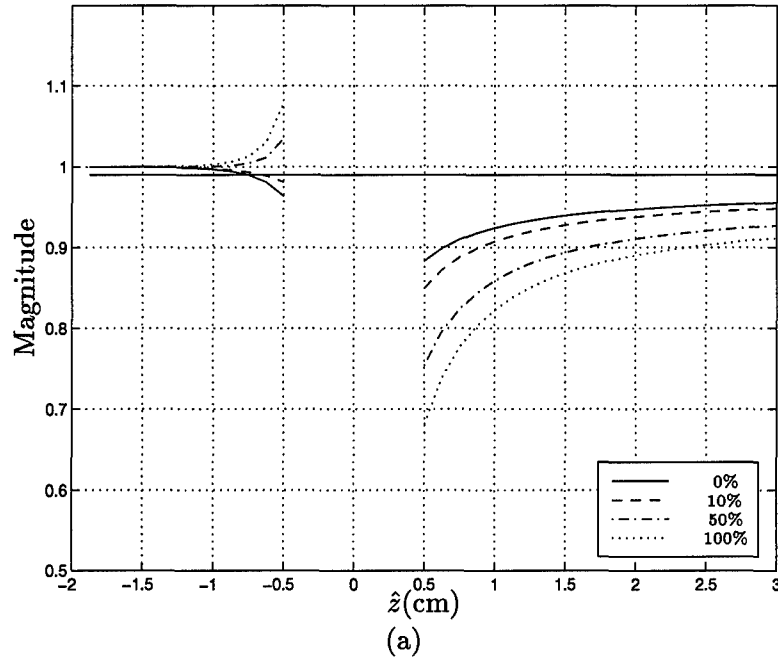


Figure 5.6 These plots show the (a) magnitude and (b) phase (degrees) of the analytic transfer function in the spatial domain for an inhomogeneity with low contrast in absorption and varied contrast in scattering along the  $\hat{z}$ -axis. The object scattering coefficient is varied as:  $\mu_{s,in} = 10 \text{ cm}^{-1}$  (solid line),  $\mu'_{s,in} = 11 \text{ cm}^{-1}$  (dashed line),  $\mu'_{s,in} = 15 \text{ cm}^{-1}$  (dashed-dotted line), and  $\mu'_{s,in} = 20 \text{ cm}^{-1}$  (dotted line). For both figures,  $\mu_{a,in} = 0.10 \text{ cm}^{-1}$ ,  $\mu_{a,out} = 0.05 \text{ cm}^{-1}$ , and  $\mu'_{s,out} = 10 \text{ cm}^{-1}$ . The straight solid line in each graph indicates the minimum detection level.

the previous case of a small amount of absorption contrast, the scattering and absorption contrast effects combine to cause a higher detectable amplitude and a lower detectable phase.

The location of the maximum in the phase occurs at the inhomogeneity boundary at 0.5 cm. Any additional phase drop-off to the right of the boundary is not noticeable.

Figure 5.8 shows the sensitivity of an inhomogeneity modeled with a very high absorption coefficient of  $\mu_{a,in} = 0.20 \text{ cm}^{-1}$ , or four times that of the background medium. For a 10% contrast in scattering, the necessary magnitude precision is 12% , and phase precision is  $0.04^\circ$ . Only the magnitude perturbation will be detected by most detectors.

Moving the detector plane towards the inhomogeneity, both the magnitude and phase increase. Yet, even at the boundary of the inhomogeneity at 10% contrast in scattering, the phase remains undetectable. However, scattering contrasts of 50% and 100% are detectable in the entire region between the inhomogeneity boundary and the detector plane at  $z=3$  cm. Consistent with the previous absorption contrast cases, the scattering and absorption contrasts effects combine to cause a higher detectable amount in the amplitude and a lower detectable amount in the phase. However the negative phase contribution due to the absorption contrast is minimal when compared to the phase amount due to the scattering contrast.

#### *5.2.6 Low Contrast in Scattering and Varied Contrast in Absorption Coefficients.*

The sensitivity of an inhomogeneity with a 10% increase in scattering, or  $\mu'_{s,in} = 11 \text{ cm}^{-1}$ , is investigated. To show the resulting perturbation in the DPDW, the absorption coefficient for the object is varied from no contrast to four times the value of the background medium. The plot in Figure 5.9 indicates that for an absorption contrast of 100%, 5% amplitude and  $0.03^\circ$  phase precision is necessary to detect the inhomogeneity at the detector plane 3 cm from the center of the inhomogeneity. The phase is not sufficient to be detected by most detectors. However, the amplitude is well above the necessary limits. As in the pure absorption case, an increase in the absorption contrast decreases the amount of magnitude precision required to detect the object. With the small amount of scattering contrast present, the resulting magnitude perturbation is in addition to that caused by

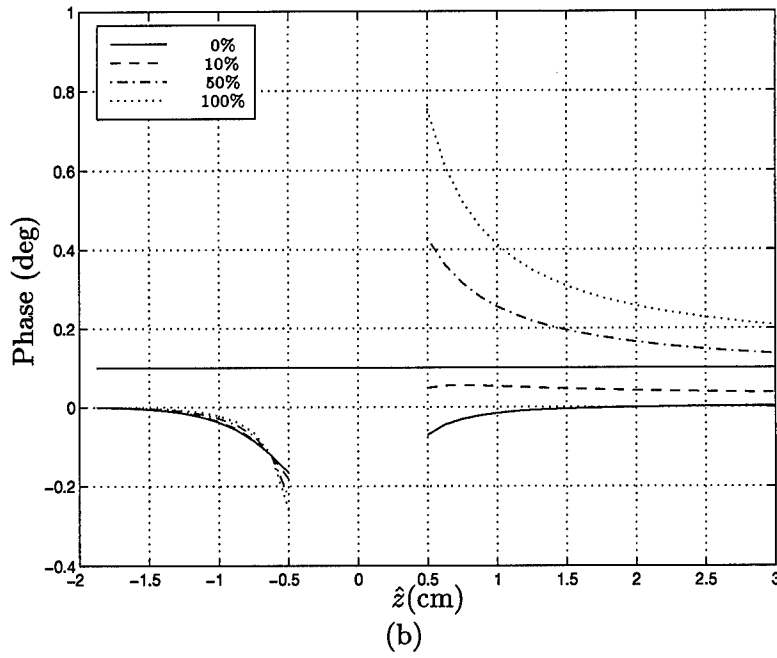
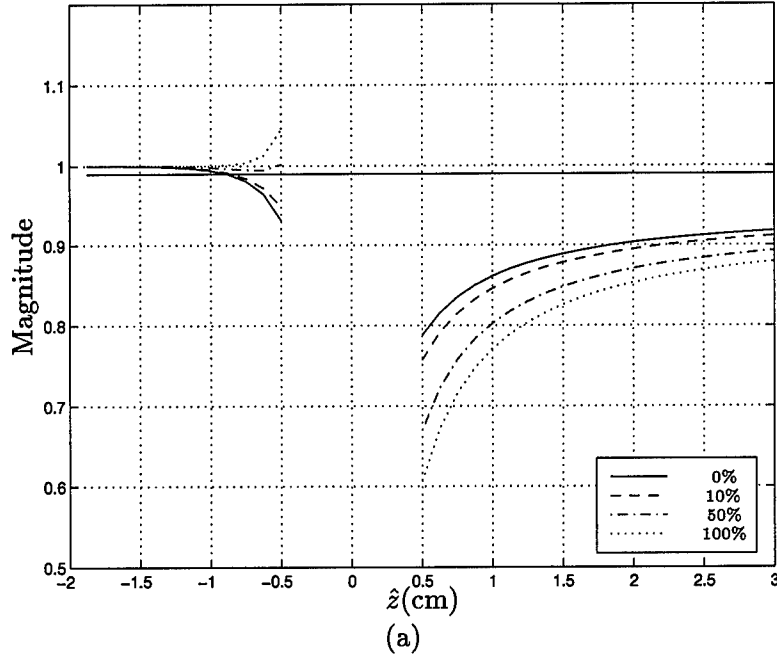


Figure 5.7 These plots show the (a) magnitude and (b) phase (degrees) of the analytic transfer function in the spatial domain for an inhomogeneity with high contrast in absorption and varied contrast in scattering along the  $\hat{z}$ -axis. The object scattering coefficient is varied as:  $\mu'_{s,in} = 10 \text{ cm}^{-1}$  (solid line),  $\mu'_{s,in} = 11 \text{ cm}^{-1}$  (dashed line),  $\mu'_{s,in} = 15 \text{ cm}^{-1}$  (dashed-dotted line), and  $\mu'_{s,in} = 20 \text{ cm}^{-1}$  (dotted line). For both figures,  $\mu_{a,in} = 0.15 \text{ cm}^{-1}$ ,  $\mu_{a,out} = 0.05 \text{ cm}^{-1}$ , and  $\mu'_{s,out} = 10 \text{ cm}^{-1}$ . The straight solid line in each graph indicates the minimum detection level.

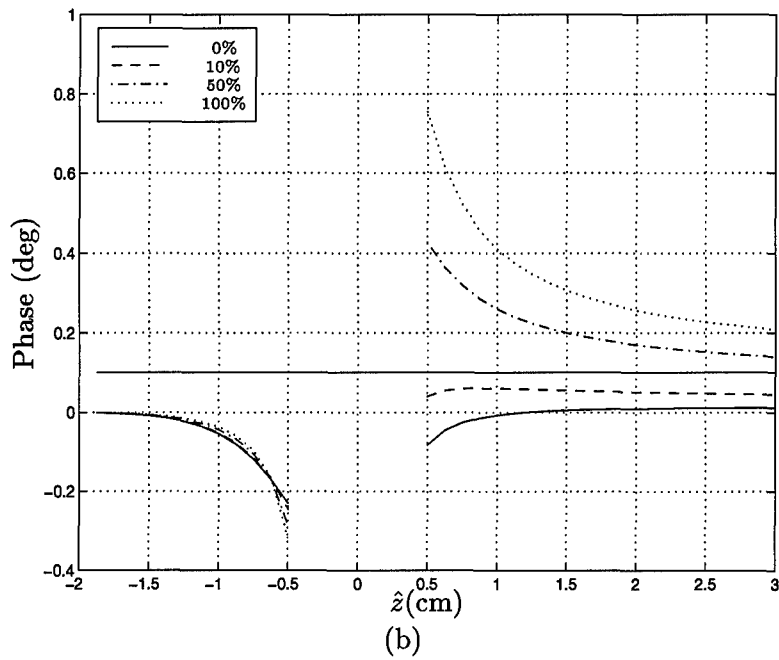
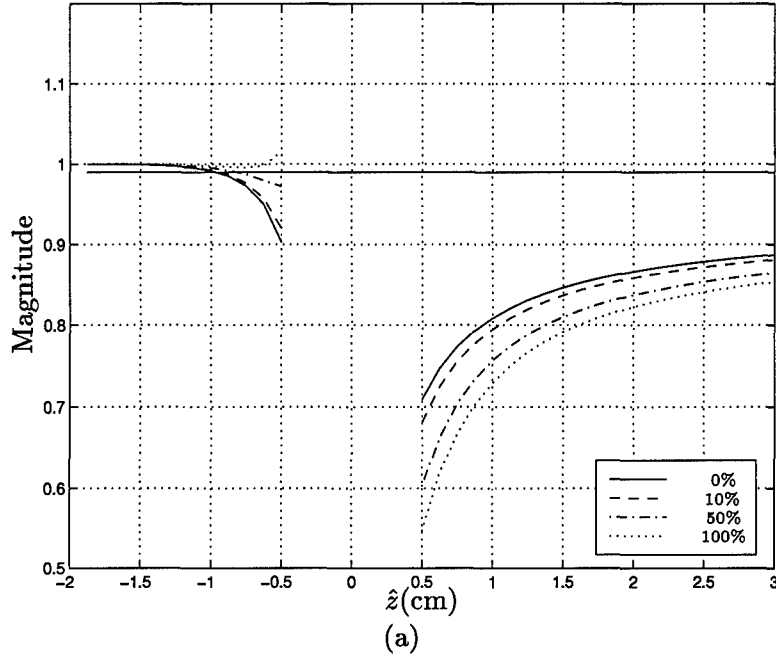


Figure 5.8 These plots show the (a) magnitude and (b) phase (degrees) of the analytic transfer function in the spatial domain for an inhomogeneity with very high contrast in absorption and varied contrast in scattering along the  $\hat{z}$ -axis. The object scattering coefficient is varied as:  $\mu'_{s,in} = 10 \text{ cm}^{-1}$  (solid line),  $\mu'_{s,in} = 11 \text{ cm}^{-1}$  (dashed line),  $\mu'_{s,in} = 15 \text{ cm}^{-1}$  (dashed-dotted line), and  $\mu'_{s,in} = 20 \text{ cm}^{-1}$  (dotted line). For both figures,  $\mu_{a,in} = 0.20 \text{ cm}^{-1}$ ,  $\mu_{a,out} = 0.05 \text{ cm}^{-1}$ , and  $\mu'_{s,out} = 10 \text{ cm}^{-1}$ . The straight solid line in each graph indicates the minimum detection level.

increased absorption contrast. A similar effect is seen in the phase on the right side of the inhomogeneity (i.e. along the positive  $\hat{z}$  direction). The magnitude perturbation is detectable for all levels of absorption contrast regardless of the detector position. However, the corresponding phase perturbation is not detectable at any point in the region.

### 5.2.7 High Contrast in Scattering and Varied Contrast in Absorption Coefficients.

The scattering contrast is increased to 50%, meaning the inhomogeneity has a scattering coefficient of  $\mu'_{s,in} = 15 \text{ cm}^{-1}$ . Again, the absorption coefficient for the object is varied to show the perturbation effects on the DPDW. Figure 5.10 illustrates that in the region between the inhomogeneity boundary and the boundary of the system at 3 cm, both the magnitude and the phase amounts are detectable for all absorption contrast amounts. The precision required to detect a change in the magnitude or the phase decreases as the detector plane is moved towards the center of the inhomogeneity. Additional increase in absorption contrast does not significantly perturb the phase further.

Figure 5.11 shows the sensitivity of an inhomogeneity modeled with a very high scattering coefficient of  $\mu'_{s,in} = 20 \text{ cm}^{-1}$ , or double that of the background medium. As in the previous scattering contrast case, both the magnitude and phase amounts are detectable for all absorption contrast variations in the region bounded by the inhomogeneity and the detector plane at  $z=3 \text{ cm}$ .

Consistent with the previous scattering contrast cases, the scattering and absorption contrasts effects combine to cause a higher detectable amount in the amplitude. However, the absorption coefficient has little effect on the detectability of the phase.

**5.2.8 Summary of Sensitivity Analysis.** In this section, the amount of perturbation in the total wave was examined for various combinations of optical contrasts between the inhomogeneity and the surrounding medium. The results show that a high absorptive contrast causes a decrease in the magnitude of the perturbed wave but does not significantly affect the phase. However, a scattering contrast causes a significant change in the phase of the perturbed wave but minimally affects the magnitude. A combination of two contrasts combine their effects in the magnitude and the phase of the total wave.

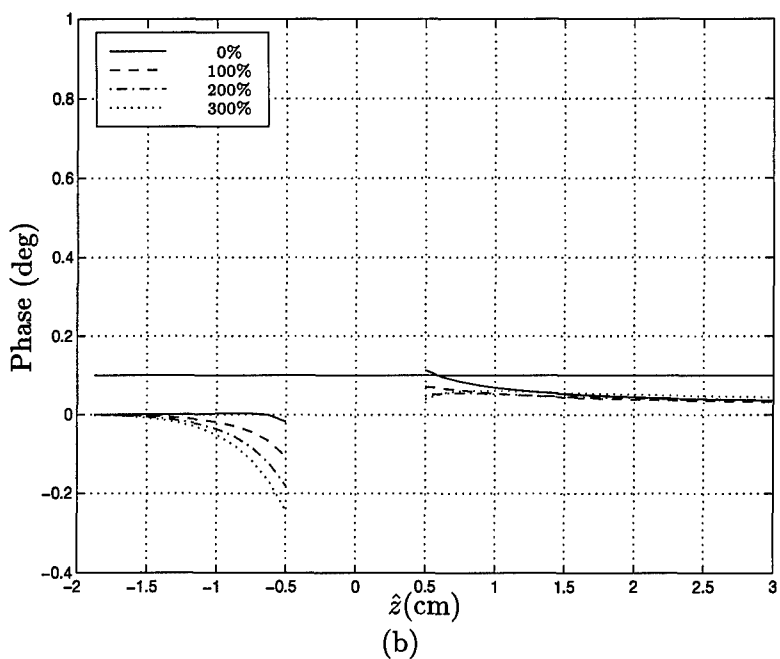
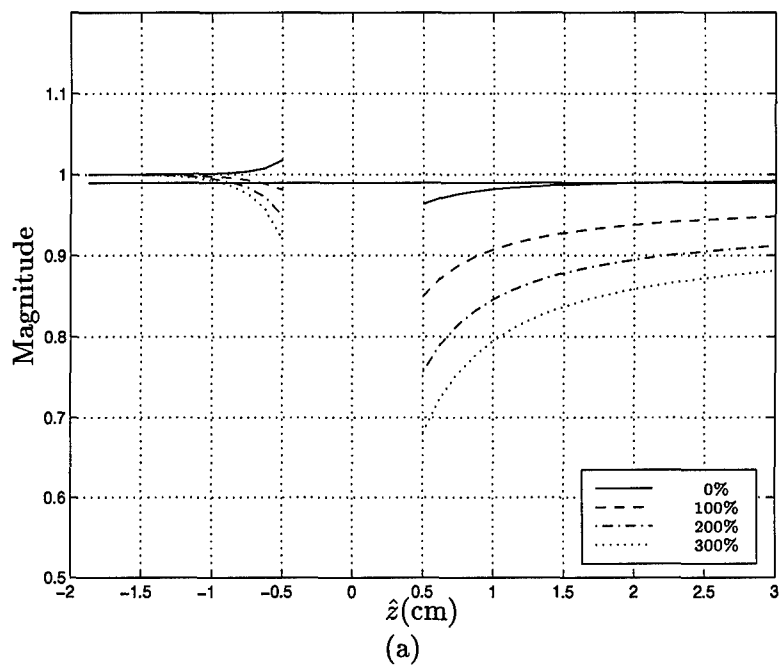


Figure 5.9 These plots show the (a) magnitude and (b) phase (degrees) of the analytic transfer function in the spatial domain for an inhomogeneity with low contrast in scattering and varied contrast in absorption along the  $\hat{z}$ -axis. The object absorption coefficient is varied as:  $\mu_{a,in} = 0.05 \text{ cm}^{-1}$  (solid line),  $\mu_{a,in} = 0.10 \text{ cm}^{-1}$  (dashed line),  $\mu_{a,in} = 0.15 \text{ cm}^{-1}$  (dashed-dotted line), and  $\mu_{a,in} = 0.20 \text{ cm}^{-1}$  (dotted line). For both figures,  $\mu'_{s,in} = 11 \text{ cm}^{-1}$ ,  $\mu_{a,out} = 0.05 \text{ cm}^{-1}$ , and  $\mu'_{s,out} = 10 \text{ cm}^{-1}$ . The straight solid line in each graph indicates the minimum detection level.

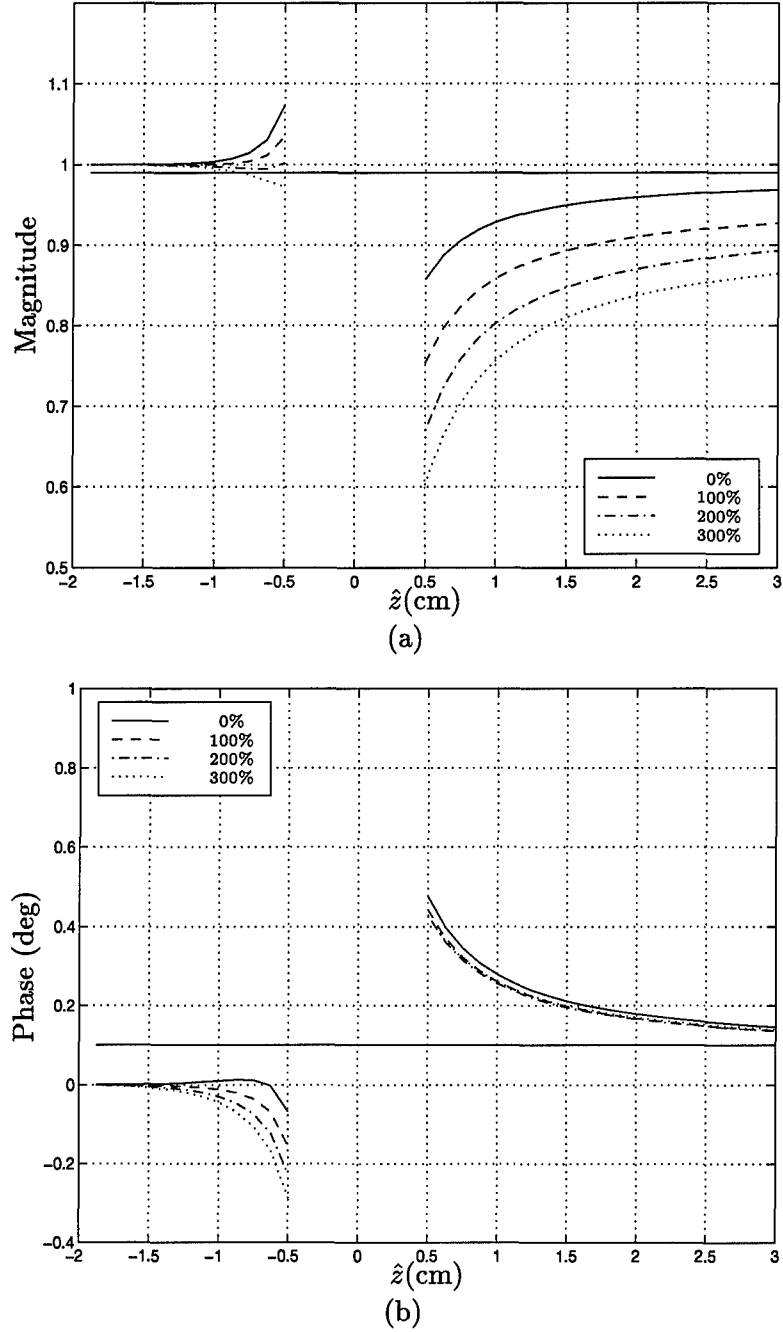
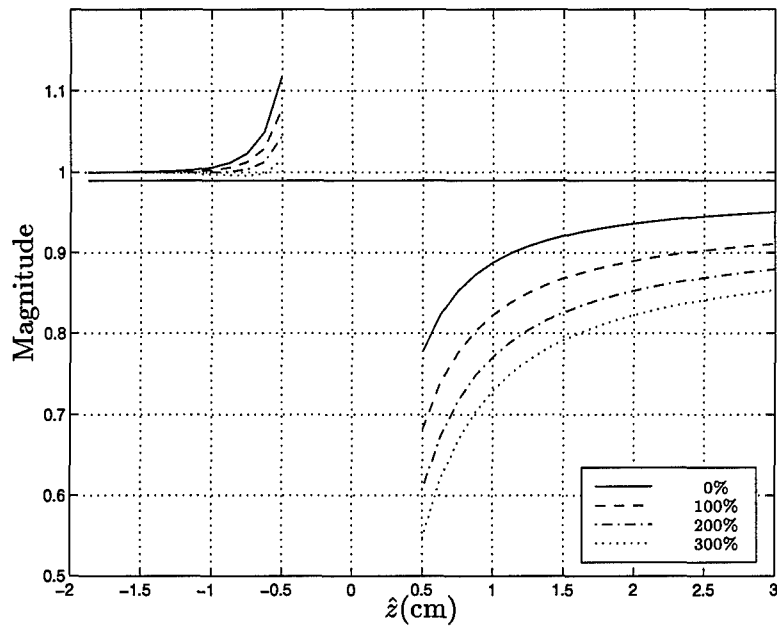
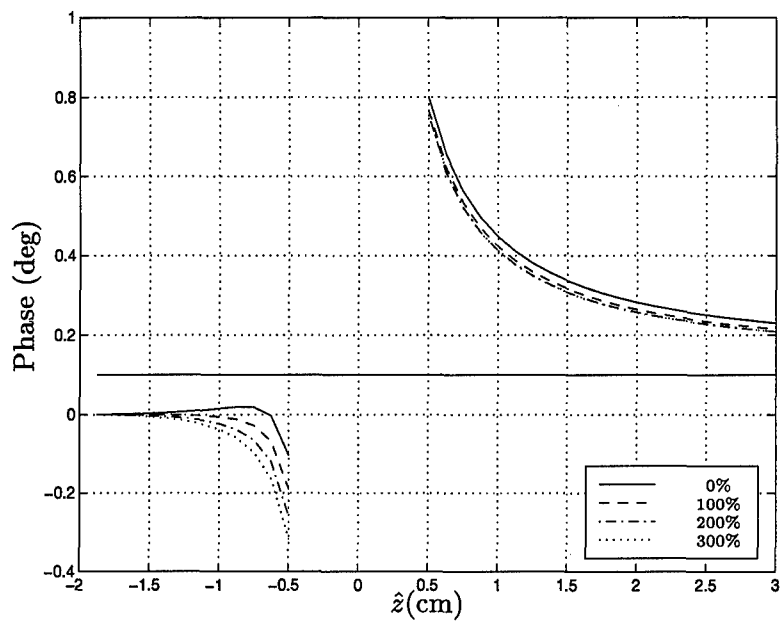


Figure 5.10 These plots show the (a) magnitude and (b) phase (degrees) of the analytic transfer function in the spatial domain for an inhomogeneity with high contrast in scattering and varied contrast in absorption coefficients along the  $\hat{z}$ -axis. The object absorption coefficient is varied as:  $\mu_{a,in} = 0.05 \text{ cm}^{-1}$  (solid line),  $\mu_{a,in} = 0.10 \text{ cm}^{-1}$  (dashed line),  $\mu_{a,in} = 0.15 \text{ cm}^{-1}$  (dashed-dotted line), and  $\mu_{a,in} = 0.20 \text{ cm}^{-1}$  (dotted line). For both figures,  $\mu'_{s,in} = 15 \text{ cm}^{-1}$ ,  $\mu_{a,out} = 0.05 \text{ cm}^{-1}$ , and  $\mu'_{s,out} = 10 \text{ cm}^{-1}$ . The straight solid line in each graph indicates the minimum detection level.



(a)



(b)

Figure 5.11 These plots show the (a) magnitude and (b) phase (degrees) of the analytic transfer function in the spatial domain for an inhomogeneity with very high contrast in scattering and varied contrast in absorption along the  $\hat{z}$ -axis. The object absorption coefficient is varied as:  $\mu_{a,in} = 0.05 \text{ cm}^{-1}$  (solid line),  $\mu_{a,in} = 0.10 \text{ cm}^{-1}$  (dashed line),  $\mu_{a,in} = 0.15 \text{ cm}^{-1}$  (dashed-dotted line), and  $\mu_{a,in} = 0.20 \text{ cm}^{-1}$  (dotted line). For both figures,  $\mu'_{s,in} = 20 \text{ cm}^{-1}$ ,  $\mu_{a,out} = 0.05 \text{ cm}^{-1}$ , and  $\mu'_{s,out} = 10 \text{ cm}^{-1}$ . The straight solid line in each graph indicates the minimum detection level.

The sensitivity results also showed that the location of the detector plane relative to the inhomogeneity determines the amount of perturbation detected. The maximum change in both the amplitude and the phase in the total wave occurred at the boundary of the inhomogeneity, assuming the object is between the source and detector. This maximum position can be used to determine the depth of the object.

Differing optical parameters are only one perturbative effect. In the next section the disruption in the DPDW caused by variations in the size of the inhomogeneity is examined.

### 5.3 Sensitivity to Inhomogeneity Size

The perturbation of the incident wave due to an inhomogeneity is directly dependent on the size of the inhomogeneity. The analytic analysis in Section 2.4.1 showed this relationship. It has been shown that for an absorption contrast of three times that of the background medium, or a scattering contrast factor of 1.5, an inhomogeneity can be detected [13]. For a mix of low contrast in absorption and scattering relative to the background medium, size is a critical factor in perturbing the wave to a level of detection ability. The system is configured as described in Section 5.2.1. Figure 5.12 illustrates the sensitivity levels of different sizes of inhomogeneities that have weakly perturbing optical characteristics of 100% in absorption contrast and 10% in scattering contrast with the background medium, namely  $\mu_a = 0.10 \text{ cm}^{-1}$  and  $\mu'_s = 11 \text{ cm}^{-1}$ .

At the detector plane, for a detector minimum limit of 1.0% magnitude perturbation (indicated by the straight solid line), only the 6 mm, 8 mm and 10 mm diameter objects can be decisively detected. For a minimum limit of  $0.1^\circ$  phase (also indicated by the straight solid line), none of the objects are detectable. If the detector plane is moved to the peak amount of each object, all save the 1 mm diameter object can be detected by magnitude. Only the 10 mm object is detected on phase perturbation alone and requires the detector to be on the same side of the object as the source, consequently violating the system geometry.

### 5.4 Scattering Moment Contributions

In Chapter II, the scattering wave was shown to be comprised of a series of moments that depended on, among other quantities, the contrast of optical properties. If the conditions  $|k_{out}a| \ll 1$  and  $|k_{in}a| \ll 1$  are valid, where  $k_{out}$  ( $k_{in}$ ) is the wavenumber outside (inside) the inhomogeneity with radius  $a$ , only the first three moments of the series are detectable in experiments due to signal-to-noise limitations [13].

However, if the conditions mentioned above are not met, additional moments are detectable. For the contrast cases listed in Table 4.3 and for a 1 cm diameter inhomogeneity,  $|k_{in}a| = 1.069$ , and  $|k_{out}a|$  ranges from 0.6143 to 0.6158. These values do not conclusively

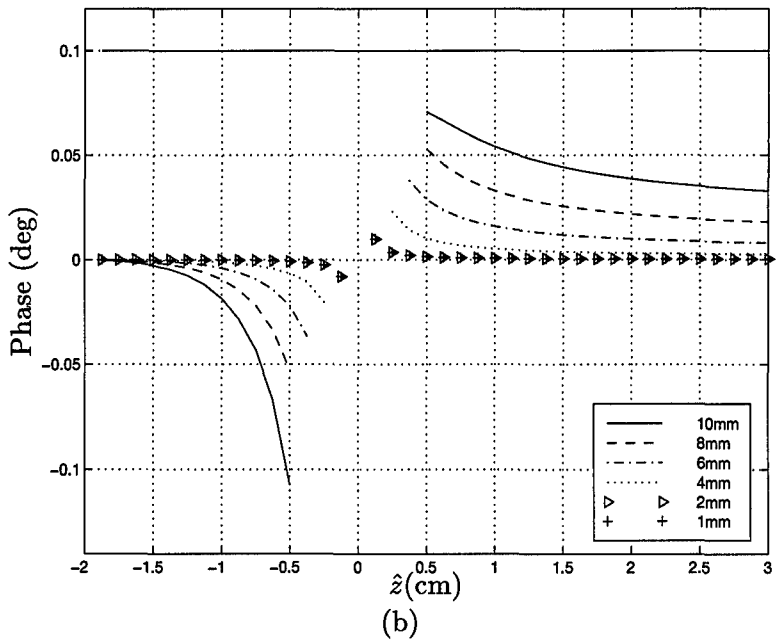
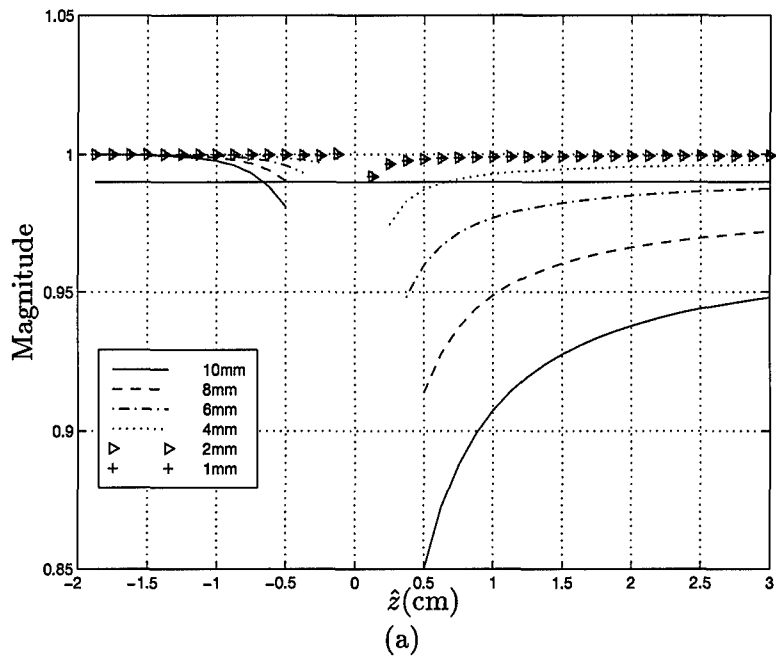


Figure 5.12 These sensitivity plots show the (a) magnitudes and (b) phases (degrees) of the transfer function in the spatial domain with low contrast in scattering absorption coefficients along the  $\hat{z}$ -axis. The diameter of the inhomogeneity is varied as: 10 mm (solid line), 8 mm (dashed line), 6 mm (dashed-dotted line), and 4 mm (dotted line), 2 mm ( $\triangleright$ ), 1 mm ( $+$ ). For both figures,  $\mu_{a,in} = 0.10 \text{ cm}^{-1}$ ,  $\mu'_{s,in} = 11 \text{ cm}^{-1}$ ,  $\mu_{a,out} = 0.05 \text{ cm}^{-1}$ , and  $\mu'_{s,out} = 10 \text{ cm}^{-1}$ . The straight solid line in each graph indicates the minimum detection level.

meet the conditions, so scattered wave moments in addition to the first three are expected to have significant contributions to the total perturbation caused by the inhomogeneity.

The first moment (monopole) was shown in Section 2.4.1 to be predominantly affected by a change in absorptive contrasts, while the second (dipole) and third (quadrupole) moments were affected by scattering contrasts. In Section 5.2.1, the sensitivity analysis determined that although contrasts in either absorption or scattering caused a detectable amount in the amplitude, the absorption contrast caused a higher detectable amount than the scattering contrast. In addition, the sensitivity results are consistent in the moment analysis of a pure absorber and pure scatterer, as well as mixed contrast cases.

In this section, the contributions of the first six moments in the scattered wave are investigated for several of the perturbative cases listed in Table 4.3. The contribution of an individual moment is determined by the absolute value of the ratio of the magnitude and phase of the scattered wave moment and the incident wave. The particular cases considered in this section include a pure absorber, a pure scatterer, and inhomogeneities with low and high absorptive and low and high scattering contrasts. The very high contrast cases are not investigated since the focus of this research is on weak perturbations caused by low contrasts in the optical properties.

*5.4.1 Pure Absorption.* In Figures 5.13 and 5.14, a pure absorber with a high and low absorption contrast are illustrated, respectively. Overall, a higher contrast in absorption causes a greater amount of perturbation in the magnitude of the wave than a lower contrast case causes. Specifically, for an inhomogeneity with an absorption coefficient three times that of the background medium induces twice the amount of amplitude change than an inhomogeneity with an absorption coefficient only twice that of the background medium. The dominant moment for a pure absorber is the monopole. Each additional moment contributes to the magnitude perturbation on the order of a factor of 10 less per moment. For example, the dipole moment is a factor of 10 less than the monopole but the quadrupole is a factor of 100 less than the monopole.

As expected from the sensitivity analysis of Section 5.2.2, various levels of absorption contrast have negligible effect on the phase perturbations. The contributions of the moments in order of the most significant is the first through the sixth moments.

*5.4.2 Pure Scatterer.* For a pure scatterer, there are similar trends in amplitude change due to increased contrast, as in the pure absorption case. Figures 5.15 and 5.16 depict high and low contrast cases for a pure scatterer, respectively. The high contrast case describes an inhomogeneity with a reduced scattering coefficient 50% higher than the background medium. The high contrast causes an average increase of 3.8 times the amount of amplitude change that the low contrast case causes, where a low scattering contrast is defined by an inhomogeneity with a reduced scattering coefficient only 10% higher than the surrounding medium. The contributions by moments in the pure scatterer case are significantly different than in the pure absorptive case. If the detector plane is more than a radius distance from the inhomogeneity boundary, the second and third moments are the major contributors to the perturbation. The first moment ranks third. However, consistent in both the low and high scattering contrast cases, within a radius distance of the inhomogeneity, the fourth and fifth moments contribute more than the monopole. This means that in the detection of pure scatterers, the position of the detection plane is an important consideration when determining how many moments to include in the infinite series representing the scattered wave (Equation (2.11)).

There is no noticeable phase change in the contributions from the individual moments due to an increase in scattering contrast. However, the monopole contributes the least amount to the phase perturbation, as expected from the sensitivity results in Section 5.2.3. An interesting behavior of the monopole shows that the amount of its phase contribution depends on the detector plane location.

*5.4.3 High Absorption Contrast.* The presence of a high absorption and two different levels (high and low) of scattering contrast cause different amounts of change in the magnitude of the perturbed wave. The contributions of the moments also vary depending on the amount of absorptive contrast relative to the scattering contrast present in the system. Figures 5.17 and 5.18 illustrate these mixed contrast cases.

Figure 5.17 depicts a high absorptive, high scattering contrast case. Respectively, the inhomogeneity coefficients are a factor of 3 and a factor of 1.5 of the coefficient values of the surrounding medium. The first moment is the major contributor to the perturbation, while the contributions of the next five moments monotonically decrease. The presence of the high scattering contrast relative to no contrast (Figure 5.13) causes an increase in contributions from the third through the sixth moments by average factors of 9, 30, 50, and 150, respectively. Note that near the inhomogeneity, the second moment is not affected by the increase in the scattering contrast. This contribution variation indicates the second moment depends on the detector plane location.

Keeping a high absorptive contrast present but lowering the scattering contrast so the inhomogeneity scattering coefficient is only a factor of 1.1 of the coefficient of the surrounding medium, the resulting moment contributions to the magnitude perturbation are depicted in Figure 5.18. The respective contributions of the second through sixth moments are not as great as that in the high scattering contrast case. However, the contribution of the second moment is dependent on the detector plane location. Overall, the first moment dominates the magnitude perturbation. At a minimum, the monopole is 26 times the amount of the dipole, which is the next highest contributing moment.

Figures 5.17 and 5.18 depicting an inhomogeneity with a high absorptive contrast relative to the background medium, show that increasing the scattering contrast causes a corresponding increase in the contributions from the third through the sixth moments. The second moment contribution increases when the detector plane is not close to the boundary of the inhomogeneity. Overall, the monopole is the major contributor to the perturbation in the amplitude.

The presence of absorption causes the monopole to also be the major contributor to the phase perturbations. However, increasing the inhomogeneity scattering coefficient from 110% to 150% of the background medium (low to high contrast) causes a  $0.05^\circ$  decrease in the second moment and a  $0.01^\circ$  increase in the third moment. The remaining moments are unaffected by the increase in the scattering contrast.

*5.4.4 Low Absorptive Contrast.* Similar to the cases involving a high absorptive contrast, magnitude perturbations are additionally affected by increasing scattering contrast levels. The low absorptive contrast with low and high scattering contrast cases are graphed in Figures 5.19 and 5.20, respectively.

The dominant contributor to the magnitude perturbations is the first moment. However, a low scattering contrast as shown in Figure 5.19 causes an average decrease of a factor of 10 in the contribution of the second moment as compared to the case with no scattering present (Figure 5.14). Increasing the inhomogeneity scattering coefficient to 150% that of the surrounding medium, the contributions from the second through sixth moments are on the order of 20 times higher than in the no scattering case as seen in Figure 5.20. Low scattering contrast in the presence of a low absorption contrast significantly decreases the dipole moment, but that effect is overcome by increasing the scattering contrast.

The monopole also is the major contributor to the phase perturbations due to the presence of an absorption contrast. An increase in the scattering contrast causes an increase in the second moment by  $0.05^\circ$ . The remaining moments are unaffected.

*5.4.5 High Scattering Contrast.* Consider the cases with a fixed high scattering contrast. The effects caused by increasing the absorption contrast are graphed in Figures 5.20 and 5.17, respectively.

In a pure scattering case as shown before in Figure 5.15, the dipole moment is the major contributor to the magnitude perturbations. When a low absorption contrast is introduced into the system, the monopole becomes the dominant moment (see Figure 5.20). The second through sixth moments are not affected by a low absorption contrast of 100% that of the surrounding medium. As the absorption contrast increases to a level of 200% that of the background medium, a corresponding increase by a factor of 2 in the monopole moment is apparent in Figure 5.17. The dipole moment decreases by an average factor of 0.8, and moments three through six are not noticeably changed.

In the presence of high scattering contrast, an increase in absorption contrast significantly increases the magnitude perturbations contributed by the first moment, and to a lesser degree, decreases the third moment.

Increasing the inhomogeneity absorption coefficient from 100% to 200% that of the background medium (low to high contrast) does not affect the phase perturbation moment contributions. This behavior is expected since the results from Section 5.2.2 showed that in the presence of a high scattering contrast, the absorption contrast does not significantly affect the distortion in the phase of the perturbed wave.

*5.4.6 Low Scattering Contrast.* Decreasing the reduced scattering coefficient of the inhomogeneity to a 10% contrast with the background medium increases the effect that an absorptive contrast has on the magnitude perturbation caused by the presence of an inhomogeneity. Figures 5.18 and 5.19 illustrate, respectively, the effects high and low absorptive contrasts have with a low scattering contrast.

Similar to the high scattering contrast case in the previous section, the presence of an absorptive contrast causes the monopole to become the dominant moment. Comparing Figure 5.18 to Figure 5.19 shows that increasing the absorption contrast 200% causes a corresponding doubling of the amount the monopole moment contributes to the magnitude perturbations. The only other increase is in the dipole moment of an average factor of 1.25, while the quadrupole moment contribution is halved. The monopole, however, is 26 times larger than the dipole, which is the next highest contributing moment. The fourth through the sixth moments are unaffected by the increase in absorption.

The presence of an absorption contrast enables the first moment to be the main contributor to the magnitude perturbations. Higher levels of absorption contrast do not increase the other moments to be significant contributors in changing the magnitude of the perturbed wave.

Comparing the phase moment graphs in Figures 5.18 and 5.19 shows that an increase from 100% to 200% contrast in absorption contrast causes a  $0.1^\circ$  increase in the second phase moment. The low scattering contrast enables a change in absorption contrast to affect the phase. The remaining moments are unaffected by the increase in absorption contrast. However, the presence of some absorption contrast causes the monopole to be the major contributor to the phase perturbations.

*5.4.7 Summary of Moment Analysis.* In the absence of any absorption contrast, the magnitude and phase perturbations are dominated by the second (dipole) and third (quadrupole) moments of the scattered wave. Adding an absorption contrast causes the first moment, or the monopole, to be the major contributor to both the magnitude and phase perturbations. In the presence of a high absorption contrast, a low scattering contrast lowers the magnitude perturbation contribution made by the second moment, while an increase in the scattering contrast causes a corresponding increase in the second, as well as the third through sixth moments. The monopole moment remains largely unaffected by the presence of any scattering contrast.

Presence of an absorption contrast affects the phase moments only if there is a low scattering contrast. In that situation, the monopole moment dominates, and the remaining moments monotonically decrease in contribution order. If scattering contrast dominates the phase perturbations, the monopole moment falls to sixth rank, and the second through the fifth moments are the major contributors.

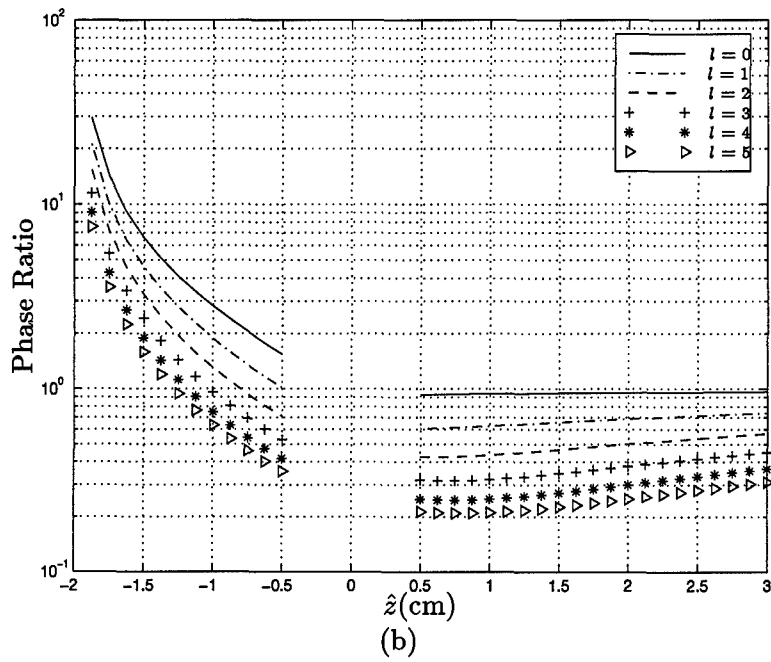
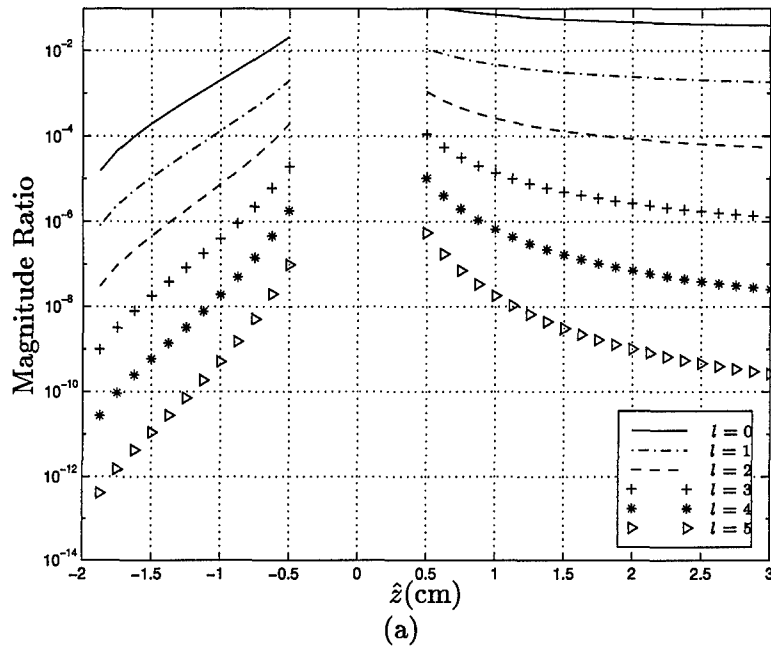


Figure 5.13 The first six moment (a) amplitude and (b) phase contributions of the scattered wave to the incident wave are plotted for a pure absorber with high contrast, along the  $\hat{z}$ -axis. For both figures,  $\mu_{a,out} = 0.05 \text{ cm}^{-1}$ ,  $\mu'_{s,out} = 10 \text{ cm}^{-1}$ ,  $\mu_{a,in} = 0.15 \text{ cm}^{-1}$ ,  $\mu'_{s,in} = 10 \text{ cm}^{-1}$ .

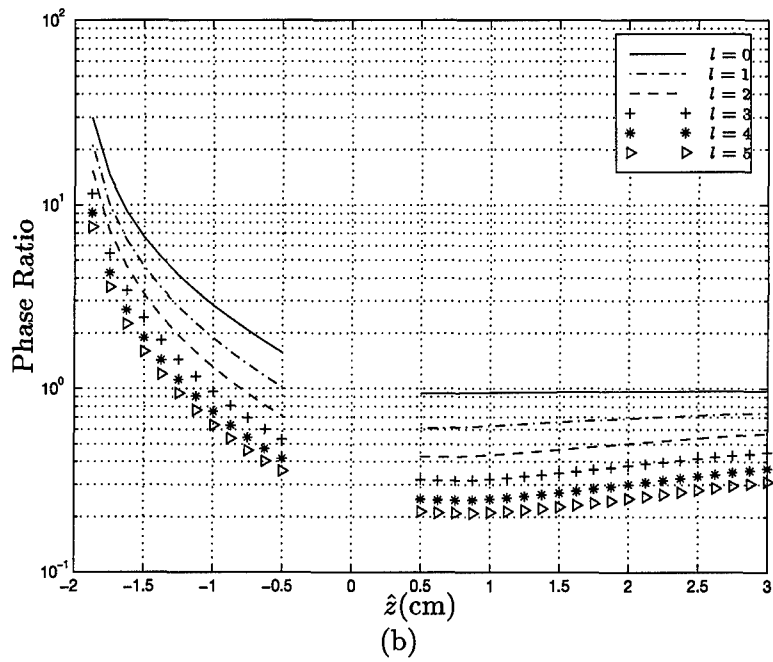
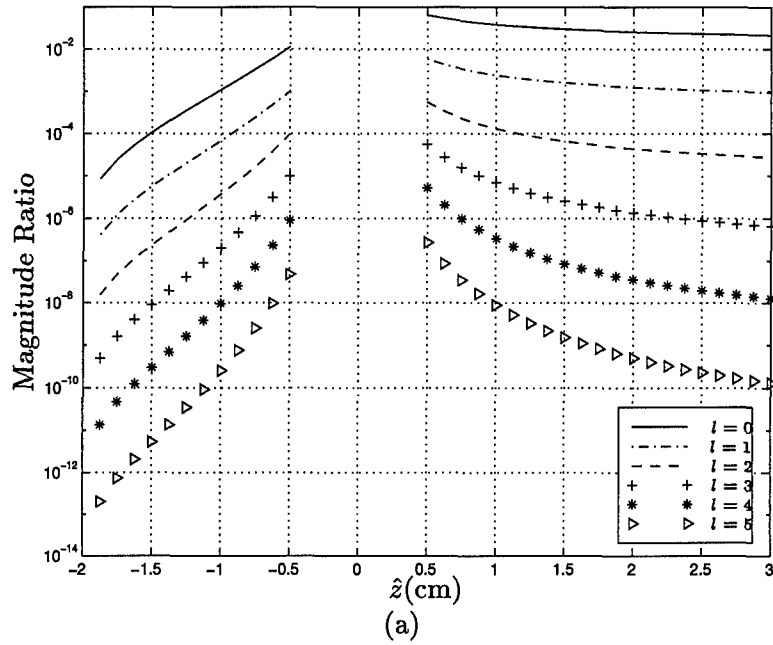


Figure 5.14 The first six moment (a) amplitude and (b) phase contributions of the scattered wave to the incident wave are plotted for a pure absorber with low contrast, along the  $\hat{z}$ -axis. For both figures,  $\mu_{a,out} = 0.05 \text{ cm}^{-1}$ ,  $\mu'_{s,out} = 10 \text{ cm}^{-1}$ ,  $\mu_{a,in} = 0.10 \text{ cm}^{-1}$ ,  $\mu'_{s,in} = 10 \text{ cm}^{-1}$ .

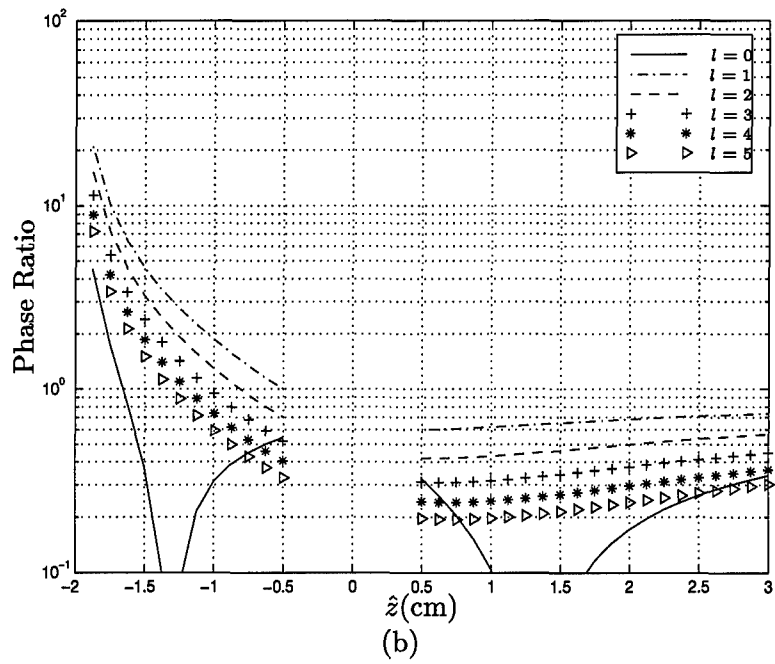
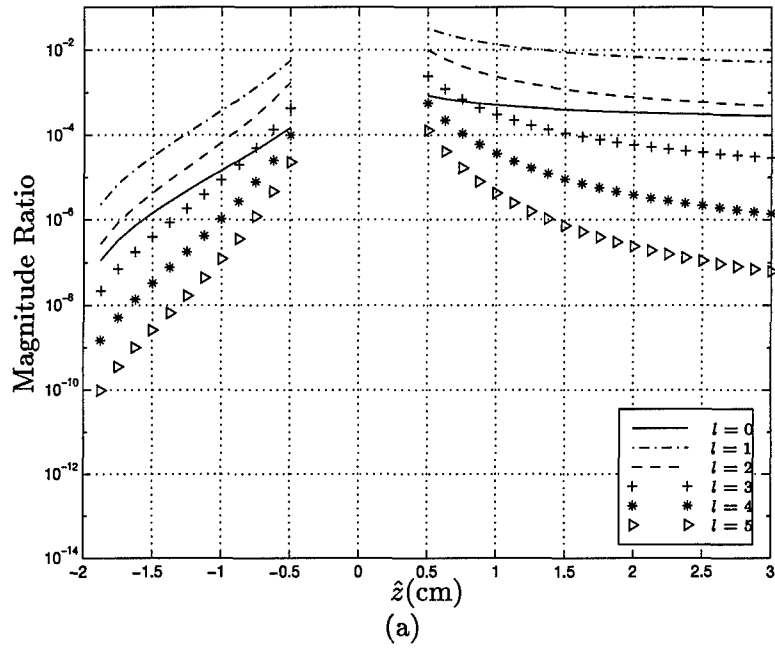


Figure 5.15 The first six moment (a) amplitude and (b) phase contributions of the scattered wave to the incident wave are plotted for a pure scatterer with high contrast, along the  $\hat{z}$ -axis. For both figures,  $\mu_{a,out} = 0.05 \text{ cm}^{-1}$ ,  $\mu'_{s,out} = 10 \text{ cm}^{-1}$ ,  $\mu_{a,in} = 0.05 \text{ cm}^{-1}$ ,  $\mu'_{s,in} = 15 \text{ cm}^{-1}$ .

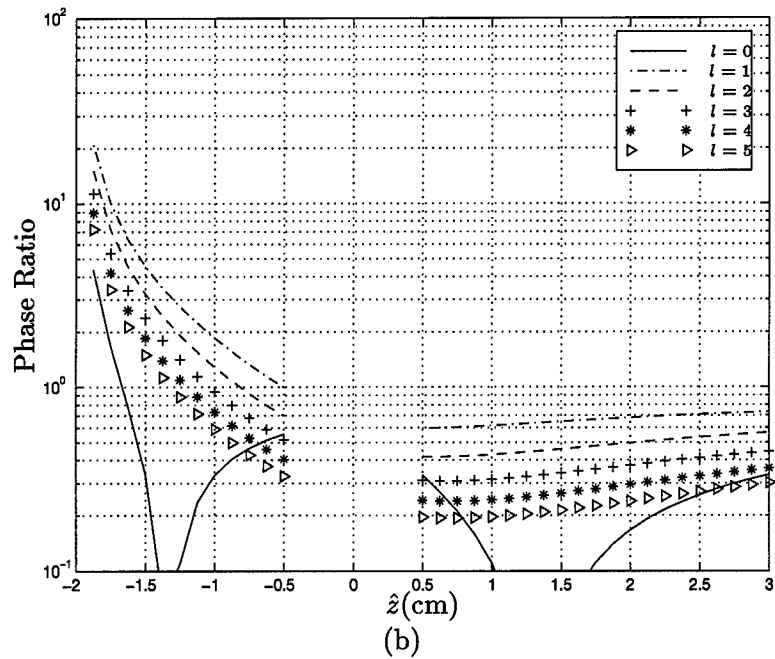
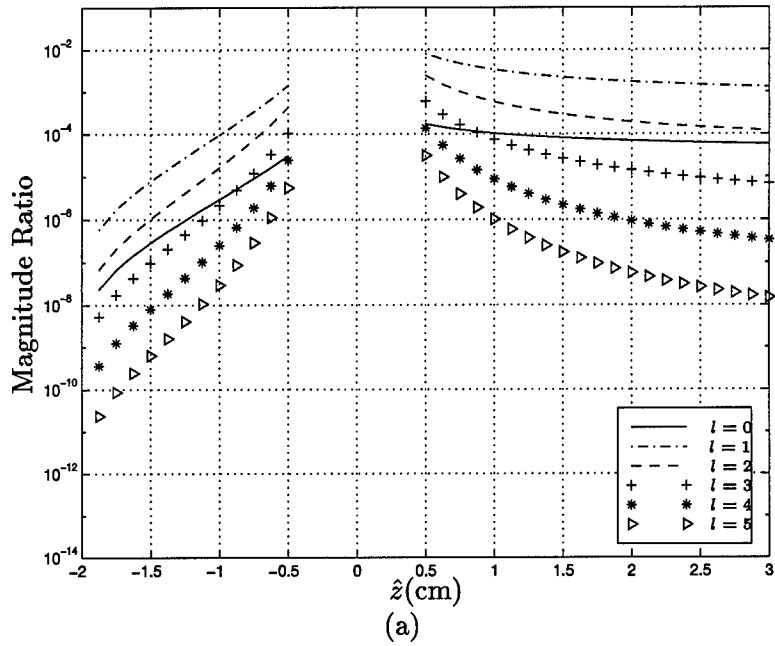


Figure 5.16 The first six moment (a) amplitude and (b) phase contributions of the scattered wave to the incident wave are plotted for a pure scatterer with low contrast, along the  $\hat{z}$ -axis. For both figures,  $\mu_{a,out} = 0.05 \text{ cm}^{-1}$ ,  $\mu'_{s,out} = 10 \text{ cm}^{-1}$ ,  $\mu_{a,in} = 0.05 \text{ cm}^{-1}$ ,  $\mu'_{s,in} = 11 \text{ cm}^{-1}$ .

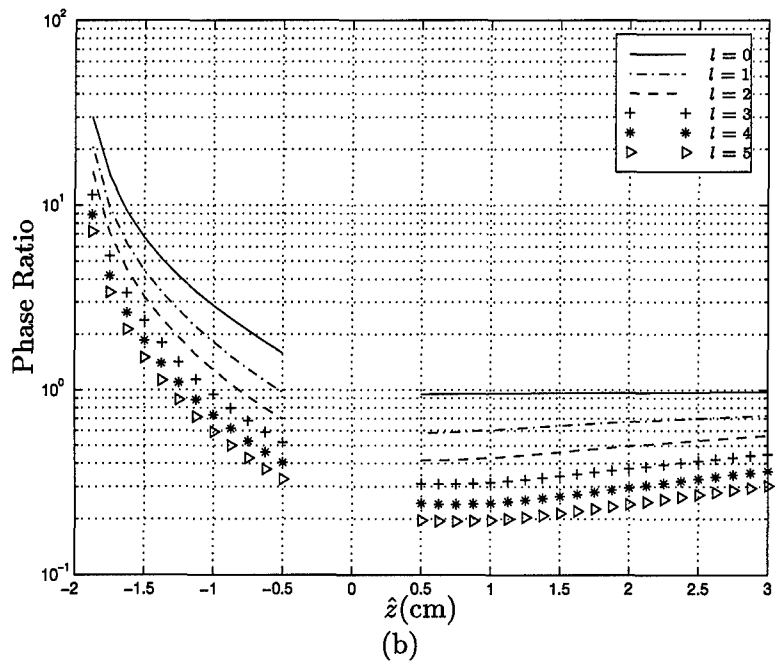
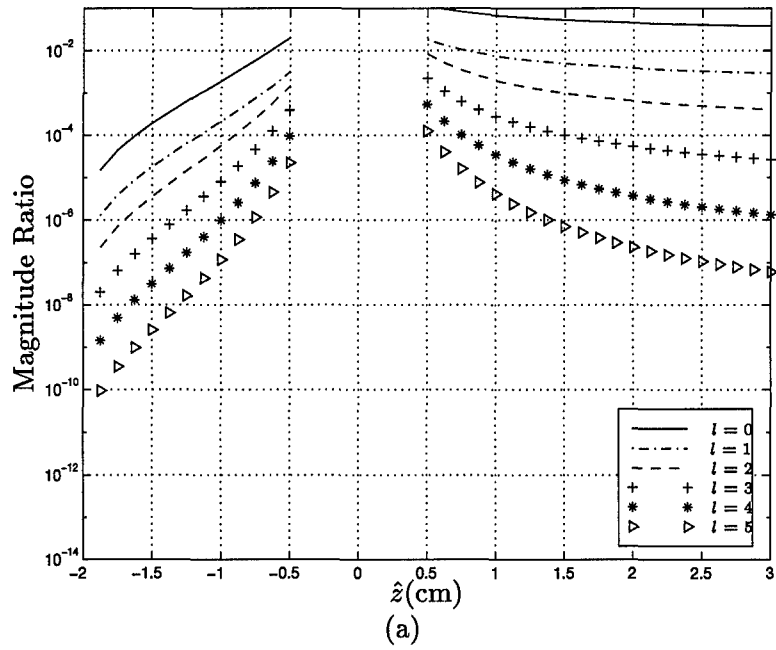


Figure 5.17 The first six moment (a) amplitude and (b) phase contributions of the scattered wave to the incident wave are plotted for high contrast in absorption and scattering, along the  $\hat{z}$ -axis. For both figures,  $\mu_{a,out} = 0.05 \text{ cm}^{-1}$ ,  $\mu'_{s,out} = 10 \text{ cm}^{-1}$ ,  $\mu_{a,in} = 0.15 \text{ cm}^{-1}$ ,  $\mu'_{s,in} = 15 \text{ cm}^{-1}$ .

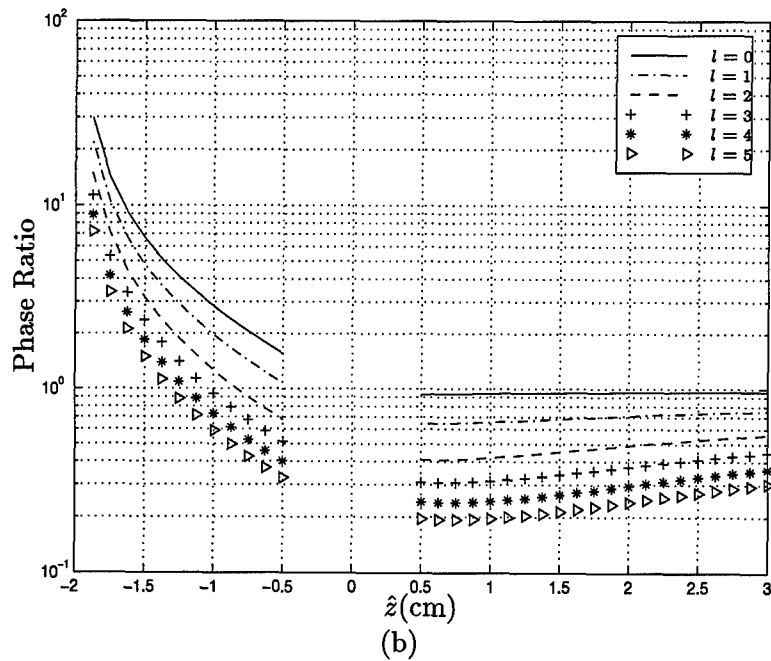
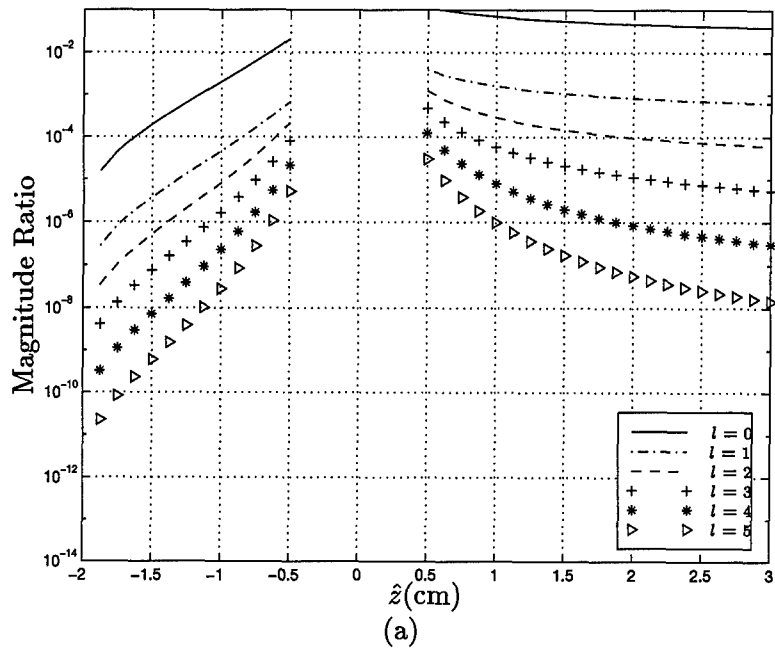


Figure 5.18 The first six moment (a) amplitude and (b) phase contributions of the scattered wave to the incident wave are plotted for high absorption and low scattering contrasts, along the  $\hat{z}$ -axis. For both figures,  $\mu_{a,out} = 0.05 \text{ cm}^{-1}$ ,  $\mu'_{s,out} = 10 \text{ cm}^{-1}$ ,  $\mu_{a,in} = 0.15 \text{ cm}^{-1}$ ,  $\mu'_{s,in} = 11 \text{ cm}^{-1}$ .

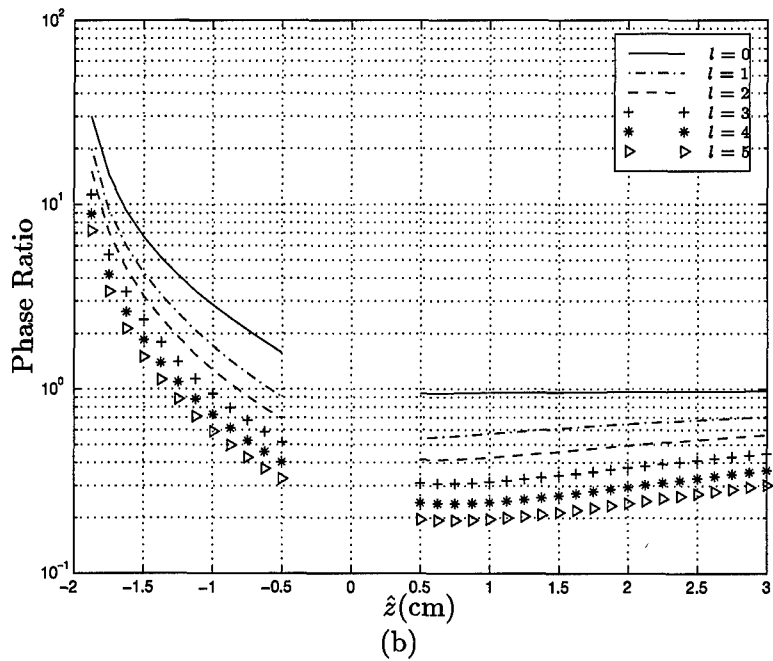
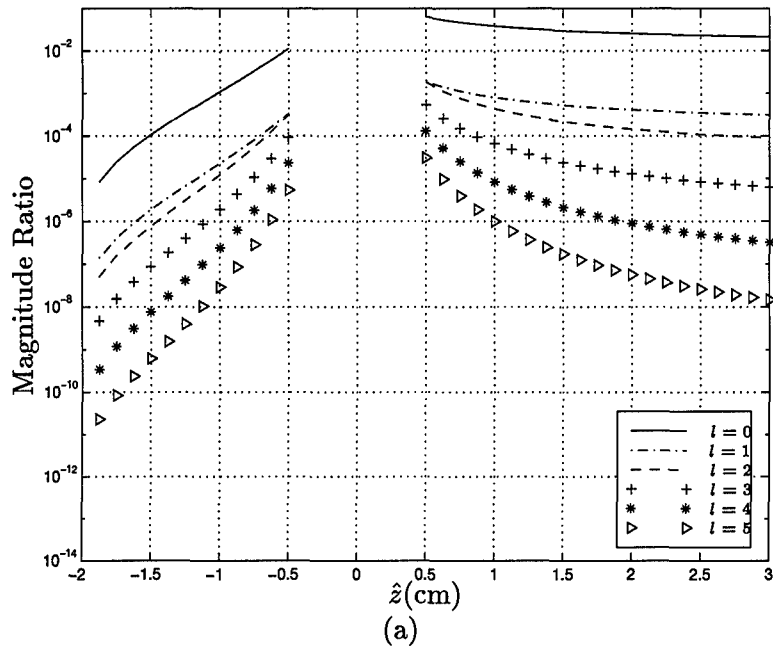


Figure 5.19 The first six moment (a) amplitude and (b) phase contributions of the scattered wave to the incident wave are plotted along the  $\hat{z}$ -axis. For both figures,  $\mu_{a,out} = 0.05 \text{ cm}^{-1}$ ,  $\mu'_{s,out} = 10 \text{ cm}^{-1}$ ,  $\mu_{a,in} = 0.10 \text{ cm}^{-1}$ ,  $\mu'_{s,in} = 11 \text{ cm}^{-1}$ .

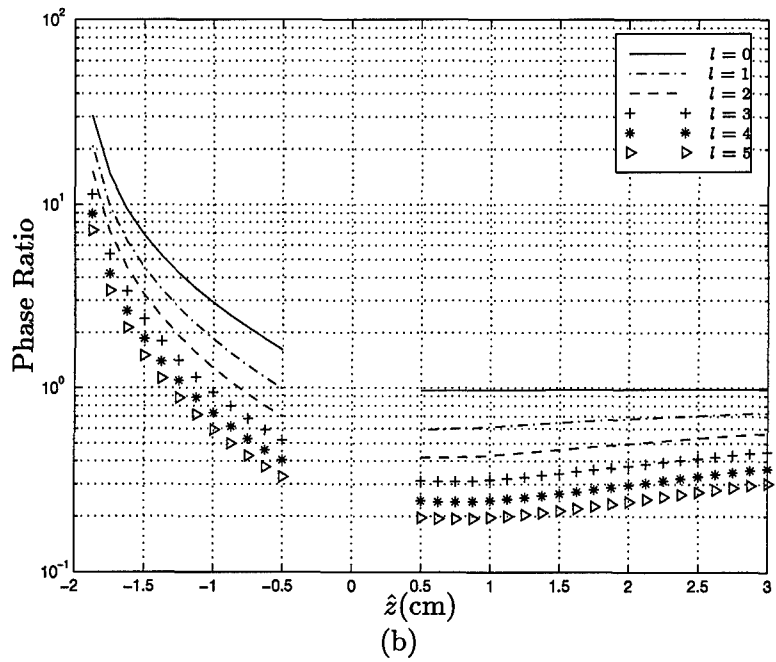
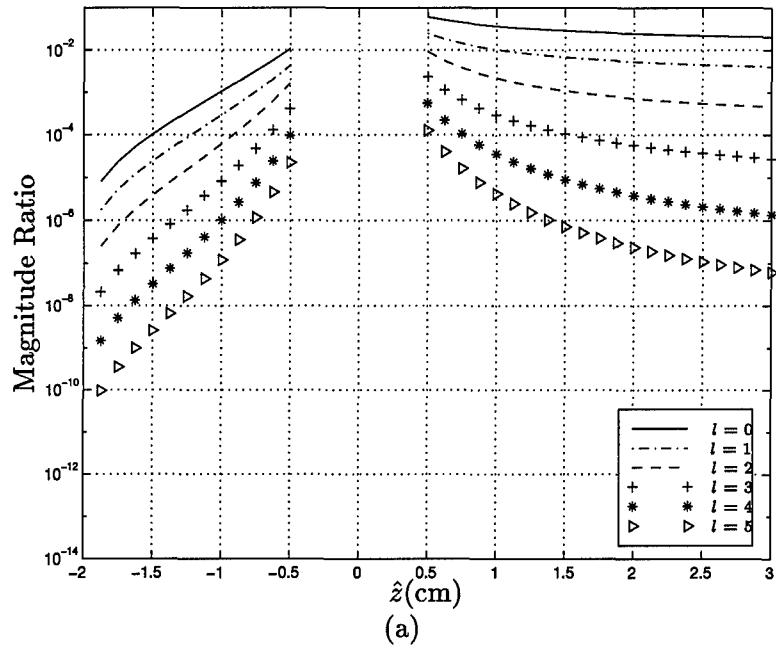


Figure 5.20 The first six moment (a) amplitude and (b) phase contributions of the scattered wave to the incident wave are plotted along the  $\hat{z}$ -axis. For both figures,  $\mu_{a,out} = 0.05 \text{ cm}^{-1}$ ,  $\mu'_{s,out} = 10 \text{ cm}^{-1}$ ,  $\mu_{a,in} = 0.10 \text{ cm}^{-1}$ ,  $\mu'_{s,in} = 15 \text{ cm}^{-1}$ .

### 5.5 *Fourier Optics Model Validity*

Though the transfer functions of the analytic approach (Chapter III) and the Fourier optics wave propagation method (Section 2.5) cannot be compared directly, their models of the effects on the incident (or homogeneous) wave due to the presence of a spherical inhomogeneity can be observed and compared. The models are simulated according to the codes developed in Section 4.8 and Section 4.9, respectively. The mean square error (MSE) is calculated in an  $\hat{x}$ - $\hat{y}$  slice for every 0.125 cm increment along the  $\hat{z}$ -axis per Equation (4.1). The coordinates corresponding to the inside of the inhomogeneity are not included in the MSE calculations since the analytic transfer function is not valid in that region. The resulting MSE of the magnitude and phase of the two approaches are plotted for various absorption and scattering parameters relative to the background medium.

The Fourier optics model was developed under the assumption that the wave propagation is through a homogeneous, source-free medium [32]. The inhomogeneity disrupts the homogeneous quality and subsequently acts as a secondary source within the medium. Thus this model is only valid in the regions not containing the inhomogeneity where the homogeneous and source-free conditions hold. If the inhomogeneity is modeled as a thin lens in the plane that contains its center, then the Fourier optics model for the incident wave is valid up to that plane. As the incident wave is transmitted through the plane containing the thin lens model of the sphere (Section 2.5.2), the incident wave is distorted. The resulting perturbed wave is then propagated through the medium using the Fourier optics model since the remaining medium is homogeneous and source-free.

As seen in Figures 5.21 through 5.28, the Fourier optics model is not without error. The perturbative effects from the inhomogeneity can only be included as the incident wave is propagated through the plane containing the inhomogeneity, unlike the analytic transfer model which can account for perturbations caused by the inhomogeneity throughout the entire medium. In a sense, there is no history in this forward propagation model as there is in the analytic transfer function model. Consequently, the degree of error between the two models increases as the wave propagates from the point source towards the plane containing the center of the inhomogeneity.

Modeling the spherical inhomogeneity as a thin lens that has straight ray propagation through it rather than some dissipative behavior, causes error in both the phase and the magnitude. Absorption in the sphere increases the amount of attenuation of the DPDW traveling through the sphere, while a more scattering medium in the inhomogeneity passes the rays unrefracted. The ray optics model does not account for the diffraction behavior. As the distorted wave propagates away from the plane containing the inhomogeneity center, the magnitude is attenuated, and the MSE between the two models will decrease. However, the error introduced in the phase does not attenuate and continues to propagate with the perturbed wave.

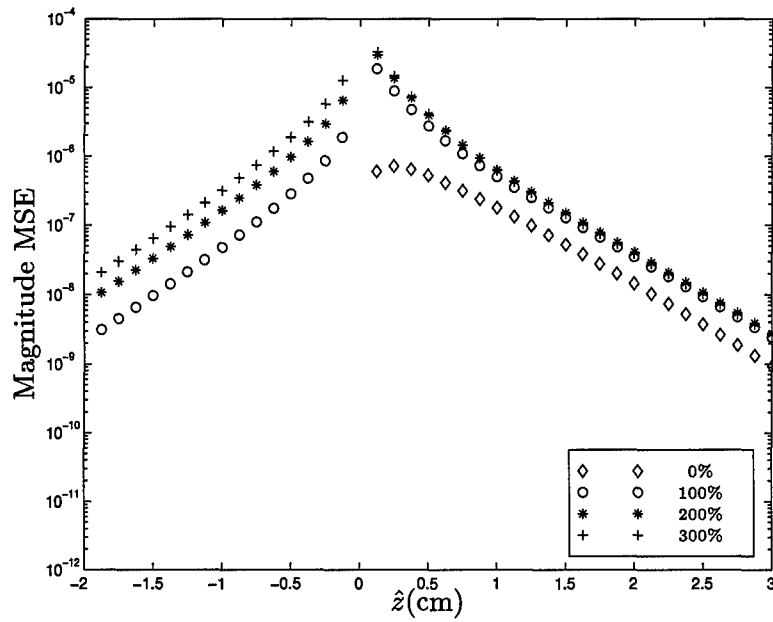
Figures 5.21 and 5.22 depict the MSE for cases involving a pure absorber and a pure scatterer, respectively. The error in both figures for the homogeneous wave up to the plane containing the center of the inhomogeneity ( $z=0$ ) is zero when there is no contrast present in either the absorption or the scattering properties. As the amount of contrast increases the amount of error in both the magnitude and phase increases. The relative error in the phase is affected more by an increase in absorption contrast than by an increase in scattering contrast. Beyond the plane containing the inhomogeneity center, the magnitude exponentially drops off as expected. However, the phase error caused by modeling the inhomogeneity in a plane is consistently carried through the remaining medium. A change in the absorption or scattering contrast does not significantly affect the phase error.

If a fixed absorption contrast is introduced into a pure scatterer case, the relative MSE for both the magnitude and the phase increases in the homogeneous wave from the source plane up to the plane containing the inhomogeneity center. The magnitude and phase MSE in the perturbed wave as it propagates through the remaining medium is largely unaffected beyond the boundary of the inhomogeneity. Variation in the scattering contrast does not significantly change either the magnitude error or the phase error in the entire system. Figures 5.23, 5.24, and 5.25 show the relative MSE for a 100%, 200%, and 300% fixed absorption contrast.

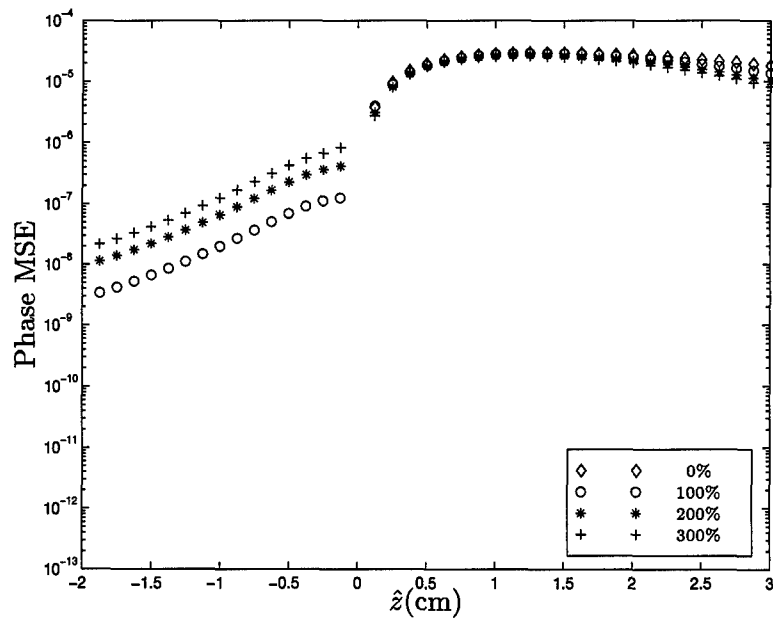
If a fixed amount of scattering contrast is added to a pure absorber case, the magnitude and phase MSE from the source plane up to the plane containing the inhomogeneity center is not affected except when no absorption contrast is present. As additional absorp-

tion contrast is introduced into the system as seen in Figures 5.26, 5.27, and 5.28, the MSE in the homogeneous wave propagation also increases. Phase error through the remaining medium, and magnitude error beyond the inhomogeneity boundary are not affected by variation in absorption contrast.

These MSE results demonstrate that the Fourier optics model is valid for the propagation of a spherical wave caused by a point source in a system containing an inhomogeneity with no optical contrast with the background medium. If the presence of an inhomogeneity causes a contrast, either in absorption or scattering, MSE in the magnitude of the model increases as the wave approaches the center location of the inhomogeneity and decreases exponentially as the wave propagates further away from the center. Additional absorption or scattering contrast causes a corresponding error in the magnitude MSE. Although the MSE in the phase of the model also increases up to the plane containing the center of the inhomogeneity, the phase error caused by modeling the inhomogeneity as a thin lens remains in the wave as it continues to propagate through the medium. The MSE of the phase is not affected by additional contrast in either absorption or scattering. Thus, the Fourier optics model is a valid approximation to the analytic transfer function when not near the inhomogeneity, and if the inhomogeneity has a little or no absorptive contrast with the surrounding turbid medium. The error incurred in the phase is mainly due to the model of the inhomogeneity as a spherical lens, and not an anomaly in the Fourier optics propagation model.

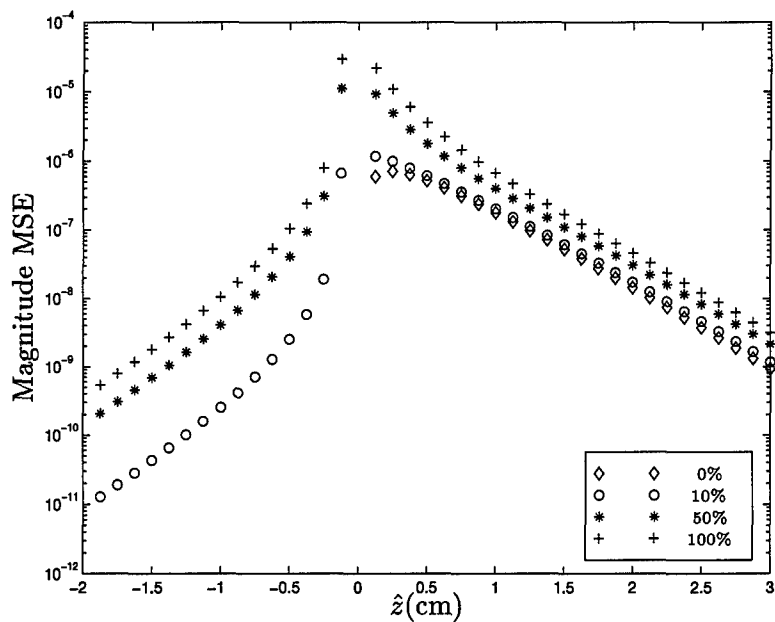


(a)

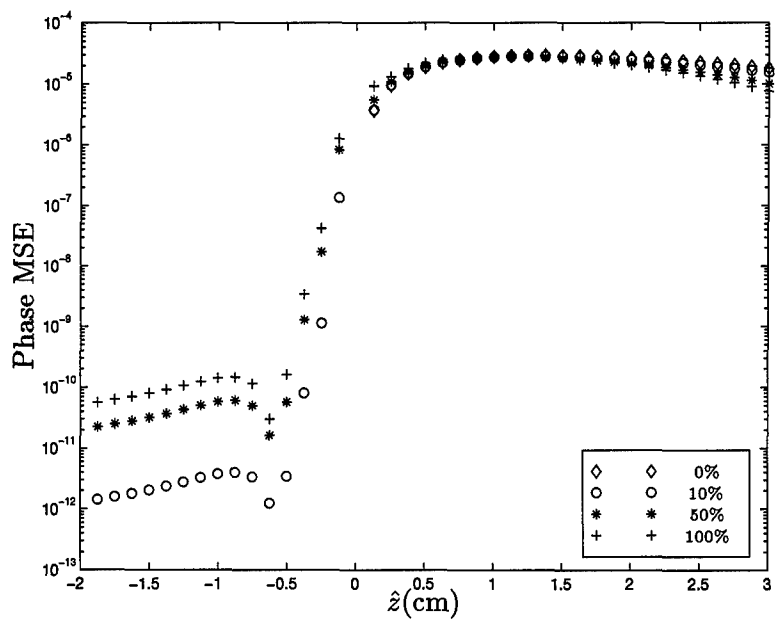


(b)

Figure 5.21 These plots show the mean square error in the (a) magnitudes and (b) phases (degrees) of the total waves for a pure absorber along the  $\hat{z}$ -axis calculated analytically and by means of the Fourier optics approximations. The object absorption coefficient is varied as:  $\mu_{a,in} = 0.05 \text{ cm}^{-1}$  ( $\diamond$ ),  $\mu_{a,in} = 0.10 \text{ cm}^{-1}$  ( $\circ$ ),  $\mu_{a,in} = 0.15 \text{ cm}^{-1}$  ( $*$ ), and  $\mu_{a,in} = 0.20 \text{ cm}^{-1}$  ( $+$ ). For both figures,  $\mu_{a,out} = 0.05 \text{ cm}^{-1}$ .

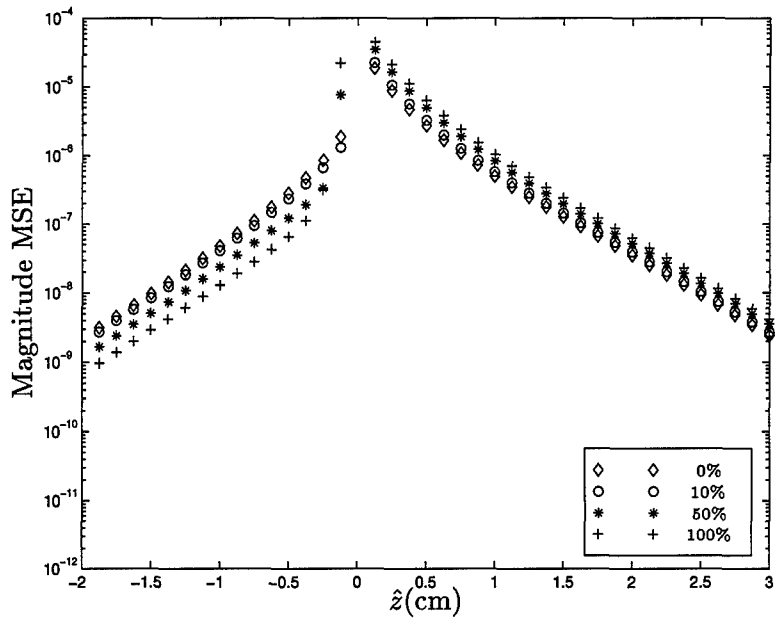


(a)

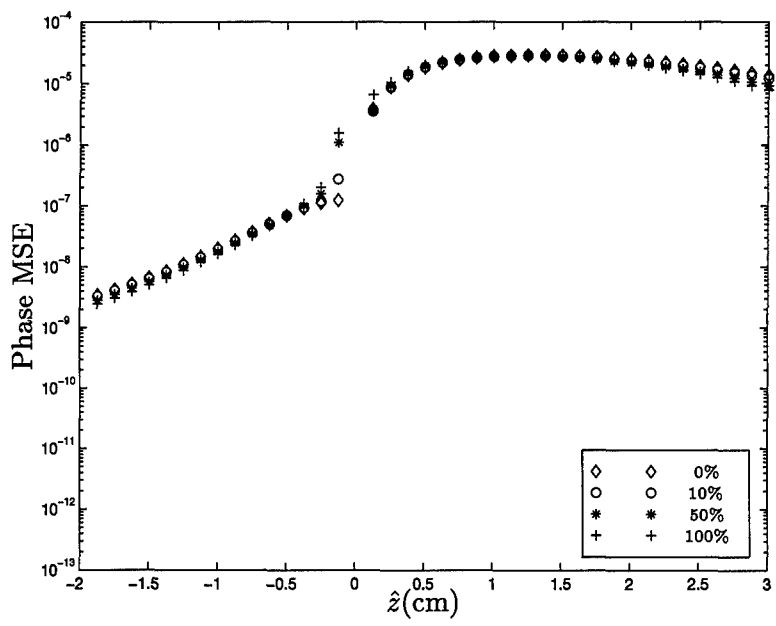


(b)

Figure 5.22 These plots show the mean square error in the (a) magnitudes and (b) phases (degrees) of the total waves for a pure scatterer along the  $\hat{z}$ -axis calculated analytically and by means of the Fourier optics approximations. The object scattering coefficient is varied as:  $\mu_{s,in} = 10 \text{ cm}^{-1}$  ( $\diamond$ ),  $\mu_{s,in} = 11 \text{ cm}^{-1}$  ( $\circ$ ),  $\mu_{s,in} = 15 \text{ cm}^{-1}$  (\*), and  $\mu_{s,in} = 20 \text{ cm}^{-1}$  (+). For both figures,  $\mu'_{s,out} = 10 \text{ cm}^{-1}$ .

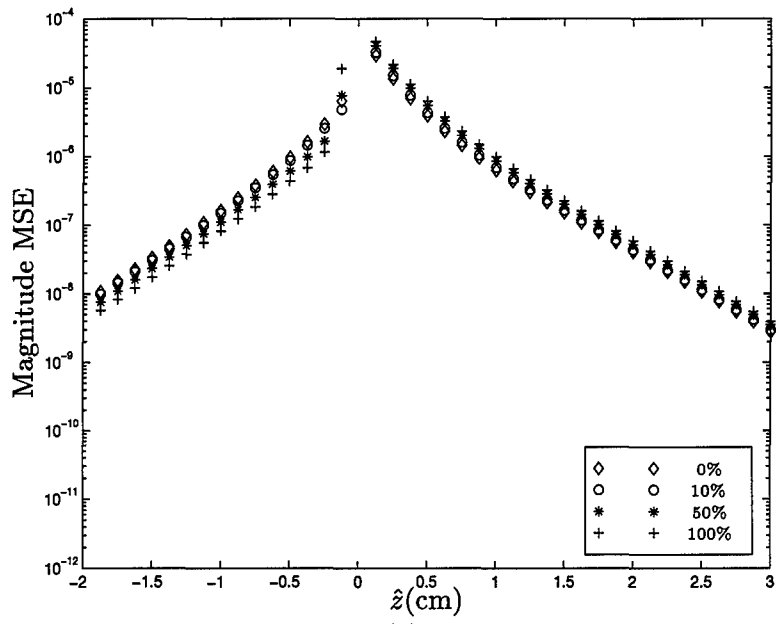


(a)

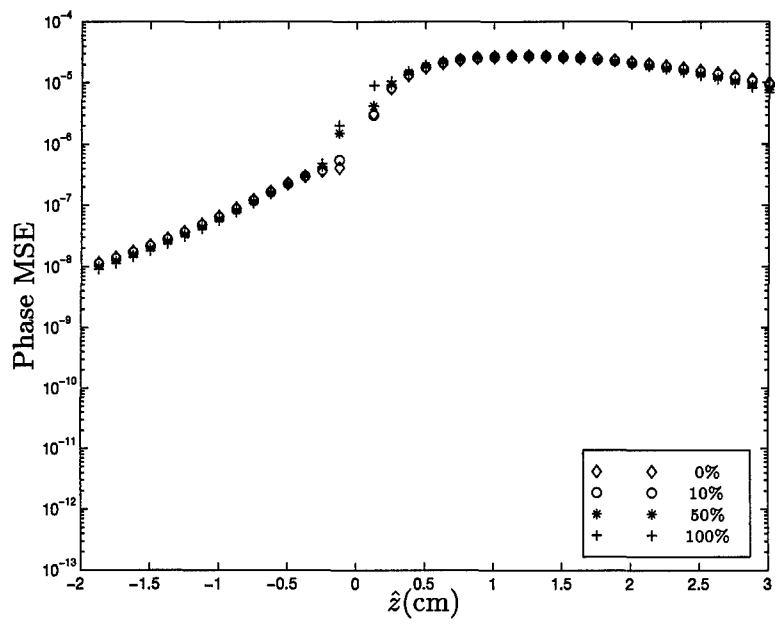


(b)

Figure 5.23 These plots show the mean square error in the (a) magnitudes and (b) phases (degrees) of the total waves for an inhomogeneity with low contrast in absorption along the  $\hat{z}$ -axis calculated analytically and by means of the Fourier optics model. The object scattering coefficient is varied as:  $\mu_{s,in} = 10 \text{ cm}^{-1}$  ( $\diamond$ ),  $\mu_{s,in} = 11 \text{ cm}^{-1}$  ( $\circ$ ),  $\mu_{s,in} = 15 \text{ cm}^{-1}$  (\*), and  $\mu_{s,in} = 20 \text{ cm}^{-1}$  (+). For both figures,  $\mu'_{a,in} = 0.10 \text{ cm}^{-1}$ ,  $\mu_{a,out} = 0.05 \text{ cm}^{-1}$ , and  $\mu'_{s,out} = 10 \text{ cm}^{-1}$ .

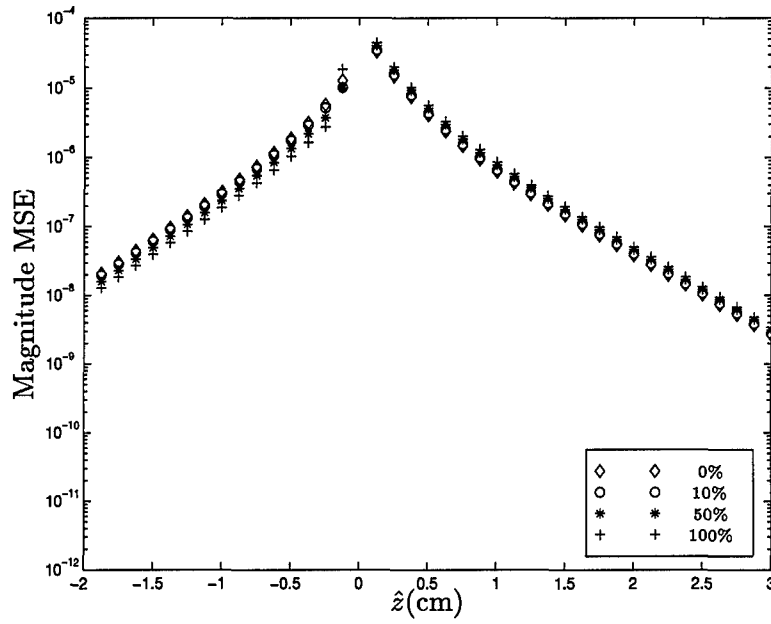


(a)

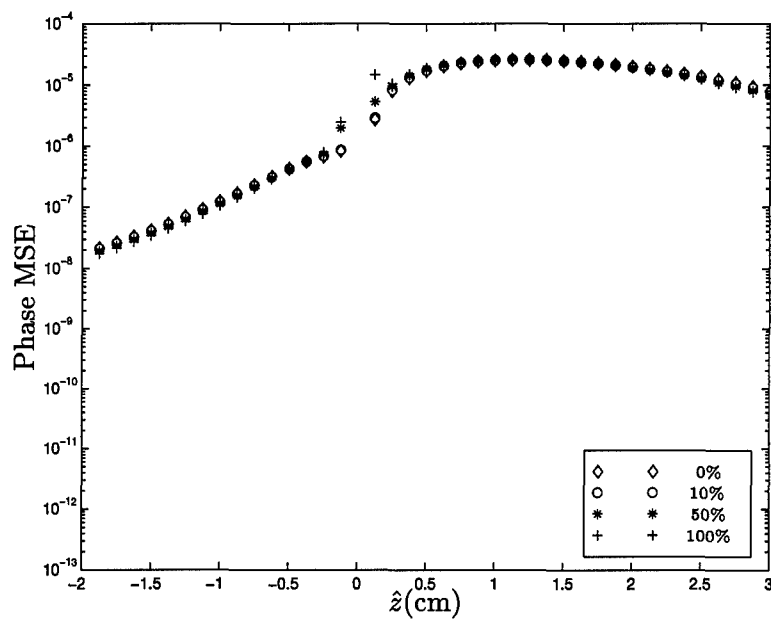


(b)

Figure 5.24 These plots show the mean square error in the (a) magnitudes and (b) phases (degrees) of the total waves for an inhomogeneity with high contrast in absorption along the  $\hat{z}$ -axis calculated analytically and by means of Fourier optics model. The object scattering coefficient is varied as:  $\mu_{s,in} = 10 \text{ cm}^{-1}$  ( $\diamond$ ),  $\mu_{s,in} = 11 \text{ cm}^{-1}$  ( $\circ$ ),  $\mu_{s,in} = 15 \text{ cm}^{-1}$  (\*), and  $\mu_{s,in} = 20 \text{ cm}^{-1}$  (+). For both figures,  $\mu'_{a,in} = 0.15 \text{ cm}^{-1}$ ,  $\mu_{a,out} = 0.05 \text{ cm}^{-1}$ , and  $\mu'_{s,out} = 10 \text{ cm}^{-1}$ .

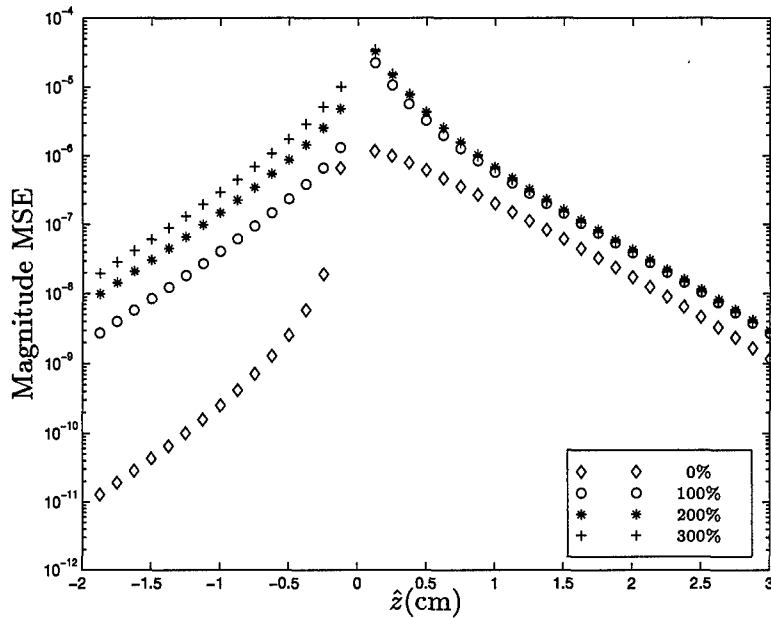


(a)

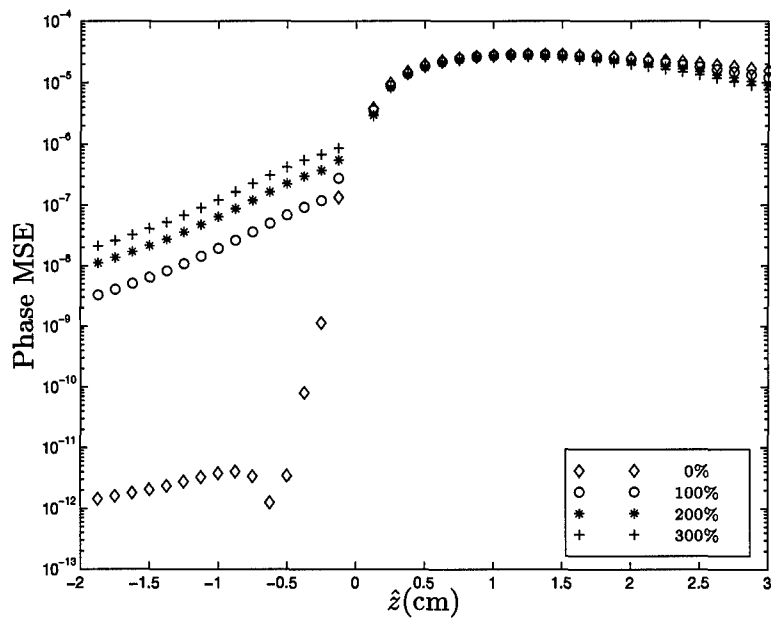


(b)

Figure 5.25 These plots show the mean square error in the (a) magnitudes and (b) phases (degrees) of the total waves for an inhomogeneity with very high contrast in absorption along the  $\hat{z}$ -axis calculated analytically and by means of Fourier optics model. The object scattering coefficient is varied as:  $\mu_{s,in} = 10 \text{ cm}^{-1}$  ( $\diamond$ ),  $\mu_{s,in} = 11 \text{ cm}^{-1}$  ( $\circ$ ),  $\mu_{s,in} = 15 \text{ cm}^{-1}$  (\*), and  $\mu_{s,in} = 20 \text{ cm}^{-1}$  (+). For both figures,  $\mu'_{a,in} = 0.20 \text{ cm}^{-1}$ ,  $\mu_{a,out} = 0.05 \text{ cm}^{-1}$ , and  $\mu'_{s,out} = 10 \text{ cm}^{-1}$ .

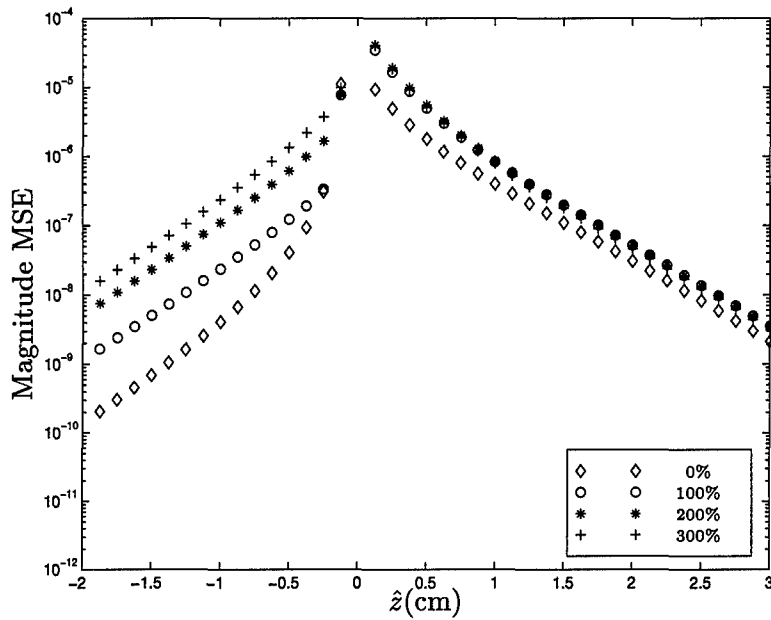


(a)

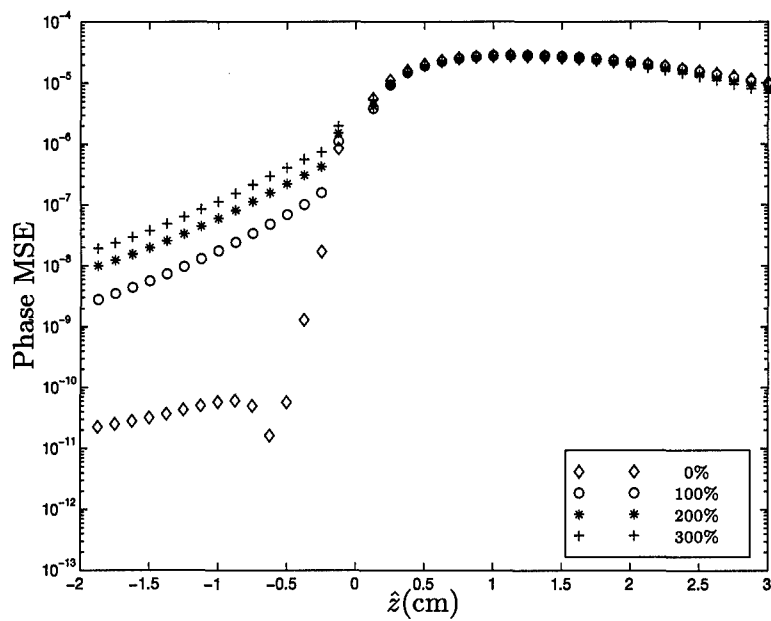


(b)

Figure 5.26 These plots show the mean square error in the (a) magnitudes and (b) phases (degrees) of the total waves for an inhomogeneity with low contrast in scattering along the  $\hat{z}$ -axis. The object absorption coefficient is varied as:  $\mu_{a,in} = 0.05 \text{ cm}^{-1}$  ( $\diamond$ ),  $\mu_{a,in} = 0.10 \text{ cm}^{-1}$  ( $\circ$ ),  $\mu_{a,in} = 0.15 \text{ cm}^{-1}$  (\*), and  $\mu_{a,in} = 0.20 \text{ cm}^{-1}$  (+). For both figures,  $\mu'_{s,in} = 11 \text{ cm}^{-1}$ ,  $\mu_{a,out} = 0.05 \text{ cm}^{-1}$ , and  $\mu'_{s,out} = 10 \text{ cm}^{-1}$ .

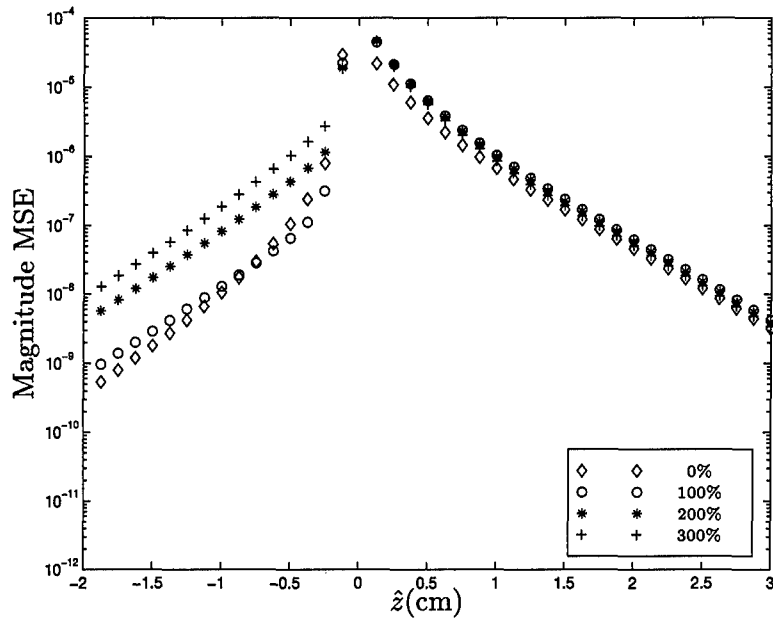


(a)

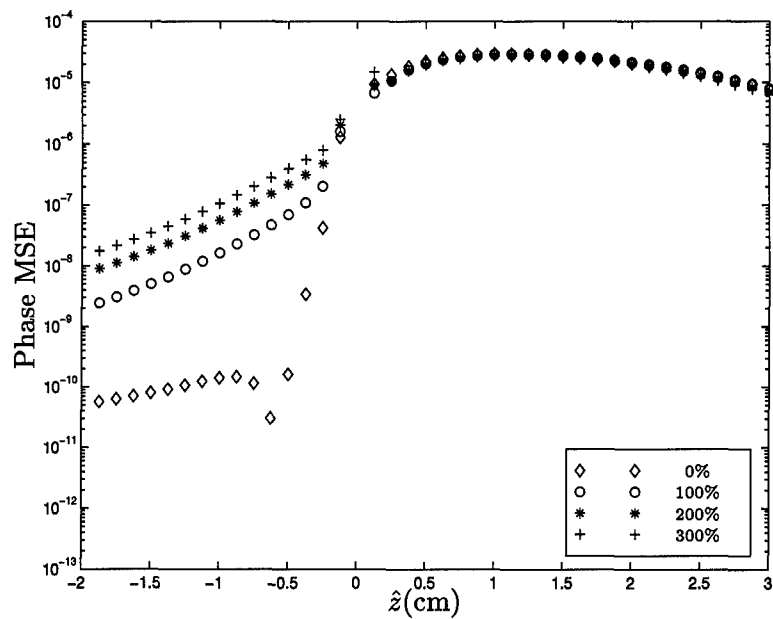


(b)

Figure 5.27 These plots show the mean square error in the (a) magnitudes and (b) phases (degrees) of the total waves for an inhomogeneity with high contrast in scattering along the  $\hat{z}$ -axis. The object absorption coefficient is varied as:  $\mu_{a,in} = 0.05 \text{ cm}^{-1}$  ( $\diamond$ ),  $\mu_{a,in} = 0.10 \text{ cm}^{-1}$  ( $\circ$ ),  $\mu_{a,in} = 0.15 \text{ cm}^{-1}$  ( $*$ ), and  $\mu_{a,in} = 0.20 \text{ cm}^{-1}$  ( $+$ ). For both figures,  $\mu'_{s,in} = 15 \text{ cm}^{-1}$ ,  $\mu_{a,out} = 0.05 \text{ cm}^{-1}$ , and  $\mu'_{s,out} = 10 \text{ cm}^{-1}$ .



(a)



(b)

Figure 5.28 These plots show the mean square error in the (a) magnitudes and (b) phases (degrees) of the total waves for an inhomogeneity with very high contrast in scattering along the  $\hat{z}$ -axis. The object absorption coefficient is varied as:  $\mu_{a,in} = 0.05 \text{ cm}^{-1}$  ( $\diamond$ ),  $\mu_{a,in} = 0.10 \text{ cm}^{-1}$  ( $\circ$ ),  $\mu_{a,in} = 0.15 \text{ cm}^{-1}$  (\*), and  $\mu_{a,in} = 0.20 \text{ cm}^{-1}$  (+). For both figures,  $\mu'_{s,in} = 20 \text{ cm}^{-1}$ ,  $\mu_{a,out} = 0.05 \text{ cm}^{-1}$ , and  $\mu'_{s,out} = 10 \text{ cm}^{-1}$ .

## 5.6 Summary

The amount of perturbation in the total wave due to the inhomogeneity depends on the contrast between the optical properties inside and outside the object. A sensitivity analysis for various combinations of contrasts showed that an object with a higher absorption coefficient relative to the background medium causes a decrease in the amplitude of the perturbed wave but does not significantly affect the phase. An inhomogeneity with a higher scattering parameter decreases the amplitude of the DPDW but causes a positive change in the phase. A combination of contrasts combine their effects, meaning that the reduction of the amplitude due to an increase in absorption is in addition to the reduction caused by a contrast in scattering properties. However, the absorption contrast does not contribute significantly to a distortion in the phase, particularly in the highly scattering cases. Ultimately, purely absorbing and scattering objects can be distinguished due to the type of change detected in the DPDW. An amplitude change indicates the presence of an absorber, while a phase change distinguishes a scatterer. However, when changes are detected in both amplitude and phase, absolute characterization is not possible without *a priori* knowledge of the object's optical properties.

The level of perturbation is dependent on the location of the detector plane to the inhomogeneity. In the simulations conducted in this research, the contrast causes the maximum change in the amplitude and phase to occur along the boundary of the inhomogeneity in the positive traveling direction of the wave. These maximum positions can be used to determine the depth of the object. As the diameter of the inhomogeneity decreases, the corresponding level of perturbation may be much less than what can be actually detected.

The number of moments required to characterize the scattered wave depends on the level and types of contrast present in the system. In the absence of any absorption contrast, the magnitude and phase perturbations are dominated by the second (dipole) and third (quadrupole) moments of the scattered wave. Depending on the location of the detector plane, the fourth and fifth moments may contribute more than the monopole. If an absorption contrast is introduced into the system, the first moment, or the monopole, becomes the major contributor to both the magnitude and phase perturbations.

The valid regions of the Fourier optics model of a spherical inhomogeneity in an otherwise piece-wise homogeneous medium were determined by comparing the total wave perturbations to those calculated by the analytic transfer function model. The homogeneous wave is best modeled by the Fourier optics model when there is no absorption contrast present in the system. When there is an absorption or a scattering contrast present, the approximate error in the homogeneous wave model increases up to the plane containing the center of the inhomogeneity. From that plane to the boundary of the system, the magnitude error exponentially decreases, making the wave propagation model a more accurate model as the detection plane moves away from the inhomogeneity. However, since the ray optics model requires the spherical inhomogeneity to be modeled in a plane, a phase error is incurred. The wave propagation transfer function continues to propagate this error, but does not appear to incur any additional phase error. Effectively, the Fourier optics model is a relatively good approximation to the analytic transfer function method when not near the inhomogeneity and if the inhomogeneity has a strong scattering and low absorption behavior. Otherwise, the model of the spherical inhomogeneity as a thin lens is not an accurate one.

## VI. Summary

### 6.1 Conclusions

Diffusive light can be used to detect and localize optical inhomogeneities embedded in thick, turbid media such as human breast tissue. In this thesis, a transfer function was derived from an exact analytic solution which can completely characterize the perturbations in the forward propagation phenomena caused by a spherical inhomogeneity in a multiple-scattering medium.

The diffusion approximation to the linear transport theory yields a wave solution when the intensity of a point source of light is sinusoidally modulated. This wave solution is a highly damped, spherically outgoing scalar intensity wave which has a complex wavenumber. The wave is referred to as a diffuse photon density wave (DPDW) and exhibits classic wave behavior.

Several models have been presented to describe the forward propagation of DPDWs through an infinite, homogeneous, turbid medium which contains an embedded spherical inhomogeneity. Based on the knowledge of scattering of diffuse photon density waves, an analytic solution is derived from the diffusion approximation. This solution is an exact model for the perturbations in the DPDW caused by the inhomogeneity. Another model uses Fourier optics theory to propagate the DPDW through the homogeneous turbid medium. This model assumes ray optic transmission through the inhomogeneity, and thus the model represents the inhomogeneity as a spherical lens in a plane. The DPDW is perturbed by the lens model and is then propagated through the remaining homogeneous medium by a simple plane wave transfer function. This lens model is an approximation to the perturbations in the DPDW since the ray optic assumption is not valid when the inhomogeneity exhibits some absorptive property.

To improve the Fourier optics model, a transfer function was derived to model exactly the perturbations caused by a spherical inhomogeneity in a plane wave structure. This function completely characterizes the sensitivity of the system to detect and localize in three-dimensions inhomogeneities of varying optical contrasts with the surrounding medium. Through simulations, the sensitivity analysis showed that a presence of low

absorptive and scattering optical contrasts can combine to perturb the incident DPDW to a detectable level. The location of the perturbation can then be used to isolate the inhomogeneity.

## *6.2 Recommendations for Future Research*

The sensitivity analysis results demonstrated the remarkable use of perturbative behavior due to optical contrast as a means to not only detect but locate in three dimensions a spherical inhomogeneity. However, these simulation results are not complete without a rigorous noise analysis. The limitations of detectors are ultimately dependent on the signal-to-noise ratios (SNR) in the system. Previous SNR studies have been conducted in systems that required movement in both the source and detector. The main source of error was found to be the source-detector alignment [13]. With the advent of the exact transfer function expression in the Fourier optics approach (which does not require source-detector movement), the positional error is removed from the system. Consequently, the Fourier optics approach has the potential to achieve higher resolution in both detection and localization.

Perturbations in the DPDW have been shown to be dependent on the level of optical contrast present as well as the inhomogeneity size. Another parameter that has a perturbative effect and should be investigated is the source modulation frequency, particularly in the presence of low optical contrasts. The analysis of the frequency effects may also be tied to the SNR analysis mentioned above.

In either the SNR or the frequency analysis, the conclusions drawn from simulations should be verified against experimental data. Initial experiments were conducted by Liu to verify the theoretical simulations [38]. However, the SNR and frequency analysis can be used to improve the experimental set-up to achieve higher accuracy.

Optical characterization continues to be an elusive process [13, 18]. Once a tumor is detected, the type of tumor becomes the important factor. Knowledge of optical contrasts may be used to characterize detected tumors. Low optical contrast was selected as the concentration in this thesis in anticipation of application to a diffraction tomo-

graphic model that is currently under development [39]. The analytic transfer function developed in Chapter III can be directly applied to the diffraction tomographic model for qualitative reconstruction of optical property imaging. Both theoretical validation as well as experimental verification of the diffraction model using the transfer function should be pursued.

### 6.3 Closing

The focus of this research has been on using DPDW imaging for low resolution breast tumor screening. This approach to *in vivo* imaging is particularly promising since the procedure is inexpensive and has no known adverse side effects, the noise associated with movement of the testing apparatus is negligible, and the measurements can be evaluated in a real-time environment. Currently, industrial research groups are performing clinical evaluations of optical mammography systems [24]. Hopefully the results of this thesis as well as other on-going research continues to generate interest and support in the continued development in this and other clinical applications.

## Appendix A. Input Parameter Code Listing to the Analytic Solution

This Appendix contains the source code list for the input parameters to the Analytic Solution code.

---

```

% Capt Debbie Lasocki
%
% file: Master.m
%
% Purpose: Input parameters
%
file_name = 'Master';

% Constants
Sac = 1;          % Source modulation amplitude
a = 0.5;         % Radius of inhomogeneity (cm)
f = 20E6;        % Modulation freq. (Hz)
numdeg = 20;     % Truncate series after this number of terms
cutoff = 0.5;    % Cutoff frequency in filtering frequency domain data

% Geometry of Source and location of Detector plane (cm)
% relative to the center of the inhomogeneity (0,0,0)

rsx = 0;         % Location of the source along x-axis
rsy = 0;         % Location of the source along y-axis
rsz = -2;        % Location of the source along z-axis
zdet = 3;        % Location of detector plane

% Define the region of interest and the increments of resolution in
% units of centimeters. Do not include origin in the sampling.

inc = 0.1;
idim = 5.0;
zinc = 0.125;
x = [-idim/2:inc:idim/2];
y = [-idim/2:inc:idim/2];
z = [rsz+zinc:zinc:-zinc zinc:zinc:zdet];

xplot = ceil(length(x)/2); % y-plane at which to view x-z slice (pixel)
yplot = ceil(length(y)/2); % y-plane at which to view x-z slice (pixel)
zplot = length(z);         % z-plane at which to view x-y slice (pixel)

% Parameters outside of the inhomogeneity
Muaout = 0.05;           % absorption coeff (cm^-1)
Musout = 10;             % red. scattering coeff (cm^-1)
Nout = 1.333;            % index of refraction
Vout = 2.98E10/Nout;     % speed of light without medium
Dout = Vout / (3*(Musout+Muaout)); % Diffusion coeff
Kout = sqrt((-Vout*Muaout + 2*pi*f*j)/Dout); % wavenumber

% Parameters inside of the inhomogeneity
Muain = 0.15;           % absorption coeff (cm^-1)
Musin = 12;             % red. scattering coeff (cm^-1)
Nin = 1.333;            % index of refraction
Vin = 2.98E10/Nin;     % speed of light within medium
Din = Vin / (3*(Musin+Muain)); % Diffusion coeff
Kin = sqrt((-Vin*Muain + 2*pi*f*j)/Din); % wavenumber

```

---

## Appendix B. Analytic Solution Code Listing

This Appendix contains the source code list for the Analytic Solution.

---

```

function [Uinc,Uscatt,Us,Uout,UoutH,H] = trx(numdeg, ...
    Sac, ...
    a, ...
    rsx, rsy, rsz, ...
    x, y, z, ...
    Dout, ...
    Vout, ...
    Kout, ...
    Din, ...
    Kin ...
);
10

% Capt Debbie Lasocki
%
% file: trx.m
%
% Purpose: To examine the Scattered wave as derived from an analytic solution
%
% It is assumed that the incident wave is generated by a point source and
% the detector is in a plane on the opposite side of the inhomogeneity than
% the source. Further, the inhomogeneity is set at the origin of this
% coordinate system, and all distances are measured relative to that point.
20

% This can be set up to calculate the wave at various z-planes, but the
% planes of interest here are already calculated meaning that at the
% inhomogeneity center and at the detector plane, the wave values are already
% computed.

% Calculate dimensions
30

lx = length(x);
ly = length(y);
lz = length(z);

% Determine the Incident Wave

% The incident wave is generated by a point source in the homogeneous medium,
% but outside the region of interest so singularities are avoided.

% Pre-calculate the x-y-z distances in spherical coordinates about the
% source coordinate
40
[xp,yp,zp] = ndgrid(x,y,z);
R = sqrt((xp-rsx).^2 + (yp-rsy).^2 + (zp-rsz).^2);
Uinc = Vout*Sac./(4*pi*Dout.*R) .* exp(j*Kout.*R);

% A(l,0) coefficients defined
for l=0:numdeg-1
    term1(l+1) = -j*Sac*Kout*sbesselh(1,1,Kout*abs(rsz))...
        *sqrt((2*l+1)/(2*pi))*conj(ymn('e',0,1,pi,0));
50

    term2(l+1) = Dout.*Kout.*a.*Dsbesselj(1,Kout.*a).*sbesselj(1,Kin.*a)...
        - Din.*Kin.*a.*sbesselj(1,Kout.*a).*Dsbesselj(1,Kin.*a);

    term3(l+1) = Dout.*Kout.*a.*Dsbesselh(1,1,Kout.*a).*sbesselj(1,Kin.*a)...
        - Din.*Kin.*a.*sbesselh(1,1,Kout.*a).*Dsbesselj(1,Kin.*a);
end;
Alm = term1 .* term2./term3;

% Define scattered wave in the region of interest.
% Pre-calculate the x-y-z distances in spherical coordinates about the
% detector plane wrt to the origin of the inhomogeneity
60

R = sqrt(xp.^2 + yp.^2 + zp.^2);

```

```

for l=0:numdeg-1;           % For each moment
for xp = 1:lx              % For each x-point
for yp = 1:ly              % For each y-point
for zp = 1:lz              % For each z-point

    if R(xp,yp,zp) ~ = 0
        Theta = acos(z(zp)./R(xp,yp,zp));
    else
        Theta = 0;
    end;
    if x(xp) ~ = 0
        Phi = atan(y(yp)./x(xp));
    else
        Phi = pi/2;
    end;
    Uscatt(xp,yp,zp,l+1) = Alm(l+1) ...
        * sbesselh(1,1,Kout*R(xp,yp,zp)) ...
        * sqrt((2*l+1)/(2*pi))*ymn('e',0,l,Theta,Phi);
end;
end;
end;
end;

Us = sum(Uscatt,4);        % Sum over the moments

% Output wave is just the superposition of the incident and the
% scattered wave
Uout = Uinc + Us;

```

### Appendix C. Transfer Function Code Listing to the Analytic Solution

This Appendix contains the source code list for the transfer function to the Analytic Solution code. The first code is the main program which calls a transfer function calculation which is listed in the second code.

---

```

function [Uinc,Uscatt,H,UoutH] = fth(numdeg, ...
    Sac, ...
    a, ...
    rsx, rsy, rsz, ...
    x, y, z, ...
    Dout, ...
    Vout, ...
    Kout, ...
    Din, ...
    Kin ...
);
10

% Capt Debbie Lasocki
%
% file: fth.m
%
% Purpose: To examine the Scattered wave as
%           determined by a transfer function
%           derived from an analytic solution
%
% It is assumed that the incident wave is generated by a point source and
% the detector is in a plane on the opposite side of the inhomogeneity than
% the source. Further, the inhomogeneity is set at the origin of this
% coordinate system, and all distances are measured relative to that point.
%
% This can be set up to calculate the wave at various z-planes, but the
% planes of interest here are already calculated meaning that at the
% inhomogeneity center and at the detector plane, the wave values are already
% computed.
%
20
% Calculate dimensions
lx = length(x);
ly = length(y);
lz = length(z);

xcent = ceil(lx/2);      % center of x-plane (pixel)
ycent = ceil(ly/2);     % center of y-plane (pixel)
40

% Determine the Incident Wave

% The incident wave is generated by a point source in the homogeneous medium,
% but outside the region of interest so singularities are avoided.

% Pre-calculate the x-y-z distances in spherical coordinates
% about the source coordinate
[xp,yp,zp] = ndgrid(x,y,z);
R = sqrt((xp-rsx).^2 + (yp-rsy).^2 + (zp-rsz).^2);
Uinc = Vout*Sac./(4*pi*Dout.*R) .* exp(j*Kout.*R);
50

% A(l,0) coefficients defined
for l=0:numdeg-1
    term1(l+1) = -j*Sac*Kout*sbesselh(1,1,Kout*abs(rsz))...
        *sqrt((2*l+1)/(2*pi))*conj(ymn('e',0,l,pi,0));

    term2(l+1) = Dout.*Kout.*a.*Dbesselj(1,Kout.*a).*sbesselj(1,Kin.*a)...
        - Din.*Kin.*a.*sbesselj(1,Kout.*a).*Dbesselj(1,Kin.*a);

    term3(l+1) = Dout.*Kout.*a.*Dbesselh(1,1,Kout.*a).*sbesselj(1,Kin.*a)...
60

```

```

        - Din.*Kin.*a.*sbesselh(1,1,Kout.*a).*Dbesselj(1,Kin.*a);
end;
Alm = term1 .* term2./term3;

% Determine the scattered wave in the region of interest

% Pre-calculate the x-y-z distances in spherical coordinates about the
% detector plane wrt to the origin of the inhomogeneity

R = sqrt(xp.^2 + yp.^2 + zp.^2);
% For each moment
% For each x-point
% For each y-point
% For each z-point
for l=0:numdeg-1;
for xp = 1:lx
for yp = 1:ly
for zp = 1:lz
    if R(xp,yp,zp) ~= 0
        Theta = acos(zp./R(xp,yp,zp));
    else
        Theta = 0;
    end;
    if x(xp) ~= 0
        Phi = atan(yp./x(xp));
    else
        Phi = pi/2;
    end;
    Uscatt(xp,yp,zp,l+1) = Alm(l+1) ...
        * sbesselh(1,1,Kout*R(xp,yp,zp)) ...
        * sqrt((2*l+1)/(2*pi))*ymn('e',0,l,Theta,Phi);
end;
end;
end;
end;
Us = sum(Uscatt,4); % Sum over the moments

% Determine Transfer function

% Zero pad up to automatically-defined fftpts size to avoid wrap-around and
% fftshift problems on an odd-sized array (in x-y direction).

% The center of the medium must be shifted to the upper left-hand corner of
% the array in order to use the fft command properly in MATLAB. A second
% shift is done to return the array to the proper ordering and the original
% data size is extracted out of the center of the array.

fftpts = 2^ceil(log2(lx)); % Assumes x-axis is longest
tinc = zeros(fftpts,fftpts,lz); % initialize temp array
ts = zeros(fftpts,fftpts,lz); % initialize temp array
fftcent = fftpts/2 + 1; % Center of fft matrix
xi = -xcent+1:xcent-1; % midrange array indices x-axis
yi = -ycent+1:ycent-1; % midrange array indices y-axis

tinc(fftcent+xi, fftcent+yi,1:lz) = Uinc(:,:);
ts(fftcent+xi, fftcent+yi,1:lz) = Us(:,:);

for n = 1:lz;
    UincFT(:,:,n) = fftshift(iff2(fftshift(tinc(:,:,n))));
    UscattFT(:,:,n) = fftshift(iff2(fftshift(ts(:,:,n))));
end;

% A matrix of the same size of the fft arrays is created in order to
% correctly add 1 to each pixel.

unity = ones(fftpts,fftpts,lz);
H = unity + UscattFT./UincFT;

% Determine Output wave from Transfer function

```

```
% The shift is done to correctly order the array for fft.  
% The second shift is done at plotting the results to extract  
% desired original data (slice) from the results of the transform.
```

```
for n=1:lz  
    UH(:,n) = fftshift(fft2(fftshift(UincFT(:,n).*H(:,n))));  
end;  
UoutH = zeros(lx,ly,lz);  
UoutH = UH(fftcent+xi, fftcent+yi,:);
```

---

## Appendix D. Fourier Optics Wave Propagation Code Listing

This Appendix contains the source code list for the Fourier optics wave propagation model [41] using Goodman's methods. The first code is the main program which calls a transfer function calculation which is listed in the second code.

---

```

function [homo,Udet] = goodman( Sac, ...
                               a, ...
                               rsx, rsy, rsz, ...
                               inc, ...
                               idim, ...
                               zinc, ...
                               x, y, z, ...
                               Dout, ...
                               Vout, ...
                               Kout, ...
                               Kin ...
                               );

% Capt Debbie Lasocki
%
% file: goodman.m
%
% Purpose: To propagate a spherical wave through an otherwise
%          piece-wise homogeneous media containing a spherical object
%          using plane wave propagation methods developed by Goodman.
%
% This program was ported to MATLAB 5.0 from IDL code developed by
% Dr. Chuck Matson.
%
% This program calculates an incident wave through a homogeneous media.
% It also calculates the wave through the homogeneous media up to the
% center of an inhomogeneity via Goodman's approach. The wave is then
% transmitted through the media using conventional techniques. This
% perturbed wave is then propagated to the detector plane using Goodman's
% approach once again.
%
% The wave is centered on the x-y axis and symmetric around the z-axis.
% The resolution of propagation along each axis is determined by the user.
% The size of the sample, the location of the source, the location of the
% inhomogeneity, and the optical parameters of the inhomogeneity are also
% specified by the user.
%
% Calculate dimensions
ic = idim/2;           % Center of sample (cm)
flr = 1E-10;         % Establish floor value
lx = length(x);      % length of x-axis (pixels)
ly = length(y);      % length of y-axis (pixels)
lz = length(z);      % length of z-axis (pixels)
lzsph = find(z==0);  % center of sphere along z-axis (pixels)
                    % assuming source pixel is included in z
%
% Size of FFT matrix should be set > # pixels in sample
fftpts = 2^ceil(log2(lx)); % Assumes x-axis is longest
%
% Pre-calculate the x-y-z distances in spherical coordinates about the
% source coordinate
[X Y Z] = ndgrid(x,y,z);
XY2 = (X-rsx).^2 + (Y-rsy).^2;
R = sqrt(XY2 + (Z-rsz).^2);
%
% Generate incident wave in the detection plane

```

```

homo = Sac*Vout./(4*pi*Dout.*R).*exp(j*Kout.*R);
size(homo)

% Propagate source wave to the plane containing center of inhomogeneity
% which also corresponds to the origin of the system
% This creates a separate incident wave then the one above (homo).
% The field is generated at each z-plane increment up to the center
% of the inhomogeneity along the z-axis
Uhomo = Sac*Vout./(4*pi*Dout.*R(:,1:lzsph)).*exp(j*Kout.*R(:,1:lzsph));
70

% Create the complex transmittance caused by the sphere
% All other points outside the sphere are transmitted unperturbed

% Determine location of center of sphere in pixels
icenx = ceil(lx/2);
iceny = ceil(ly/2);

if rem(icenx,2) == 0
    ix = icenx;
else
    ix = floor(icenx);
end;
if rem(iceny,2) == 0
    iy = iceny;
else
    iy = floor(iceny);
end;

trans = ones(lx);           % Initialize complex transmittance array
90

for m = -a/inc:a/inc       % Index array for diameter of sphere in pixels
    for n = -a/inc:a/inc
        if a^2 >= XY2(ix+m,iy+n)      % Is point inside sphere?
            thick = 2.*sqrt(a^2-XY2(ix+m,iy+n)); % Distance through sphere
            amp = exp(-thick*imag(Kin-Kout)); % Adjust amplitude
            phase = thick*(Kin-Kout); % Adjust phase
            trans(ix+m,iy+n) = amp*exp(j*phase); % Calculate transmittance
        end;
    end;
end;
100

% Create perturbed wave in same plane, just after going through equivalent
% sphere transmittance as created above (so plane location is at the center
% of the inhomogeneity still)

Uper=Uhomo;
Uper(:,1:lzsph) = Uhomo(:,1:lzsph).*trans;

% Propagate inhomogeneous wave to detection plane now using Goodman's
% Fourier optics propagation approach
110

% Zero pad perturbed wave to avoid wrap-around errors and quadrant swapping
% errors during Fourier transform process
Uperz = zeros(fftpts,fftpts,lzsph);
UPERZ = zeros(fftpts,fftpts,lzsph);
fftcent = fftpts/2 +1;           % Center of fft matrix
xi = -icenx+1:icenx-1;          % midrange array indices x-axis
yi = -iceny+1:iceny-1;          % midrange array indices y-axis
Uperz(fftcent+xi, fftcent+yi,1:lzsph) = Uper(:,,:);
120

for n = 1:lzsph
    % Fourier transform perturbed wave
    UPERZ(:,n) = fftshift(fft2(fftshift(Uperz(:,n))));
end;

% Initialize arrays
H = ones(fftpts, fftpts, lz);

```

```

UH = zeros(fftpoints, fftpoints, lz);
UH(:,:,1:lzspth) = UPERZ(:,:,:);
uh = zeros(fftpoints, fftpoints, lz);
% Pre-calculate transfer function
Htemp = transfer(fftpoints, zprop, inc, Kout, flr);
for n=lzspth+1:lz;
    % Move wave via transfer function
    H(:,:,n) = H(:,:,n-1).*Htemp;
    UH(:,:,n) = UH(:,:,n-1).*H(:,:,n);
end;
for n = 1:lz
    % Inverse Fourier transform to get inhomogeneous wave
    uh(:,:,n) = fftshift(iff2(fftshift(UH(:,:,n))));
end;
Udet = zeros(lx,ly,lz);
Udet = uh(fftcent+xi,fftcent+yi,:); % Extract original size of wave array

```

---

```

function [H] = transfer(fftpoints, zprop, scale, k, floorratio);
% This function creates a (Matson) transfer function for wave propagation.
% fftpoints is the size of the array, zprop is the distance to propagate between
% orthogonal planes, scale is the distance per pixel in the image plane,
% and k is the wave number (complex), and the floorratio is the lower
% limit for values to keep within the precision of MATLAB 5.0.
%
% fftpoints : size of array
% zprop : plane of interest distance
% scale : x-y increments in image plane
% k : complex wavenumber
% floorratio : bottom limit of transfer function
ic = fftpoints/2 + 1; % Center of array
% Note that this is one-pixel short of the
% center of the fftpoints array
% Results in H are centered on the fftpoints
% array as it should be
H = zeros(fftpoints); % Initialize array
fscale = 2*pi/(fftpoints*scale);
m = 1:fftpoints; n = 1:fftpoints;
[M N] = meshgrid(m,n);
r = j*zprop*sqrt(k.^2 - (fscale*(ic-M)).^2 - (fscale*(ic-N)).^2);
rmag = abs(r);
rphasor = r./rmag;
r = rmag.*rphasor;
H = exp(r);
H = H+floorratio * max(max(H))*ones(size(H));

```

### Bibliography

1. Abramowitz, M. and I. Stegun. *Handbook of Mathematical Functions*. New York: Dover Publications, 1965.
2. Anderson, R. R. and J. A. Parish. "The Optics of Human Skin," *Journal of Investigative Dermatology*, *77*:13-19 (1981).
3. Aronson, R. "Boundary conditions for diffusion of light," *J. Opt. Soc. Am. A*, *12*:2532-2539 (November 1995).
4. Arridge, S. R. "Photon-measurement density functions. Part 1. Analytical forms," *Appl. Opt.*, *34*:7395-7409 (November 1995).
5. Baños, A. *Dipole Radiation in the Presence of a Conducting Half-Space*. Oxford: Pergamon Press, 1966.
6. Beahrs, O.H., et al. "Report of the Working Group to Review the National Cancer Institute-American Cancer Society Breast Cancer Detection Projects," *Journal of the National Cancer Institute*, *62*:641-709 (1993).
7. Bell, W. W. *Special Functions for Scientists and Engineers*. New Jersey: Van Nostrand, 1968.
8. Benaron, D. A. and D. K. Stevenson. "Optical time-of-light and absorbance imaging of biological media," *Science*, *259*:1463-1466 (1993).
9. Bigelow, Lt W. S. *Photon Transport from a Point Source in the Atmosphere*. MS thesis, AFIT/GNE/PH/68-3, Air Force Institute of Technology, Wright-Patterson AFB, Ohio, 1968.
10. Boas, D. A. *Diffuse Photon Probes of Structural and Dynamical Properties of Turbid Media: Theory and Biomedical Applications*. PhD dissertation, University of Pennsylvania, Philadelphia PA, 1996.
11. Boas, D. A., et al. "Scattering and wavelength transduction of diffuse photon density waves," *Phys. Rev. E*, *47*:R2999-R3002 (May 1993).
12. Boas, D. A., et al. "Scattering of diffuse photon density waves by spherical inhomogeneities within turbid media: Analytic solution and applications," *Proc. Natl. Acad. Sci. USA*, *91*:4887-4891 (May 1994).
13. Boas, D. A., et al. "Detection and characterization of optical inhomogeneities with diffuse photon density waves: a signal-to-noise analysis," *Appl. Opt.*, *36*:75-92 (January 1997).
14. Brekhovskikh, L. M. *Waves in Layered Media* (Second Edition). New York: Academic Press, 1980.
15. Cartwright, C. H. "Infrared Transmission of the Skin," *Journal of the Optical Society of America*, *30*:81-84 (1930).

16. Case, K. M. and P. F. Zweifel. *Linear Transport Theory*. Massachusetts: Addison-Wesley, 1967.
17. Chance, B., et al. "Highly sensitive object location in tissue models with linear in-phase and anti-phase multi-element optical arrays in one and two dimensions," *Proc. Natl. Acad. Sci. USA*, 90:3423-3427 (April 1993).
18. Cheong, W., et al. "A review of the optical properties of biological tissues," *IEEE J. Quan. Elect.*, 26 (December 1990).
19. Contini, D., et al. "Photon migration through a turbid slab described by a model based on diffusion approximation. I. Theory," *Appl. Opt.*, 36:4587-4599 (July 1997).
20. Cutler, M. "Transillumination as an Aid in the Diagnosis of Breast Lesions," *Surgery, Gynecology, and Obstetrics*, 48:712-729 (1929).
21. Cutler, M. "Transillumination of the Breast," *Ann. Surg.*, 93:223-234 (1931).
22. Davison, B. *Neutron Transport Theory*. London: Oxford, 1958.
23. Devaney, A. J. and E. Wolf. "Multipole expansions and plane wave representations of the electromagnetic field," *J. Math. Phys.*, 15:234-244 (February 1974).
24. Fantini, S., et al. "Frequency-domain optical mammography: edge effect corrections," *Med. Phys.*, 23 (1996).
25. Ferguson, K. *The Fire in the Equations: Science, Religion, and the Search for God*. Michigan: Eerdmans Publishing Co., 1994.
26. Fernandez, J. E. and V. G. Molinari. "Diffusion of polarized photons in the frame of the transport theory," *Nuclear Instruments and Methods in Physics Research*, 73:341-351 (1993).
27. Fishkin, J. B., et al. "Frequency-domain photon migration measurements of normal and malignant tissue optical properties in a human subject," *Appl. Opt.*, 36:10-20 (January 1997).
28. Fishkin, J. B. and E. Gratton. "Propagation of photon density waves in strongly scattering media containing an absorbing semi-infinite plane bounded by a straight edge," *J. Opt. Soc. of Am. A*, 10:127-140 (January 1993).
29. Furutsu, K. and Y. Yamada. "Diffusion approximation for a dissipative random medium and the applications," *Phys. Rev. E*, 50:3634-3640 (November 1994).
30. Gandjbakhche, A. H., et al. "Scaling relationships for theories of anisotropic random walks applied to tissue optics," *Appl. Opt.*, 32:504-516 (February 1993).
31. Glasstone, S. and M. C. Edlund. *The Elements of Nuclear Reactor Theory*. New Jersey: Van Nostrand, 1952.
32. Goodman, J. W. *Introduction to Fourier Optics* (Second Edition). San Francisco: McGraw-Hill, 1996.
33. Haskell, R. C., et al. "Boundary conditions for the diffusion equation in radiative transfer," *J. Opt. Soc. Am. A*, 11:2727-2741 (October 1994).

34. Ishimaru, A. *Wave Propagation and Scattering in Random Media. Vol. 1.* New York: Academic, 1978.
35. Jackson, J. D. *Classical Electrodynamics.* New York: Wiley and Sons Inc., 1975.
36. Lafreniere, R., et al. "Infrared Light Scanning of the Breast," *The American Surgeon*, 52:123-128 (March 1986).
37. Liu, H., et al. "Determination of optical properties and blood oxygenation using continuous NIR light," *Phys. Med. Biol.*, 40:1983 (1995).
38. Liu, H. and K. Lau. "Experimental Validation of Three-Dimensional Reconstruction of Inhomogeneity Images in Turbid Media." Final Report for Summer Faculty Research Program, sponsored by Phillips Laboratory, Kirtland AFB, NM and AFOSR, Bolling AFB, Washington D.C., August 1997.
39. Matson, C. L. "A diffraction tomographic model of the forward problem using diffuse photon density waves," *Optics Express*, 1:6-11 (1997).
40. Matson, C. L., et al. "Three-dimensional tumor localization in thick tissue with the use of diffuse photon-density waves," *Appl. Opt.*, 36:214-220 (January 1997).
41. This code was ported to MATLAB 5.0© from an Image Description Language (IDL) code authored by Dr. Chuck Matson.
42. Morse, P. M. and H. Feshbach. *Methods of Theoretical Physics, I & II.* New York: McGraw-Hill, 1953.
43. Morton, R. and S. S. Miller. "Infrared Transilluminations Using Photography and Television," *Journal of Audiovisual Media in Medicine*, 4:86-90 (1981).
44. O'Leary, M. A., et al. "Refraction of diffuse photon density waves," *Phys. Rev. Lett.*, 69:2658-2661 (November 1992).
45. O'Leary, M. A., et al. "Experimental images of heterogeneous turbid media by frequency-domain diffusing-photon tomography," *Opt. Lett.*, 20:426-428 (March 1995).
46. Ostermeyer, M. R. and S. L. Jacques. "Perturbation theory for diffuse light transport in complex biological tissues," *J. Opt. Soc. Am. A*, 14:255-261 (January 1997).
47. Patterson, M., et al. "Time resolved reflectance and transmittance for the non-invasive measurement of tissue optical properties," *Appl. Opt.*, 28:2331-2336 (June 1988).
48. Peters, V. G., et al. "Optical properties of normal and diseased human breast tissues in the visible and near infrared," *Phys. Med. Biol.*, 35:1317-1334 (1990).
49. See the Photon Migration Imaging (PMI) Code Home Page developed by D. Boas et al.: URL <http://dpdw.eotc.tufts.edu/boas/PMI/pmi.html>.
50. Rebane, A. and J. Feinberg. "Time-resolved holography," *Nature (London)*, 351:378-380 (1991).
51. Schmitt, J. M., et al. "Interference of diffusive light waves," *J. Opt. Soc. Am. A*, 9:1832-1843 (October 1992).

52. Senior, T. B. A. and R. F. Goodrich. "Scattering by a sphere," *Proc. Inst. EE*, 111:907-916 (May 1964).
53. Svaasand, L. O., et al. "Tissue characterization and imaging using photon density waves," *Opt. Eng.*, 32:258-265 (February 1993).
54. Tromberg, B. J., et al. "Properties of photon density waves in multiple-scattering media," *Appl. Opt.*, 32:607-616 (February 1993).
55. Wang, L., et al. "Ballistic 2-D imaging through scattering walls using an ultrafast optical Kerr gate," *Science*, 253:769-771 (1991).
56. Whittaker, E. T. "On the partial differential equations of mathematical physics," *Math. Ann.*, 57:333-355 (1902).
57. Wolf, E. "Three-dimensional structure determination of semi-transparent objects from holographic data," *Opt. Comm.*, 1:153-156 (September/October 1969).
58. Yodh, A. G. and B. Chance. "Spectroscopy and Imaging with Diffusing Light," *Physics Today*, 48:34-40 (March 1995).

## *Vita*

Captain Deborah L. Lasocki was born on 6 October 1969 in Chelsea, Massachusetts. In Fairfax, Virginia, she graduated from Robinson Secondary High School. She attended the University of Notre Dame in South Bend, Indiana from which she received the degree of Bachelor of Science in Electrical Engineering in May, 1991. Upon graduation, Capt Lasocki tendered a regular commission from the Reserve Officer Training Corps and was honored as a distinguished graduate.

After graduation from college, Captain Lasocki was assigned to the National Security Agency at Fort George G. Meade in March 1992. She temporarily served as Executive Assistant to the Staff Judge Advocate before taking over as a Design Engineer in the Research & Engineering Group in July 1992. There, she was responsible for developing analog and digital integrated circuits for DoD combat intelligence systems. She researched, developed, evaluated and acquired integrated circuit computer-aided-design tools and acted as a consultant for those tools and methodologies for National, Air Force, and other service's command, control, communications, and signals intelligence systems. Captain Lasocki assumed the duties as the Program Manager for Advanced Communications Technologies in the Target Access Plans and Programs Element of the Global Signals Technology and Combat Support Group. She was responsible for plans, programs, testing, deployment and budgets for a signals search and collection system. She also led a multi-directorate team in the design, development and deployment of a universal test system to worldwide sights.

While assigned in the Washington D.C. area, she served as a White House Social Aide, headed the 694 IG Mentorship Program for officers, directed the Lieutenants' Professional Development Program, and acted as President of the Company Grade Officers' Council.

In May, 1996, she entered the School of Engineering, Air Force Institute of Technology, as a masters degree candidate. Following graduate school, Captain Lasocki will be heading a branch in the AFMC Space Systems Support Group at Peterson AFB, Colorado.

Permanent address: 6084 Burnside Landing Drive  
Burke, Virginia 22015

**REPORT DOCUMENTATION PAGE**

*Form Approved  
OMB No. 0704-0188*

Public reporting burden for this collection of information is estimated to average 1 hour per response, including the time for reviewing instructions, searching existing data sources, gathering and maintaining the data needed, and completing and reviewing the collection of information. Send comments regarding this burden estimate or any other aspect of this collection of information, including suggestions for reducing this burden, to Washington Headquarters Services, Directorate for Information Operations and Reports, 1215 Jefferson Davis Highway, Suite 1204, Arlington, VA 22202-4302, and to the Office of Management and Budget, Paperwork Reduction Project (0704-0188), Washington, DC 20503.

<b>1. AGENCY USE ONLY (Leave blank)</b>		<b>2. REPORT DATE</b> December 1997	<b>3. REPORT TYPE AND DATES COVERED</b> Master of Science Thesis	
<b>4. TITLE AND SUBTITLE</b> Analytic Transfer Function of the Forward Propagation of Diffuse Photon Density Waves in Turbid Media with an Embedded Spherical Inhomogeneity			<b>5. FUNDING NUMBERS</b>	
<b>6. AUTHOR(S)</b> Deborah L. Lasocki, B.S.E.E., Captain, USAF				
<b>7. PERFORMING ORGANIZATION NAME(S) AND ADDRESS(ES)</b> School of Engineering (AFIT/ENG) Air Force Institute of Technology Wright-Patterson AFB, OH 45433-6583			<b>8. PERFORMING ORGANIZATION REPORT NUMBER</b>  AFIT/GE/ENG/97D-01	
<b>9. SPONSORING/MONITORING AGENCY NAME(S) AND ADDRESS(ES)</b> Phillips Laboratory Advanced Imaging Division 3550 Aberdeen Ave SE Kirtland AFB, NM 87117-5776			<b>10. SPONSORING/MONITORING AGENCY REPORT NUMBER</b>	
<b>11. SUPPLEMENTARY NOTES</b>				
<b>12a. DISTRIBUTION AVAILABILITY STATEMENT</b> Approved for Public Release Distribution Unlimited			<b>12b. DISTRIBUTION CODE</b>	
<b>13. ABSTRACT (Maximum 200 words)</b> <p>Diffusing photons can be used to detect and localize optical inhomogeneities embedded in turbid media such as clouds, fog, paint and human tissue. This thesis shows that a transfer function derived from an analytic solution of the Helmholtz equation can completely characterize in three dimensions the perturbations in the forward propagation phenomena caused by a spherical defect object in a multiple-scattering medium.</p> <p>Two models of the forward propagation behavior of diffuse photon density waves in homogeneous, infinite, turbid media that contains a spherical inhomogeneity are examined. The first model is an exact analytic solution based on a modal expansion in spherical harmonics. The second model uses Fourier optics theory for wave propagation in a plane through homogeneous turbid media containing a spherical lens. The Fourier optics model is found to be a good approximation to the exact analytic solution when the optical absorptive contrast of the inhomogeneity and the surrounding media is weakly perturbative, and the detector is not near the inhomogeneity.</p> <p>Using linear system theory, a transfer function from the analytic model is derived. This function improves the Fourier optics model by replacing the spherical lens approximation with an exact representation of the system perturbation behavior. The transfer function is shown through simulation to completely characterize the sensitivity of the system to detect and localize in three dimensions inhomogeneities of varying optical contrast with the surrounding media.</p>				
<b>14. SUBJECT TERMS</b> diffuse photon density waves, transfer function, three dimensional localization, wave propagation, turbid media, breast tumor detection			<b>15. NUMBER OF PAGES</b> 125	
			<b>16. PRICE CODE</b>	
<b>17. SECURITY CLASSIFICATION OF REPORT</b> UNCLASSIFIED	<b>18. SECURITY CLASSIFICATION OF THIS PAGE</b> UNCLASSIFIED	<b>19. SECURITY CLASSIFICATION OF ABSTRACT</b> UNCLASSIFIED	<b>20. LIMITATION OF ABSTRACT</b> UL	